

DISSERTATION

Advanced Monte Carlo Simulation for Semiconductor Devices

ausgeführt zum Zwecke der Erlangung des akademischen
Grades
eines Doktors der technischen Wissenschaften

eingereicht an der Technischen Universität Wien
Fakultät für Elektrotechnik und Informationstechnik
von

GERHARD KARLOWATZ



Wien, im April 2009

Kurzfassung

In Standardsimulatoren für Halbleiterbauelemente werden die elektrischen Eigenschaften der Bauelemente durch Anwendung des Drift-Diffusionsmodells berechnet. Die Entwicklung immer komplexerer und kleinerer Bauelemente verlangt jedoch zunehmend nach physikalisch exakteren Simulationsmethoden, so wie die in dieser Arbeit behandelte Monte Carlo Methode. Ein besonders relevantes Einsatzgebiet dieser Methode ist die Erforschung der elektrischen Eigenschaften von verspanntem Silizium und Germanium. Mechanische Verspannung erhöht signifikant die Ladungsträgerbeweglichkeit, ein Effekt der seit einigen Jahren wesentlich zur Leistungssteigerung in der CMOS Technologie eingesetzt wird.

In dieser Arbeit werden zuerst der Spannungs- und der Verzerrungstensor eingeführt und anschließend die Symmetrieeigenschaften der Bandstruktur des kubisch flächenzentrierten Kristalls im unverspannten sowie im verspannten Zustand dargestellt. Aus den Symmetrieeigenschaften wird für mehrere Verspannungszustände der irreduzible Bereich der Brillouin Zone hergeleitet, für den die Berechnung der Bandstruktur zu erfolgen hat. Die Bandstruktur wird mit der Pseudopotentialmethode berechnet und auf einem Gitter diskretisiert.

Der Hauptteil dieser Arbeit beschäftigt sich mit der Simulation des Ladungsträgertransports mit Hilfe der sogenannten Full Band Monte Carlo Methode. Die wesentlichen verwendeten Algorithmen und Streumodelle werden dargestellt. Der Schwerpunkt liegt hierbei auf neuen Methoden zur Verkürzung der Simulationszeiten. In diesem Zusammenhang werden die Implementierung lokal verfeinerter Tetraedergitter für die Diskretisierung der Brillouinzone und der effiziente Einsatz von Verwerfungsmethoden bei der Monte Carlo Methode untersucht.

Die Ergebnisse der Bandstruktur- und der Transportberechnungen werden im Kontext neuer theoretischer Beschreibungen diskutiert. Im verspannten Silizium kommt es zu einer Aufhebung der Entartung der X-Täler und in Folge zu einer bevorzugten Besetzung der energetisch niedrigeren Täler. Zusätzlich zur Verschiebung der Leitungsbandtöler relativ zueinander kann auch eine Änderung der effektiven Elektro-

nenmassen auftreten. Dieser Effekt beruht auf der Wirkung von Scherspannung, die eine Deformation der Leitungsbandminima verursacht. Eine Analyse der Valenzbänder im verspannten Kristall zeigt eine Aufhebung der Entartung des schweren und leichten Löcherbandes im Γ -Punkt. Scherspannung erhöht die Löcherbeweglichkeit in bestimmte Vorzugsrichtungen aufgrund einer Deformierung der Valenzbänder.

Bei industriell gefertigten CMOS Transistoren wird der Kanal mit uniaxialer Zugverspannung in [110] Richtung belegt. Für diesen Verspannungszustand ergibt sich bei 1.5 GPa in der Simulation im Bulkkrystall für Silizium eine Beweglichkeitssteigerung der Elektronen um den Faktor 1.68. Die Löcherbeweglichkeit in Germanium kann mit kompressiver Verspannung von 1.5 GPa in [110] Richtung um den Faktor 2.55 auf 4790 cm/Vs gesteigert werden.

Ein weiter Teil der Arbeit behandelt die Simulation von Blocked Impurity Band Fotodetektoren. Diese Bauelemente werden im langwelligen Infrarotbereich eingesetzt und arbeiten bei niedrigen Temperaturen unter 10 K. Die Detektion eines Photons erfolgt dabei durch die Anhebung eines Ladungsträgers aus einem hoch dotierten Störstellenband in ein höhergelegenes Leitungsband aufgrund einer optischen Anregung. Es werden die Erweiterungen des Monte Carlo Simulators um ein für tiefe Simulationstemperaturen geeignetes inelastisches Streumodell für akustische Phononen beschrieben, sowie ein Modell zur individuellen Simulation aller Ladungsträger einer durch Stoßionisation entstehenden Ladungsträgerlawine. Es werden die energetischen und zeitlichen Verteilungen der Ladungsträgerlawine berechnet.

Abstract

In standard simulators for semiconductor devices the electrical behavior of the devices is calculated using the drift-diffusion model. The development of more complex and smaller devices demands for more exact simulation methods, such as the Monte Carlo method examined within this work. An important application of the Monte Carlo method is the study of the electrical behavior of Silicon and Germanium. Mechanical strain can raise significantly the carrier mobility in a semiconductor. This effect has been utilized over the last few years to enhance performance of CMOS technology.

This work starts with an introduction of the stress- and strain tensors. Then the symmetry properties of the band structure of the relaxed and the strained diamond lattice are presented. The irreducible domains of the Brillouin zone for band structure calculation are derived for important strain configurations. The band structure is calculated using the pseudo potential method and discretized on a mesh.

The main part of this work is about the simulation of carrier transport using the full-band Monte Carlo method. Important numerical algorithms and scattering models are presented. The scope is on new algorithms, which reduce simulation times. In this regard the generation of locally refined meshes for the Brillouin zone and the efficient implementation of rejection algorithms are explored.

Results from band structure and carrier transport calculations are discussed in the context of recent theoretical findings. In strained Silicon the degeneration of the X-valleys is lifted. As a consequence the valleys lower in energy are higher populated. Band structure calculations show, that in addition to the shift of the conduction band valleys relative to each other, the effective electron masses can be changed. This is caused by shear strain, which leads to an deformation of the valley minima. An analysis of the valence bands of a strained crystal shows that the degeneration of the heavy hole and light hole bands at the Γ -point is lifted. Shear strain increases the hole mobility along certain directions, an effect caused by a deformation of the valence bands.

Mass manufactured CMOS transistors feature a uniaxially tensile strained channel in [110] direction. Simulations at 1.5 GPa for this strain configuration show a mobility gain by a factor of 1.68 to 2410 cm/Vs for electrons in bulk Silicon. For compressively strained Germanium hole mobility is raised by a factor of 2.55 up to 4790 cm/Vs at 1.5GPa stress in [110] direction.

The final part of this work deals with the simulation of blocked impurity band photo detectors. These devices operate in the long wave length infrared range at temperatures below 10 K. A photon is detected by lifting a carrier from a heavy doped impurity band by optical excitation to the conduction band. The simulator is extended by an inelastic scattering model for acoustic phonons, which is appropriate for simulations at low device temperature. A model for individual simulation of every carrier from an avalanche caused by impact ionization is also implemented. The distribution in energy and arrival time of the carrier avalanche is calculated.

Danksagung

Diese Arbeit wäre ohne die Unterstützung vieler Leute, denen ich hier meinen Dank aussprechen will, nicht möglich gewesen.

Zunächst möchte ich meinen Dank Prof. Dr. Siegfried Selberherr und Prof. Dr. Erasmus Langer ausdrücken, durch deren Bemühen ihr Institut stets ein optimales Umfeld für das Gelingen meiner Arbeit geboten hat. Mein besonderer Dank gilt meinem Betreuer Prof. Dr. Hans Kosina. Sein enormes Fachwissen in Verbindung mit seiner geduldigen Haltung bei der Vermittlung desselben haben zum Erfolg dieser Arbeit wesentlich beigetragen.

Meine Zimmerkollegen waren ebenfalls am Gelingen dieser Arbeit wesentlich beteiligt. Stets hilfreich in Fragen zur theoretischen Physik war mein Zimmerkollege Viktor Sverdlov, mit Wilfried Wessner hat sich eine fruchtbare Zusammenarbeit im Bereich der Gittergenerierung ergeben, mit der Unterstützung von Sephan Wagner konnte ich meine Programmierkenntnisse in kürzester Zeit auf das erforderliche Niveau heben und Oliver Triebel hatte auf Fragen im Bereich der IT-Infrastruktur immer die richtigen Antworten parat.

Gerne habe ich zusammen mit meinem Kollegen Enzo Ungersböck unsere Simulationssoftware weiterentwickelt, aber auch meine Kollegen Oskar Baumgartner, Johann Cervenka, Siddhartha Dhar, Robert Entner, Philipp Hehenberger, Stefan Holzer, Markus Karner, Gregor Meller, Vassil Palankovski, Alireza Sheikholeslami, Mahdi Pourfath, Philipp Schwaha, Martin Vasicek, Martin Wagner, Paul Wagner und Robert Wittmann sorgten für ein angenehmes und kreatives Arbeitsumfeld. Ich hoffe, dass mich mit möglichst vielen meiner Kollegen eine langjährige Freundschaft verbinden wird.

Zuletzt möchte ich mich bei meiner Familie und meiner Freundin Martina bedanken. Ihre Liebe hat mich während meiner Arbeit stets begleitet.

Contents

List of Abbreviations and Acronyms	ix
List of Symbols	x
Notation	x
Physical Quantities	xi
Constants	xii
1 Introduction	1
2 Strained Band Structure	3
2.1 Definition of Stress	3
2.2 Definition of Strain	4
2.3 Stress-Strain Relations	5
2.3.1 Notation of Planes and Directions in a Crystal	7
2.3.2 Stress Applied Along Symmetry Directions	8
2.4 Configuration of the Diamond Structure	10
2.5 Effect of Strain on Symmetry	12
2.5.1 The Point Group Symmetry Operations	13
2.6 The Reciprocal Lattice	14
2.6.1 The Relaxed Diamond Structure: O_h Symmetry	16

CONTENTS

2.6.2	The Biaxially Strained Diamond Structure: D_{4h} Symmetry . . .	17
2.6.3	D_{2h} Symmetry	18
2.6.4	S_2 Symmetry	18
2.6.5	Utilizing Symmetry Properties in Monte Carlo Simulation . . .	19
3	The Semiclassical Transport Model	21
3.1	The Equations of Motion	21
3.2	Boltzmann Transp. Equation	22
3.3	Scattering Mechanisms	24
3.3.1	Phonon Scattering	26
3.3.2	Ionized Impurity Scattering	34
3.3.3	Impact Ionization	38
4	Monte Carlo Technique	40
4.1	Random Numbers: Direct and Indirect Method	40
4.2	Piecewise Constant Gamma Scheme	41
4.3	Self-Scattering Scheme	44
4.4	Selecting a k-vector after Scattering	45
4.5	Meshing of the Brillouin Zone	48
4.6	Calculating the DOS	55
4.7	Precalculated Values related to the Mesh	60
4.8	Selfconsistent Monte Carlo Scheme	60
5	Results	63
5.1	The Conduction Band Structure of Strained Si	63
5.1.1	Valley splitting	63
5.1.2	Effective mass change	64
5.2	Low Field Electron Mobility of Strained Si	65
5.3	High Field Electron Mobility of Strained Si	68
5.4	The Valence Band Structure of Strained Ge	70

CONTENTS

5.4.1	Band splitting	70
5.4.2	Effective mass change	71
5.5	Low Field Mobility of Holes in Strained Ge	72
5.6	High Field Mobility of Holes in Strained Ge	74
6	BIB Devices	77
6.1	Introduction	77
6.2	Operation of BIB Detectors	78
6.3	Hopping Conduction	82
6.4	Monte Carlo Simulation of BIB Detectors	84
6.4.1	Neutral Impurity Scattering	84
6.4.2	Non-Markovian Impact Ionization Model	85
6.5	Results	86
6.5.1	Electrostatic Field	86
6.5.2	BIB Device as a Single Photon Counter	88
7	Summary and Conclusions	92
	Curriculum Vitae	106

List of Abbreviations and Acronyms

BIB	...	Blocked impurity band
BTE	...	Boltzmann transport equation
BZ	...	Brillouin zone
CMOS	...	Complementary MOS
EPM	...	Empirical pseudopotential method
FBMC	...	Monte Carlo simulation based on full-band structure
FET	...	Field-effect transistor
HH	...	heavy hole
ITRS	...	International Technology Roadmap for Semiconductors
IR	...	Infrared
LH	...	light hole
MC	...	Monte Carlo
MOS	...	Metal-oxide-semiconductor
MOSFET	...	Metal-oxide-semiconductor field-effect transistor
SO	...	split-off band
TCAD	...	Technology Computer Aided Design
UTB	...	Ultra-thin-body
VMC	...	Vienna Monte Carlo simulator

List of Symbols

Notation

k	...	Constant
x	...	Scalar
\mathbf{x}	...	Vector
\underline{T}	...	Tensor
\mathcal{X}	...	Operator
T_{ij}	...	Elements of the matrix \underline{T}
$[hkl]$...	Miller indices to specify a crystal direction
$\langle hkl \rangle$...	Miller indices to specify equivalent crystal directions
(hkl)	...	Miller indices to specify a crystal plane
$\{hkl\}$...	Miller indices to specify equivalent crystal planes

Physical Quantities

Symbol	Unit	Description
ε	eV	Energy
ε_f	eV	Fermi energy
ε_g	eV	Band gap energy
\mathbf{E}	Vm^{-1}	Electric field
\mathbf{F}	N	Force
$f(\mathbf{r}, \mathbf{k}, t)$	1	Distribution function
ϕ	V	Electrostatic potential
g	$\text{m}^{-3}\text{eV}^{-1}$	Density of states
$\hbar\omega$	eV	Phonon energy
k	m^{-1}	Wave number
\mathbf{k}	m^{-1}	Wave number vector
k_f	m^{-1}	Radius of Fermi sphere
ϵ_s	$\text{AsV}^{-1}\text{m}^{-1}$	static dielectric coefficient
μ_n	$\text{m}^2\text{V}^{-1}\text{s}^{-1}$	Electron mobility
μ_p	$\text{m}^2\text{V}^{-1}\text{s}^{-1}$	Hole mobility
m	kg	Mass
m_{dos}	kg	Density of states mass
n	m^{-3}	Electron concentration
ψ	$\text{m}^{-3/2}$	Wave function
\mathbf{r}	m	Position vector
γ_{ij}	1	Engineering strain component (i, j)
ε_{ij}	1	Component (ij) of the strain tensor
T_{ij}	GPa	Component (ij) of the stress tensor
C_{ijkl}	GPa	Component ($ijkl$) of the elastic stiffness tensor
c_{ij}	GPa	Component (ij) of the contracted stiffness tensor
S_{ijkl}	GPa^{-1}	Component ($ijkl$) of the elastic compliance tensor
s_{ij}	GPa^{-1}	Component (ij) of the contracted compliance tensor
t	s	Time
T	K	Temperature
\mathbf{v}	ms^{-1}	Velocity vector

Constants

h	...	Planck's constant	$6.6260755 \times 10^{-34} \text{ Js}$
\hbar	...	Reduced Planck's constant	$h/(2\pi)$
k_B	...	Boltzmann's constant	$1.380662 \times 10^{-23} \text{ JK}^{-1}$
e	...	Elementary charge	$1.6021892 \times 10^{-19} \text{ C}$
m_0	...	Electron rest mass	$9.1093897 \times 10^{-31} \text{ kg}$
ϵ_0	...	Permittivity constant of vacuum	$8.8541878 \times 10^{-12} \text{ AsV}^{-1}\text{m}^{-1}$

Chapter 1

Introduction

Over the last three decades our way of life was dramatically changed by the spread of new electronic appliances. Important achievements like personal computers, mobile phones, or the world wide web form a new digital world, a world driven by the progress in semiconductor device and process research and development.

By far the most widely used semiconductor device for logic integrated circuits is the metal-oxide-semiconductor field-effect transistor (MOSFET). It is implemented exclusively on Si substrates. The main reason for the impressive performance improvements over the last decades results from the down scaling of this device. Scaling does not just allow to integrate more transistors within one circuit. When making the devices smaller they also exhibit reduced switching times and reduced power consumption. As predicted by the International Technology Road-map for Semiconductors [SIA06] this trend is expected to continue in the coming decade and then coming to an end because of rising costs when scaling is pushed close to principal physical limits [Haensch06].

These limits are, on the one hand, related to the fabrication process itself. It gets more and more challenging to achieve the needed resolution in lithography for the next technology node. On the other hand, important device properties do not benefit from scaling any more, or even get worse. A major problem in this respect is the gate leakage current, which raises exponentially for smaller gate oxide thickness. For the upcoming 45 nm technology node this problem is solved by the introduction of metal gates and hafnium-based high- κ dielectrics [Intel07]. With further downscaling also variability in the delay and power consumption is becoming an urgent problem for designers [Bernstein06]. Another problem is the increase of the source-drain series resistance caused by the need for ultra-shallow p-n junctions in the source-drain regions [Skotnicki05].

These problems slow down the scaling process significantly and already brought

alternative approaches to improve device performance into focus. These approaches include new device designs like multi-gate MOSFETs or ultra thin body (UTB) MOSFETs as well as the introduction of strain engineering.

In this work the use of strained Si to improve the carrier mobility is explored with technical computer aided design (TCAD) methods. Whereas conventional TCAD simulators are based on drift-diffusion models, here, a full-band Monte Carlo (FBMC) simulator is developed which delivers more accurate and refined electrical transport properties of strained Si, Ge, and SiGe alloys. In the past the use of full-band Monte Carlo methods was limited by their high demand for computation time, so that their main purpose in TCAD was to deliver accurate data for calibration of less fundamental methods such as drift-diffusion. However, it is shown, that due to the ever increasing availability of computational power and with the implementation of CPU-time efficient algorithms, FBMC can be used for simulation of MOSFET devices [Jungemann03]. In this work FBMC is applied to explore blocked impurity band (BIB) devices [Petroff86]. These devices are photo detectors for the far infrared band which operate at very low temperatures.

In **Chapter 2** a short introduction to the theory of stress and strain in elastic bodies is given. Next the conduction band structure of Si as well as the valence band structure of Ge is analyzed in detail. The band structure data are obtained with the empirical pseudopotential method (EPM). To improve the performance of EPM calculations and of FBMC simulations it is important to take advantage of the symmetry properties of the Brillouin zone. Therefore, the symmetry properties under several strain conditions are investigated in detail.

In **Chapter 3** an introduction to the semi-classical Monte Carlo method is given, with emphasis on the algorithms and models actually implemented in the full-band simulator. This also includes a description of the methods used for meshing the Brillouin zone, which have a critical impact on the simulator performance and accuracy.

The Monte Carlo simulator is adopted to explore BIB devices in **Chapter 4**. These photo detectors for the far infrared range are mainly used in space based observation facilities. BIB detectors deliver high quantum efficiency in a volume much smaller than in conventional photoconductors because of their much higher primary doping. The primary dopants form an impurity band, in which significant hopping conduction occurs. To block dark current introduced by hopping carriers the device features an undoped region, referred as the blocking layer. Some of the standard scattering models for Monte Carlo have to be extended to deliver valid results for temperatures below 10 K. Also an approach for a non-Markovian impact ionization model is presented. At the end of that chapter simulation results for a BIB device operating as a photon counter are presented.

Chapter 2

Strain Related Effects on the Band Structure

In this chapter a short introduction to the theory of stress and strain in elastic bodies is given. To improve the performance of FBMC simulations it is important to take advantage of the symmetry properties of the band structure. Therefore, the symmetry properties of the reciprocal diamond lattice are investigated in detail for several strain conditions.

2.1 Definition of Stress

To keep a body in static equilibrium the sum of all forces acting on it must be zero. If a small cubicle volume as depicted in Figure 2.1 of the body is considered, forces $\Delta \mathbf{F}_i$ act on the surfaces ΔA_i . The index i indicates one of the surface planes. The stress vector \mathbf{T}_i is then defined as the limit [Bir74]

$$\mathbf{T}_i = \lim_{\Delta A_i \rightarrow 0} \frac{\Delta \mathbf{F}_i}{\Delta A_i} = \frac{d\mathbf{F}_i}{dA_i}. \quad (2.1)$$

As depicted in Figure 2.1, each of the three stress vectors can be decomposed into two components within the plane, the so called shear stress components, and one normal component. The total number of six shear stress components and three normal stress components can be lumped together into the stress tensor \underline{T}

$$\underline{T} = \begin{pmatrix} T_{xx} & T_{xy} & T_{xz} \\ T_{xy} & T_{yy} & T_{yz} \\ T_{xz} & T_{yz} & T_{zz} \end{pmatrix}. \quad (2.2)$$

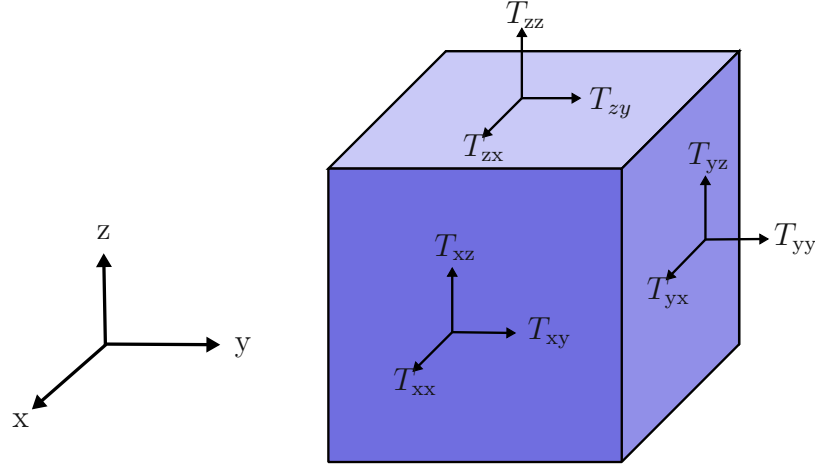


Figure 2.1: Stress components acting on an infinitesimal cube.

To fulfill the condition of static equilibrium, the shear stress components across a diagonal are identical,

$$T_{xy} = T_{yx} , \quad T_{yz} = T_{zy} , \quad T_{zx} = T_{xz} , \quad (2.3)$$

which leads to six independent components in the stress tensor.

2.2 Definition of Strain

Stress forces within a body cause an elastic deformation which is called strain. Two points at locations \mathbf{x} and $\mathbf{x} + d\mathbf{x}$ within a relaxed body move under deformation caused by stress to the locations $\mathbf{x} + \mathbf{u}(\mathbf{x})$ and $\mathbf{x} + d\mathbf{x} + \mathbf{u}(\mathbf{x} + d\mathbf{x})$. The absolute squared distance between the deformed points can then be obtained as [Bir74]

$$\sum_i (dx_i + u_i(\mathbf{x} + d\mathbf{x}) - u_i(\mathbf{x}))^2 = \sum_i \left(dx_i + \sum_j \frac{\partial u_i}{\partial x_j} dx_j \right)^2 . \quad (2.4)$$

Since $d\mathbf{x}$ is considered to be a small displacement, a Taylor expansion around \mathbf{x} can be performed, which gives for the the absolute squared distance

$$\sum_i \left(dx_i + \sum_j \frac{\partial u_i}{\partial x_j} dx_j \right)^2 = \sum_i dx_i^2 + 2 \sum_{i,j} dx_i \frac{\partial u_i}{\partial x_j} dx_j + \sum_{i,j,k} \frac{\partial u_i}{\partial x_j} dx_j \frac{\partial u_i}{\partial x_k} dx_k . \quad (2.5)$$

Since the first term in (2.5) is the squared distance between the points in the relaxed system the change in the squared distance caused by strain becomes

$$\begin{aligned}
 D(d\mathbf{x}) &= \sum_{i,j} dx_i \left(\frac{\partial u_i}{\partial x_j} + \frac{\partial u_j}{\partial x_i} \right) dx_j + \sum_{i,j,k} \frac{\partial u_k}{\partial x_i} \frac{\partial u_k}{\partial x_j} dx_i dx_j \\
 &= \sum_{i,j} dx_i \left[\left(\frac{\partial u_i}{\partial x_j} + \frac{\partial u_j}{\partial x_i} \right) + \sum_k \frac{\partial u_k}{\partial x_i} \frac{\partial u_k}{\partial x_j} \right] dx_j \\
 &= 2 \sum_{i,j} dx_i \varepsilon_{ij} dx_j .
 \end{aligned} \tag{2.6}$$

Here, ε_{ij} are the components of the strain tensor which are defined as

$$\varepsilon_{ij} = \frac{1}{2} \left[\frac{\partial u_i}{\partial x_j} + \frac{\partial u_j}{\partial x_i} + \sum_k \frac{\partial u_k}{\partial x_i} \frac{\partial u_k}{\partial x_j} \right]. \tag{2.7}$$

If the strain is small enough such that $\frac{\partial u_k}{\partial x_i} \ll 1$ holds, the second order term in (2.7) can be neglected. This simplifies the resulting tensor components to

$$\varepsilon_{ij} = \frac{1}{2} \left[\frac{\partial u_i}{\partial x_j} + \frac{\partial u_j}{\partial x_i} \right]. \tag{2.8}$$

The strain tensor is therefore symmetric

$$\underline{\varepsilon} = \begin{pmatrix} \varepsilon_{xx} & \varepsilon_{xy} & \varepsilon_{xz} \\ \varepsilon_{yx} & \varepsilon_{yy} & \varepsilon_{yz} \\ \varepsilon_{xz} & \varepsilon_{yz} & \varepsilon_{zz} \end{pmatrix}. \tag{2.9}$$

In literature sometimes the so called engineering shear strain definition is used. The engineering shear strain γ_{ij} for $i \neq j$ is given by the relation

$$\gamma_{ij} = \varepsilon_{ij} + \varepsilon_{ji} = 2\varepsilon_{ij}. \tag{2.10}$$

2.3 Stress-Strain Relations

By observation of the behavior of spring systems, Robert Hooke [Hooke78] first identified a mathematical relation between stress and strain. Hooke's Law denotes

$$F = k x. \tag{2.11}$$

	Si	Ge	Units
c_{11}	166.0	126.0	GPa
c_{12}	64.0	44.0	GPa
c_{44}	79.6	67.7	GPa

Table 2.1: Elastic stiffness constants of Si and Ge [Levinshtein99].

Here, k is the material-dependent spring constant, F is the applied force, and x is the resulting deformation of the spring. Later Cauchy generalized Hooke's law for application to three dimensional elastic bodies

$$T_{ij} = C_{ijkl} \varepsilon_{kl} , \quad (2.12)$$

where C_{ijkl} is the elastic stiffness tensor of order four. The tensor contains 81 components. Since there are only six independent components in the stress and strain tensors they can be written in a contracted notation as six component vectors. In this formulation the elastic stiffness tensor simplifies to a 6x6 matrix.

The number of independent components in the elastic stiffness tensor is further reduced by symmetry properties of the considered crystal [Kittel96]. For cubic semiconductors such as Si, Ge or GaAs, the elastic stiffness tensor contains only three independent components, c_{11} , c_{12} , and c_{44} , which lead to a stress-strain relation of the form

$$\begin{pmatrix} T_{xx} \\ T_{yy} \\ T_{zz} \\ T_{yz} \\ T_{xz} \\ T_{xy} \end{pmatrix} = \begin{pmatrix} c_{11} & c_{12} & c_{12} & 0 & 0 & 0 \\ c_{12} & c_{11} & c_{12} & 0 & 0 & 0 \\ c_{12} & c_{12} & c_{11} & 0 & 0 & 0 \\ 0 & 0 & 0 & c_{44} & 0 & 0 \\ 0 & 0 & 0 & 0 & c_{44} & 0 \\ 0 & 0 & 0 & 0 & 0 & c_{44} \end{pmatrix} \cdot \begin{pmatrix} \varepsilon_{xx} \\ \varepsilon_{yy} \\ \varepsilon_{zz} \\ 2\varepsilon_{yz} \\ 2\varepsilon_{xz} \\ 2\varepsilon_{xy} \end{pmatrix} . \quad (2.13)$$

The factor 2 in the notation of the off-diagonal elements of the strain tensor stems from the fact, that in literature the values of the elastic stiffness constants are usually given for the engineering strain notation. The values for the elastic stiffness constants of Si and Ge are given in Table 2.1.

In the case that the stresses are known, the values for the strains have to be determined by inversion of (2.12). With the introduction of the elastic compliance tensor S_{ijkl} , the inverted equation reads

$$\varepsilon_{ij} = S_{ijkl} T_{kl} , \quad (2.14)$$

or in matrix form for the specific symmetry properties of the diamond lattice

$$\begin{pmatrix} \varepsilon_{xx} \\ \varepsilon_{yy} \\ \varepsilon_{zz} \\ 2\varepsilon_{yz} \\ 2\varepsilon_{xz} \\ 2\varepsilon_{xy} \end{pmatrix} = \begin{pmatrix} s_{11} & s_{12} & s_{12} & 0 & 0 & 0 \\ s_{12} & s_{11} & s_{12} & 0 & 0 & 0 \\ s_{12} & s_{12} & s_{11} & 0 & 0 & 0 \\ 0 & 0 & 0 & s_{44} & 0 & 0 \\ 0 & 0 & 0 & 0 & s_{44} & 0 \\ 0 & 0 & 0 & 0 & 0 & s_{44} \end{pmatrix} \cdot \begin{pmatrix} T_{xx} \\ T_{yy} \\ T_{zz} \\ T_{yz} \\ T_{xz} \\ T_{xy} \end{pmatrix}. \quad (2.15)$$

The elastic compliance constants s_{ij} are related to the elastic stiffness constants c_{ij} by

$$s_{11} = \frac{c_{11} + c_{12}}{c_{11}^2 + c_{11}c_{12} - 2c_{12}^2}, \quad (2.16)$$

$$s_{12} = \frac{-c_{12}}{c_{11}^2 + c_{11}c_{12} - 2c_{12}^2}, \quad (2.17)$$

$$s_{44} = \frac{1}{c_{44}}. \quad (2.18)$$

It should be noted that in literature the stiffness constants are consistently represented by the symbol c_{ij} , while s_{ij} is used for the compliance constants.

2.3.1 Notation of Planes and Directions in a Crystal

To specify directions and planes in a crystal the Miller index notation is commonly used [Ashcroft76, Kittel96]. The Miller indices of a plane are defined in the following way: In a first step three lattice vectors, which form the axis of the crystallographic coordinate system have to be found. In cubic crystal systems, the lattice vectors are chosen along the edges of the crystallographic unit cell. Second the points where a crystal plane intercepts the axes are derived and their coordinates are transformed into fractional coordinates by dividing by the respective cell dimension. In a last step the Miller indices are obtained as the reciprocals of the fractional coordinates. For a cubic crystal they are given as a triplet of integer values (hkl) . A Miller index 0 indicates a plane parallel to the respective axis. Negative indices are defined by a bar written over the number. To denote all planes equivalent by symmetry, the notation $\{hkl\}$ is used.

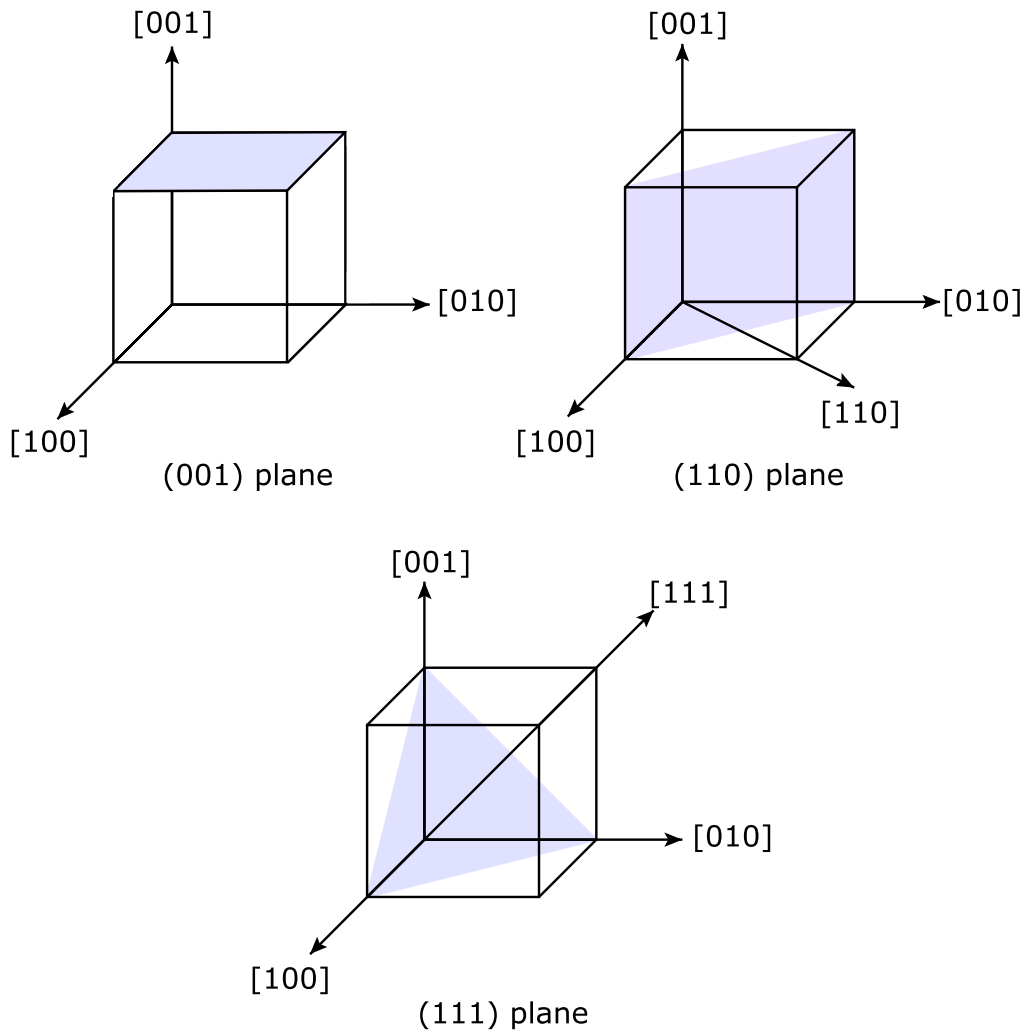


Figure 2.2: Three planes in the cubic system along with their Miller indices.

It is also common to indicate directions in the basis of the lattice vectors by Miller indices with square brackets like in $[hkl]$. The notation $\langle hkl \rangle$ is used to indicate all directions that are equivalent to $[hkl]$ by crystal symmetry.

Figure 2.2 depicts the Miller notation for several planes in the cubic system. The Miller indices of a plane coincide with those of the direction perpendicular to the plane.

2.3.2 Stress Applied Along Symmetry Directions

Uniaxial stress applied along symmetry directions of the cubical crystal is of technological importance since it is preferably used in actual devices. The stress and strain

tensors in the principal coordinate system of the crystal are given in the following for uniaxial stress of magnitude S applied along $[100]$, $[110]$, $[111]$ and $[120]$ directions, respectively. Here, the strain tensors are calculated by inserting the corresponding stress tensors in (2.15).

$$\begin{aligned}
\mathbb{T}_{[100]} &= S \begin{pmatrix} 1 & 0 & 0 \\ 0 & 0 & 0 \\ 0 & 0 & 0 \end{pmatrix}, & \underline{\varepsilon}_{[100]} &= S \begin{pmatrix} s_{11} & 0 & 0 \\ 0 & s_{12} & 0 \\ 0 & 0 & s_{12} \end{pmatrix} \\
\mathbb{T}_{[110]} &= \frac{S}{2} \begin{pmatrix} 1 & 1 & 0 \\ 1 & 1 & 0 \\ 0 & 0 & 0 \end{pmatrix}, & \underline{\varepsilon}_{[110]} &= \frac{S}{2} \begin{pmatrix} s_{11} + s_{12} & s_{44}/2 & 0 \\ s_{44}/2 & s_{11} + s_{12} & 0 \\ 0 & 0 & s_{12} \end{pmatrix} \\
\mathbb{T}_{[111]} &= \frac{S}{3} \begin{pmatrix} 1 & 1 & 1 \\ 1 & 1 & 1 \\ 1 & 1 & 1 \end{pmatrix}, & \underline{\varepsilon}_{[111]} &= \frac{S}{3} \begin{pmatrix} s_{11} + 2s_{12} & s_{44}/2 & s_{44}/2 \\ s_{44}/2 & s_{11} + 2s_{12} & s_{44}/2 \\ s_{44}/2 & s_{44}/2 & s_{11} + 2s_{12} \end{pmatrix} \\
\mathbb{T}_{[120]} &= \frac{S}{5} \begin{pmatrix} 1 & 2 & 0 \\ 2 & 4 & 0 \\ 0 & 0 & 0 \end{pmatrix}, & \underline{\varepsilon}_{[120]} &= \frac{S}{5} \begin{pmatrix} s_{11} + 4s_{12} & s_{44} & 0 \\ s_{44} & s_{12} + 4s_{11} & 0 \\ 0 & 0 & 5s_{12} \end{pmatrix} \quad (2.19)
\end{aligned}$$

Biaxial strain can be introduced in Si by epitaxially growing a Si layer on an SiGe substrate, which features a different lattice constant. The Si layer adjusts to the lattice constant of the SiGe substrate and becomes globally biaxially strained. If the interface is a (001)-plane the strain tensor reads [Hinckley90]

$$\underline{\varepsilon}_{(001)} = \varepsilon_{\parallel} \begin{pmatrix} 1 & 0 & 0 \\ 0 & 1 & 0 \\ 0 & 0 & -\frac{2c_{12}}{c_{11}} \end{pmatrix}, \quad (2.20)$$

where ε_{\parallel} is the strain in the interface plane, related to the lattice mismatch via

$$\varepsilon_{\parallel} = \frac{a_l - a_0}{a_0}. \quad (2.21)$$

Here $a_0 = 5.431 \text{ \AA}$ denotes the lattice constant of relaxed Si and a_l that of the substrate layer. Note that biaxial strain in the (001)-plane leads to the same form of the strain tensor as uniaxial stress in $[001]$ -direction.

2.4 Configuration of the Diamond Structure

A Bravais lattice is an infinite set of points generated by discrete translation operations. Each lattice point is made up by one or more atoms which are called the basis. In the most simple case the basis consists of one atom. It can be derived by point group theory that there exist 14 different Bravais lattices which are divided into seven crystal systems [Bir74]. The lattices within one system share the same point group symmetry operations. Figure 2.3 shows this classification with the properties of each system regarding angles and lengths of their elementary cells.

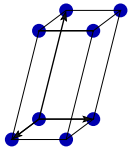
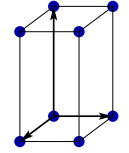
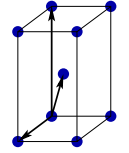
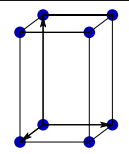
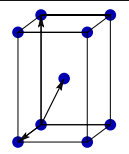
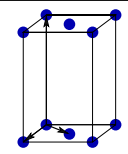
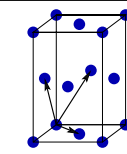
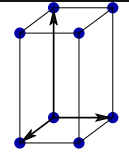
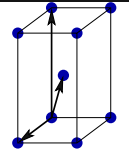
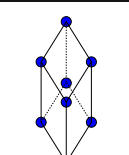
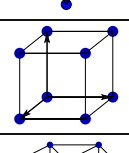
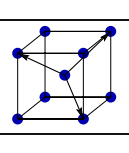
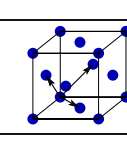
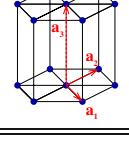
Bravais lattice	Parameters	Simple (P)	Volume centered (I)	Base centered (C)	Face centered (F)
Triclinic	$a_1 \neq a_2 \neq a_3$ $\alpha_{12} \neq \alpha_{23} \neq \alpha_{31}$				
Monoclinic	$a_1 \neq a_2 \neq a_3$ $\alpha_{23} = \alpha_{31} = 90^\circ$ $\alpha_{12} \neq 90^\circ$				
Orthorhombic	$a_1 \neq a_2 \neq a_3$ $\alpha_{12} = \alpha_{23} = \alpha_{31} = 90^\circ$				
Tetragonal	$a_1 = a_2 \neq a_3$ $\alpha_{12} = \alpha_{23} = \alpha_{31} = 90^\circ$				
Trigonal	$a_1 = a_2 = a_3$ $\alpha_{12} = \alpha_{23} = \alpha_{31} < 120^\circ$				
Cubic	$a_1 = a_2 = a_3$ $\alpha_{12} = \alpha_{23} = \alpha_{31} = 90^\circ$				
Hexagonal	$a_1 = a_2 \neq a_3$ $\alpha_{12} = 120^\circ$ $\alpha_{23} = \alpha_{31} = 90^\circ$				

Figure 2.3: Bravais lattices in three dimensions [Anghel03]

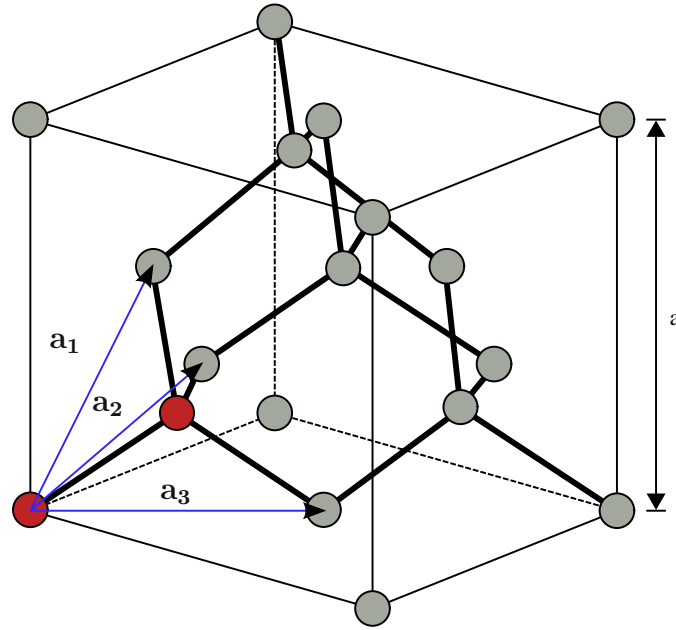


Figure 2.4: Crystallographic unit cell of the diamond structure. The primitive basis vectors and the two atoms forming the basis are shown.

Figure 2.4 depicts the structure of the diamond lattice, which is the lattice of group IV semiconductors such as Si and Ge. The basis consists of two atoms at $(0, 0, 0)$ and $\frac{a_0}{4}(1, 1, 1)$ and the basis vectors \mathbf{a}_1 , \mathbf{a}_2 and \mathbf{a}_3 . The lattice can also be described as two inter-penetrating face centered cubic (fcc) lattices, one displaced from the other by a translation of $\frac{a_0}{4}(1, 1, 1)$ along a body diagonal.

For group IV semiconductors the two basis atoms are identical, whereas for III-V semiconductors such as GaAs, AlAs, InAs, or InP the basis atoms are different and the structure is called the zinc-blende structure.

The basis vectors of the Bravais lattice read

$$\mathbf{a}_1 = \frac{a_0}{2} \begin{pmatrix} 0 \\ 1 \\ 1 \end{pmatrix}, \quad \mathbf{a}_2 = \frac{a_0}{2} \begin{pmatrix} 1 \\ 0 \\ 1 \end{pmatrix}, \quad \text{and} \quad \mathbf{a}_3 = \frac{a_0}{2} \begin{pmatrix} 1 \\ 1 \\ 0 \end{pmatrix}. \quad (2.22)$$

The lattice is invariant for all translations from a lattice vector \mathbf{R}_0 to a lattice vector \mathbf{R} of the form

$$\mathbf{R} = \mathbf{R}_0 + i\mathbf{a}_1 + j\mathbf{a}_2 + k\mathbf{a}_3, \quad (2.23)$$

where i, j and k are integers.

2.5 The Strained Diamond Structure

Generally, applying strain to a crystal reduces its symmetry. The basis vectors \mathbf{a}_i of the strained Bravais lattice can be directly obtained by a transformation of the vectors \mathbf{a}_i of the unstrained crystal [Bir74]

$$\mathbf{a}_i' = (\mathbb{1} + \underline{\varepsilon}) \cdot \mathbf{a}_i . \quad (2.24)$$

The volume of the strained primitive cell can be obtained as

$$\Omega_0' = \Omega_0(1 + \varepsilon_H) , \quad (2.25)$$

where ε_H is the hydrostatic strain component

$$\varepsilon_H = \varepsilon_{xx} + \varepsilon_{yy} + \varepsilon_{zz} . \quad (2.26)$$

Strain can also cause a change of the Bravais lattice type. The resulting Bravais lattice can be determined by looking up Figure 2.3. Since it is not straight forward to find the transitions between lattice types by intuition the following guidance may be convenient.

- The relaxed diamond structure is a face centered cubic system.
- If the face centered cubic cell is distorted along one of the orthogonal directions the cell is transformed to the centered tetragonal system. The face centered tetragonal system is equivalent to the volume centered system.
- Distorting the centered tetragonal cell along one of the orthogonal directions within the squared plane leads to the face centered orthorhombic cell.
- Applying strain to the centered tetragonal cell along one of the orthogonal directions within the squared plane leads to the face centered orthorhombic cell.
- By applying arbitrary shear strain components to the face centered orthorhombic cell it is further degraded to the triclinic lattice.
- As a special case the face centered orthorhombic cell can also be sheared to the volume centered triclinic system.

2.5.1 The Point Group Symmetry Operations

To describe the lattice symmetry properties on a more formal basis a definition of the possible point operations is needed:

E	unity operation
n_k^+	clockwise rotation of angle $2\pi/n$ around axis \mathbf{r}_k
n_k^-	counter-clockwise rotation of angle $2\pi/n$ around axis \mathbf{r}_k
I	inversion
\bar{n}_k^+	clockwise rotation of angle $2\pi/n$ around axis \mathbf{r}_k followed by inversion
\bar{n}_k^-	counter-clockwise rotation of angle $2\pi/n$ around axis \mathbf{r}_k followed by inversion

where \mathbf{r}_k is in one out of five sets of rotation axes

$$\begin{aligned}
 \mathbf{r}_i &= (1, 0, 0), (0, 1, 0), (0, 0, 1) \\
 \mathbf{r}_{i''} &= (0, 1, 0), (\sqrt{3}, -1, 0), (-\sqrt{3}, -1, 0) \\
 \mathbf{r}_j &= (1, 1, 1), (-1, -1, 1), (1, -1, -1), (-1, -1, -1) \\
 \mathbf{r}_p &= (1, 1, 0), (-1, 1, 0), (1, 0, 1), (0, 1, 1), (-1, 0, 1), (0, -1, 1) \\
 \mathbf{r}_s &= (1, 1, 0), (-1, 1, 0)
 \end{aligned}$$

Table 2.2 [Yu03] lists the resulting point groups in Schönflies notation when applying strain to the diamond lattice. Starting point is the unstrained diamond structure denoted by O_h . $|P(\Gamma)|$ denotes the number of elements of the point group which is 48 for O_h and is decreased under strain as indicated in the table.

point group	symmetry elements	$ P(\Gamma) $	stress direction
O_h	E 2_i 3_j^+ 3_j^- 2_p 4_i^+ 4_i^- I $\bar{2}_i$ $\bar{3}_j^+$ $\bar{3}_j^-$ $\bar{2}_p$ $\bar{4}_i^+$ $\bar{4}_i^-$	48	unstrained
D_{4h}	E 4_z^+ 4_z^- 2_i 2_s I $\bar{4}_z^+$ $\bar{4}_z^-$ $\bar{2}_i$ $\bar{2}_s$	16	stress along $\langle 100 \rangle$
D_{3d}	E 3_z^+ 3_z^- $2_{i''}$ I $\bar{3}_z^+$ $\bar{3}_z^-$ $\bar{2}_{i''}$	12	stress along $\langle 111 \rangle$
D_{2h}	E 2_i I $\bar{2}_i$	8	stress along $\langle 110 \rangle$
C_{2h}	E 2_z I $\bar{2}_z$	4	stress along $\langle 120 \rangle$
S_2	E I	2	other directions

Table 2.2: Point group and symmetry elements of strained lattices that originate when stress is applied along various high symmetry directions to an initially cubic lattice O_h . Schönflies symbols are used to specify the point groups. $|P(\Gamma)|$ denotes the number of elements of the point group.

2.6 The Reciprocal Lattice

The basis vectors \mathbf{b}_i of the reciprocal lattice are related to the basis vectors \mathbf{a}_i of the Bravais lattice via

$$\mathbf{b}_i \cdot \mathbf{a}_j = 2\pi\delta_{ij} \quad (2.27)$$

Relations (2.27) and (2.22) give the reciprocal basis vectors

$$\mathbf{b}_1 = \frac{2\pi}{a_0} \begin{pmatrix} -1 \\ 1 \\ 1 \end{pmatrix}, \quad \mathbf{b}_2 = \frac{2\pi}{a_0} \begin{pmatrix} 1 \\ -1 \\ 1 \end{pmatrix}, \quad \text{and} \quad \mathbf{b}_3 = \frac{2\pi}{a_0} \begin{pmatrix} 1 \\ 1 \\ -1 \end{pmatrix}. \quad (2.28)$$

General reciprocal lattice vectors have the form

$$\mathbf{G}_{lmn} = l\mathbf{b}_1 + m\mathbf{b}_2 + n\mathbf{b}_3, \quad (2.29)$$

where l, m , and n are integers.

The unit cell of the reciprocal lattice is the Brillouin zone. It contains all points nearest to one enclosed lattice point. Due to periodicity of the reciprocal lattice only the first Brillouin zone has to be considered for band structure calculation. The shape of the first Brillouin zone is determined by the boundary faces

$$|k_x| + |k_y| + |k_z| = \frac{3}{2} \frac{2\pi}{a_0}, \quad |k_x| = \frac{2\pi}{a_0}, \quad |k_y| = \frac{2\pi}{a_0}, \quad \text{and} \quad |k_z| = \frac{2\pi}{a_0}. \quad (2.30)$$

These faces are constructed by finding the reciprocal lattice vectors pointing from the origin to the fourteen nearest lattice points and take perpendicular planes to these vectors at a position where the planes bisect the vectors [Jungemann03].

The volume for band structure calculation can be further reduced by taking into account that the symmetry operations for the reciprocal lattice are the same as for the Bravais lattice. Therefore the symmetry elements given in Table 2.2 can be directly applied to the reciprocal lattice cell. The smallest possible domain in the Brillouin zone is termed the irreducible wedge. Figure 2.5 depicts the first Brillouin zone highlighting the irreducible wedge as well as one octant.

Figure 2.6 shows one octant of the Brillouin zone and a detailed view of the irreducible wedge with the location of some symmetry points as they are usually named in literature.

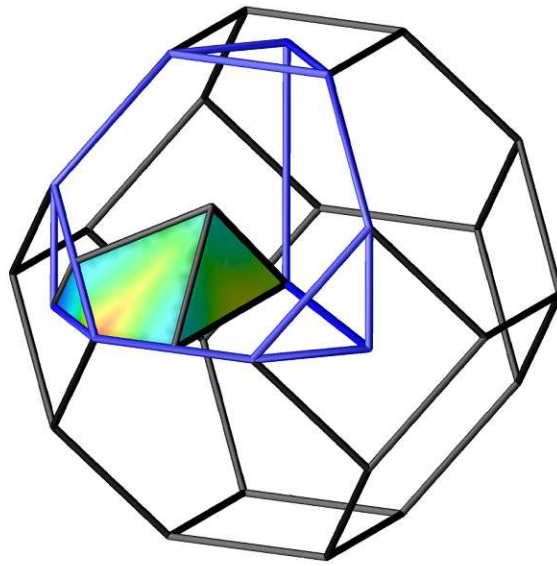


Figure 2.5: Brillouin zone of Si highlighting the first octant and the first irreducible wedge.

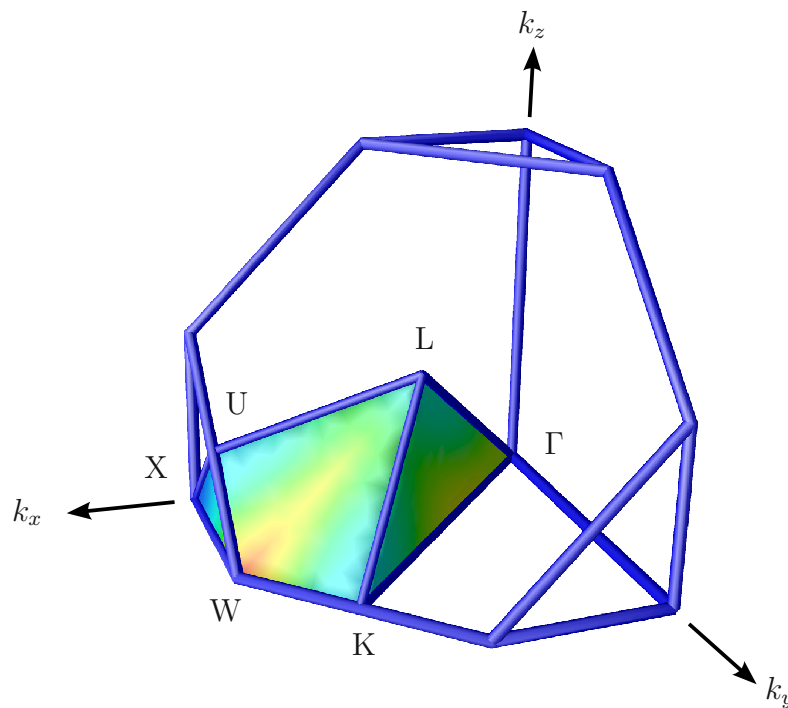


Figure 2.6: The irreducible wedge of the diamond structure showing important symmetry points.

2.6.1 The Relaxed Diamond Structure: O_h Symmetry

The point group O_h refers to the relaxed diamond structure. It contains 48 symmetry elements which are listed in Table 2.2. From these symmetry properties follows that the energy bands are invariant under eight reflections

$$\varepsilon_n(k_x, k_y, k_z) = \varepsilon_n(|k_x|, |k_y|, |k_z|) \quad (2.31)$$

and six permutations

$$\begin{aligned} \varepsilon_n(k_x, k_y, k_z) &= \varepsilon_n(k_x, k_z, k_y) = \varepsilon_n(k_y, k_x, k_z) = \\ \varepsilon_n(k_y, k_z, k_x) &= \varepsilon_n(k_z, k_x, k_y) = \varepsilon_n(k_z, k_y, k_x) . \end{aligned} \quad (2.32)$$

The choice of the irreducible wedge as shown in Figure 2.6 is not unique. If the irreducible wedge is allowed to exceed the borders of the Brillouin zone, simpler shapes can be found [Stanley98]. Figure 2.7 depicts the conduction and valence bands of unstrained Si along lines from one symmetry point to another.

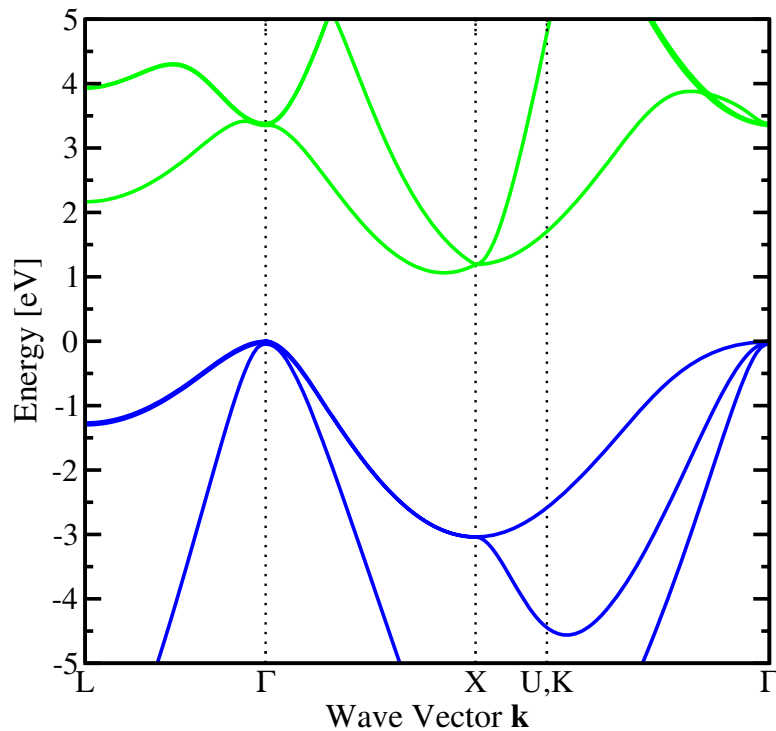


Figure 2.7: Valence and conduction bands of Si.

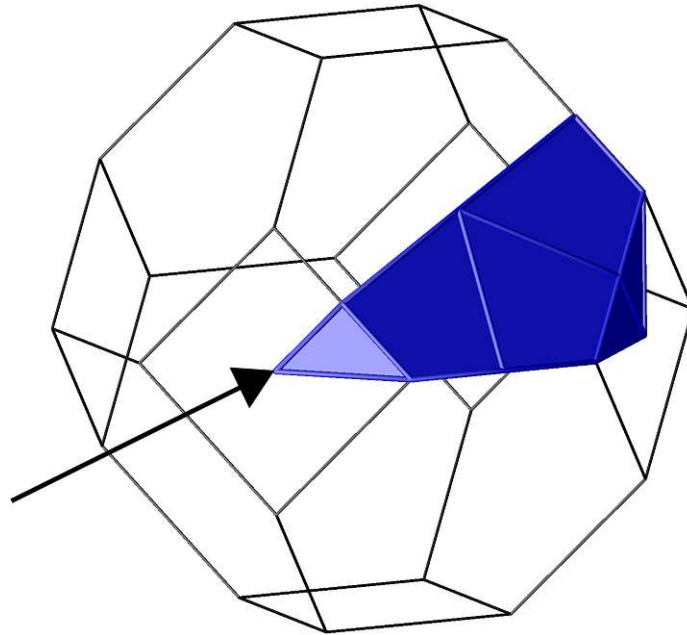


Figure 2.8: Irreducible wedge of a diamond structure strained along direction [100].

2.6.2 The Biaxially Strained Diamond Structure: D_{4h} Symmetry

Biaxial strain applied in a $\{001\}$ plane of a cubic lattice transforms the cell from O_h to the D_{4h} symmetry, a member of the tetragonal crystal class [Bir74]. The same symmetry reduction is observed, if uniaxial strain along a fourfold axis \mathbf{r}_i is applied. The point group D_{4h} has 16 remaining symmetry elements. The symmetry operations maintain invariance of the energy bands under reflections

$$\varepsilon_n(k_x, k_y, k_z) = \varepsilon_n(|k_x|, |k_y|, |k_z|) . \quad (2.33)$$

The invariance of the energy bands under permutation depends on the direction of stress, since only the indices perpendicular to the stress direction can be permuted, which gives in the case of stress along [100]

$$\varepsilon_n(k_x, k_y, k_z) = \varepsilon_n(k_x, k_z, k_y) . \quad (2.34)$$

Figure 2.8 shows a possible choice for the irreducible wedge of the D_h system. The wedge fits into the first octant of the Brillouin zone and has a volume of $\Omega_{\text{BZ}}/16$.

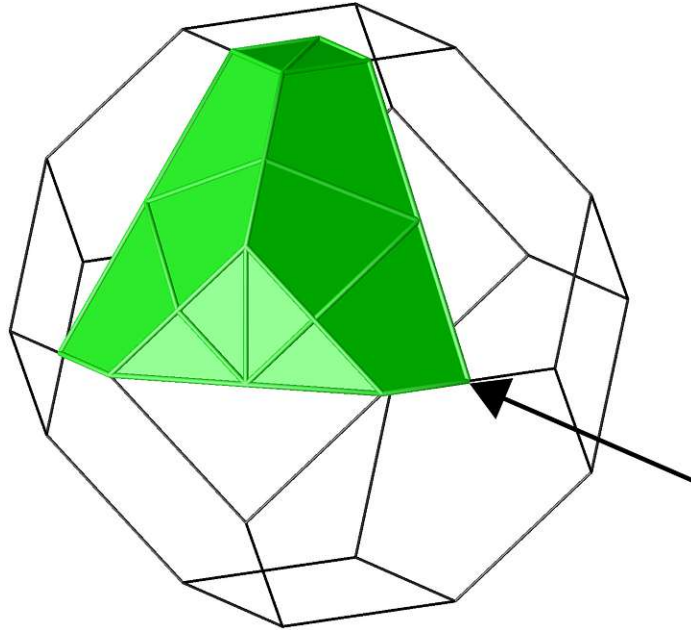


Figure 2.9: Irreducible wedge of a diamond structure stressed along direction $[110]$.

2.6.3 D_{2h} Symmetry

The cube of the crystal class O_h is converted to a parallelepiped of the orthorhombic system belonging to D_{2h} when uniaxial stress is applied along $\langle 110 \rangle$ or when biaxial strain is applied in a $\{110\}$ plane. Equation (2.19) exhibits the form of the strain tensor [Bir74] which includes off-diagonal elements. As a result the unit cube is sheared and the angles between the basis vectors are altered.

The D_{2h} group has only eight symmetry elements (given in Table 2.2). A possible irreducible wedge with a volume of $\Omega_{\text{BZ}}/8$ is depicted in Figure 2.9. The irreducible wedge is any of the eight octants of the Brillouin zone. It should be noted that the D_{2h} group can also be reached by applying strain to the O_h class along two of the three fourfold axes \mathbf{r}_i . In this case, the strain tensor consists of three different diagonal elements ε_{11} , ε_{22} , and ε_{33} and vanishing off-diagonal components.

2.6.4 S_2 Symmetry

Under arbitrary stress – that is stress along directions other than those given in Table 2.2 – no rotational symmetries remain. The crystal is invariant only under inversion and therefore a member of the crystal class S_2 . In this case half of the Brillouin zone must be chosen as the irreducible volume for band structure calculation and for the transport simulation.

2.6.5 Utilizing Symmetry Properties in Monte Carlo Simulation

Due to the symmetry properties of the reciprocal lattice the simulation domain is restricted to the first Brillouin zone. All wave vectors \mathbf{k} exceeding the first Brillouin zone are mapped back via subtracting a reciprocal lattice vector $\mathbf{G}_{i,j,k}$

$$\mathbf{k}^{\text{firstBZ}} = \mathbf{k} - \mathbf{G}_{i,j,k} . \quad (2.35)$$

As illustrated in the last section, only the irreducible wedge is needed as the actual simulation domain. Mapping a carrier back to the domain of the irreducible wedge is more complicated as a coordinate transformation is necessary after applying equation (2.35) and every possible shape of the irreducible wedge demands for its own set of transformation rules.

To keep the code simple only two sizes of the simulation domain are implemented in the simulator: if the irreducible wedge fits into the first octant then the first octant is chosen as the domain, if it exceeds the first octant one half of the Brillouin zone is chosen. Since these domains can be larger than the irreducible wedge it may be necessary to extend the original band structure data by permutation.

In the case of the first octant as the simulation domain the octants are numbered as shown in Figure 2.10. If the carrier crosses the Brillouin zone border in a first step it is mapped back by subtraction of a lattice vector. In a second step it is mapped into the first octant by a coordinate transformation. This coordinate transformation is simply realized by a set of mirror operations as shown in Table 2.3. The table entries indicate which of the coordinates k_x , k_y and k_z have to be mirrored for a

	0	1	2	3	4	5	6	7
0		x	y	xy	z	xz	yz	xyz
1	x		xy	y	xz	z	xyz	yz
2	y	xy		x	yz	xyz	z	xz
3	xy	y	x		xyz	yz	xz	z
4	z	xz	yz	xyz		x	y	xy
5	xz	z	xyz	yz	x		xy	y
6	yz	xyz	z	xz	y	xy		x
7	xyz	yz	xz	z	xy	y	x	

Table 2.3: Mirroring operations for transitions between octants of the Brillouin zone.

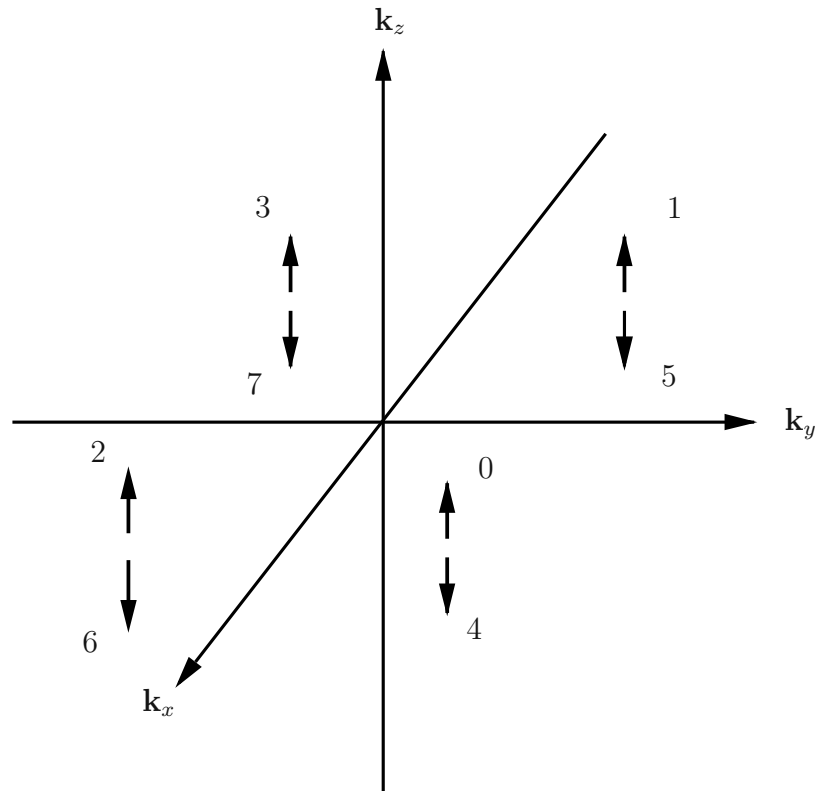


Figure 2.10: Numbering of the octants of the first Brillouin zone. The first octant is labeled 0.

specific transition from one octant to another. The transformation is applied to the particle \mathbf{k} -vector and to the force vector (see also equation of motion (3.3)).

If the carrier is crossing a border to another octant within the Brillouin zone, the mirror operations are applied to map it back to the first octant.

If one half of the Brillouin zone is used as the simulation domain there is only one mirroring operation: all three coordinates of the \mathbf{k} -vector and the force vector are mirrored if a transition from one halfspace to the other occurs.

Chapter 3

The Semiclassical Transport Model

As computational power raises and more efficient new Monte Carlo algorithms are developed, the Monte Carlo approach to solve the Boltzmann equation for TCAD device simulation is getting more and more important. In this work the Boltzmann equation – originally developed to describe the flow of kinetic gases – is used with extensions to meet the properties of quantum mechanical transport occurring for electron or hole ensembles in crystals. These extensions include particle kinetics depending on a position-dependent band structure and on scattering events, which are calculated quantum-mechanically using Fermi’s Golden Rule. The carrier motion consists of periods of collisionless acceleration caused by external forces, interrupted by instantaneous scattering events. The Monte Carlo approach solves the semiclassical Boltzmann transport equation [Kosina00].

During this work our in-house Monte Carlo tool named VMC [IuE06] was further developed in general and extended by a FBMC part. This chapter gives an overview of the used Monte Carlo models and algorithms with focus on the numerical methods used for CPU time efficient FBMC simulation.

3.1 The Equations of Motion

The semiclassical Hamilton function $H_n^e(\mathbf{r}, \mathbf{k}, t)$ for an electron in a conduction band is given by

$$H_n^e(\mathbf{r}, \mathbf{k}, t) = E_c(\mathbf{r}) + \varepsilon_n(\mathbf{r}, \mathbf{k}) - e\psi(\mathbf{r}, t) \quad (3.1)$$

where E_c is the conduction band edge, ε_n is the energy of the n -th band relative to the conduction band edge, ψ is the electrostatic potential, \mathbf{r} is the position, \mathbf{k} is the wave vector of the carrier, and e the elementary charge. The Hamilton function for holes reads

$$H_n^h(\mathbf{r}, \mathbf{k}, t) = -E_v(\mathbf{r}) + \varepsilon_n(\mathbf{r}, \mathbf{k}) + e\psi(\mathbf{r}, t) \quad (3.2)$$

where E_v is the valence band edge. The collisionless motion of the carriers is described by the equations of motions given by Newton's law

$$\hbar \frac{\partial \mathbf{k}}{\partial t} = -\nabla_{\mathbf{r}} H = \mathbf{F} \quad (3.3)$$

and the carrier group velocity

$$\frac{\partial \mathbf{r}}{\partial t} = \frac{1}{\hbar} \nabla_{\mathbf{k}} H = \mathbf{v}(\mathbf{r}, \mathbf{k}). \quad (3.4)$$

Here, \hbar is the reduced Planck constant, \mathbf{F} denotes the force and \mathbf{v} the group velocity. In the semiclassical Monte Carlo framework the velocity \mathbf{v}_n for a carrier in the band n is the group velocity of the wave packet of the carrier and follows from (3.4)

$$\mathbf{v}_n(\mathbf{r}, \mathbf{k}) = \frac{1}{\hbar} \nabla_{\mathbf{k}} \varepsilon_n(\mathbf{r}, \mathbf{k}). \quad (3.5)$$

The force \mathbf{F} denotes

$$\mathbf{F}_n^e(\mathbf{r}, \mathbf{k}, t) = \nabla_{\mathbf{r}}(-E_c(\mathbf{r}) + e\psi(\mathbf{r}, t) - \varepsilon_n(\mathbf{r}, \mathbf{k})) \quad (3.6)$$

for electrons and

$$\mathbf{F}_n^h(\mathbf{r}, \mathbf{k}, t) = \nabla_{\mathbf{r}}(E_v(\mathbf{r}) - e\psi(\mathbf{r}, t) - \varepsilon_n(\mathbf{r}, \mathbf{k})) \quad (3.7)$$

for holes.

3.2 The Boltzmann Transport Equation

Because of the nature of scattering as a random process it is impossible to determine the path of a carrier exactly. Instead a stochastic approach is used where the carrier

gas is described by a distribution function $f_n(\mathbf{r}, \mathbf{k}, t)$. This distribution function is related to the total number of particles N_{tot} in the system by

$$N_{\text{tot}} = \frac{2}{(2\pi)^3} \sum_n \int_{\Omega} \int_{\text{BZ}} f_n(\mathbf{r}, \mathbf{k}, t) d^3k d^3r. \quad (3.8)$$

The integral in real space is hereby over the whole device domain Ω whereas the integral in \mathbf{k} -space is over the first Brillouin zone (BZ), $1/(2\pi)^3$ is the minimum phase-space volume of a particle and the factor of two originates from the two possible spin states of the carriers. The semiclassical Boltzmann equation reads then

$$\left\{ \frac{\partial}{\partial t} + \mathbf{F}_n^{\text{T}}(\mathbf{r}, \mathbf{k}, t) \frac{1}{\hbar} \nabla_{\mathbf{k}} + \mathbf{v}_n^{\text{T}}(\mathbf{r}, \mathbf{k}) \nabla_{\mathbf{r}} \right\} f_n(\mathbf{r}, \mathbf{k}, t) = S_{\text{SC}}(\mathbf{r}, \mathbf{k}, t). \quad (3.9)$$

The left hand side is derived from the equations of motion (3.2) and (3.3). S_{SC} is the scattering integral given by

$$S_{\text{SC}} = \frac{\Omega}{(2\pi)^3} \sum_{n'} \int_{\text{BZ}} (1 - f_n(\mathbf{r}, \mathbf{k}, t)) S_{n,n'}(\mathbf{k}|\mathbf{k}')(\mathbf{r}, t) f_{n'}(\mathbf{r}, \mathbf{k}', t) - (1 - f_{n'}(\mathbf{r}, \mathbf{k}', t)) S_{n',n}(\mathbf{k}|\mathbf{k}')(\mathbf{r}, t) f_n(\mathbf{r}, \mathbf{k}, t) d^3k'. \quad (3.10)$$

S_{SC} describes the transition from a state $(n', \mathbf{r}, \mathbf{k}')$ into a state $(n, \mathbf{r}, \mathbf{k})$ and the inverse process. The rate for a transition from an initial state $(n', \mathbf{r}, \mathbf{k}')$ to a final state $(n, \mathbf{r}, \mathbf{k})$ is proportional to the probabilities that the initial state is occupied, $f_{n'}(\mathbf{r}, \mathbf{k}', t)$, and that the final state is not occupied, $(1 - f_n(\mathbf{r}, \mathbf{k}, t))$, and to the transition rate $S_{n,n'}(\mathbf{k}|\mathbf{k}')(\mathbf{r}, t)$. The factor $(1 - f_n(\mathbf{r}, \mathbf{k}, t))$ stems from the Pauli exclusion principle.

The Boltzmann equation in the form of (3.9) is non-linear, because the transition rate may depend on the carrier distribution and the scattering integral includes a product of the distribution function with itself. The latter can be avoided if the Pauli exclusion principle is neglected. If additionally it is assumed, that the transition rate does not depend on the distribution function, we achieve the linear Boltzmann equation

$$\left\{ \frac{\partial}{\partial t} + \mathbf{F}_n^{\text{T}}(\mathbf{r}, \mathbf{k}) \frac{1}{\hbar} \nabla_{\mathbf{k}} + \mathbf{v}_n^{\text{T}}(\mathbf{r}, \mathbf{k}) \nabla_{\mathbf{r}} + S_n(\mathbf{r}, \mathbf{k}) \right\} f_n(\mathbf{r}, \mathbf{k}, t) = \frac{\Omega}{(2\pi)^3} \sum_{n'} \int_{\text{BZ}} S_{n,n'}(\mathbf{k}|\mathbf{k}') f_{n'}(\mathbf{r}, \mathbf{k}', t) d^3k'. \quad (3.11)$$

The scattering rate $S_n(\mathbf{r}, \mathbf{k})$ is the rate at which carriers are scattered out of their initial state and is defined as

$$S_n(\mathbf{r}, \mathbf{k}) = \frac{\Omega}{(2\pi)^3} \sum_{n'} \int_{\text{BZ}} S_{n,n'}(\mathbf{k}'|\mathbf{k}) d^3k'. \quad (3.12)$$

Equation (3.11) describes the kinetics of a carrier ensemble where the particles are considered independent and noninteracting.

3.3 Scattering Mechanisms

In this work scattering is treated on the basis of Fermi's Golden Rule [Landau81]

$$S_{if} = \frac{2\pi}{\hbar} |M_{if}(t)|^2 \delta(\varepsilon - \varepsilon_f). \quad (3.13)$$

Here, S_{if} is the transition probability from the initial state i to the final state f and ε_f is the energy of the final state. The matrix element $M_{if}(t)$ is given by

$$M_{if}(t) = \int \Psi_i^* V(t) \Psi_f d^3r, \quad (3.14)$$

where Ψ_i and Ψ_f are the wave functions of the initial and final state, respectively. $V(t)$ is the perturbation potential.

The density of states per spin of a band n is given by

$$g_n(\varepsilon) = \frac{1}{(2\pi)^3} \int_{\text{cell}} \delta(\varepsilon - \varepsilon_n(\mathbf{k})) d^3k. \quad (3.15)$$

The density of states integral can be evaluated numerically as for FBMC simulation or approximated by analytical expressions. Following the approach of Jacoboni [Jacoboni83] an analytical description for the conduction bands is derived by approximating the minima of the conduction bands – the so called valleys – by using the bandform function

$$\gamma^v(\varepsilon) = \frac{\hbar^2}{2} \sum_{i,j=1}^3 k_i \frac{1}{m_{ij}^v} k_j = \quad (3.16)$$

$$(\varepsilon^v(\mathbf{k}) - \varepsilon_0^v) (1 + \alpha^v(\varepsilon^v(\mathbf{k}) - \varepsilon_0^v)) = \varepsilon (1 + \alpha^v \varepsilon),$$

v_n	Volume Boundaries
1 :	$k_x \geq k_y \quad \wedge \quad k_x \geq k_z $
2 :	$-k_x \geq k_y \quad \wedge \quad -k_x \geq k_z $
3 :	$k_y \geq k_x \quad \wedge \quad k_y \geq k_z $
4 :	$-k_y \geq k_x \quad \wedge \quad -k_y \geq k_z $
5 :	$k_z \geq k_x \quad \wedge \quad k_z \geq k_y $
6 :	$-k_z \geq k_x \quad \wedge \quad -k_z \geq k_y $

Table 3.1: The six volumes in the first Brillouin representing the six X-valleys of the first conduction band.

where v denotes the valley index and ε is the energy relative to the valley energy offset ε_0^v . One can include strain effects by introducing for each valley strain-dependent effective mass tensors m_{ij}^v , nonparabolicity coefficients α^v , and valley energy offsets. If α^v is set to zero the shape of the band approximation simplifies from nonparabolic to parabolic. The density of states of a nonparabolic band can be written as

$$g^v(\varepsilon) = \frac{1}{\sqrt{2}} \frac{\{m_{\text{dos}}^v\}^{3/2}}{\pi^2 \hbar^3} \sqrt{\gamma^v(\varepsilon)} (1 + 2\alpha^v \varepsilon), \quad (3.17)$$

where m_{dos}^v is the density of states effective mass of the v -th valley, which can be obtained from the effective mass tensor

$$m_{\text{dos}}^v = \sqrt[3]{m_{11}^v m_{22}^v m_{33}^v}. \quad (3.18)$$

The approach to use valley-dependent scattering models can be adapted from Monte Carlo with analytical band structure models to fit into the framework of FBMC [Jungemann03]. The first Brillouin zone of the first conduction band of Si is divided into six volumes v_n as defined in Table 3.1 where v_n indices the v -th valley in the n -th band. The same approximation is also applied to the higher conduction bands. This approach is in the spirit of the analytical many valley model [Jacoboni83]. In combination with constant matrix elements it gives a CPU efficient formulation of the scattering rates, because scattering rates are proportional to the density of states, which is calculated numerically from the full-band structure.

3.3.1 Phonon Scattering

The transition rate from an initial state (v, \mathbf{k}) to a final state (v', \mathbf{k}') for phonon scattering in a non-polar semiconductor can be written as [Jacoboni83]

$$\{S^{\text{abs}}\}^{v'v}(\mathbf{k}'|\mathbf{k}) = \frac{\pi}{\rho\Omega\omega_q} \left(N_q + \frac{1}{2} \mp \frac{1}{2} \right) \mathcal{O} |D_{ij}q_j \xi_i|^2 \delta[\varepsilon^{v'}(\mathbf{k}') - \varepsilon^v(\mathbf{k}) \mp \hbar\omega_q] \quad (3.19)$$

Here, the upper and lower signs denote phonon absorption and emission, respectively. The rate depends on the the phonon number N_q , the momentum transfer $\mathbf{q} = \mathbf{k} - \mathbf{k}'$, the deformation potential tensor D_{ij} , the mass density of the crystal ρ , the overlap integral \mathcal{O} , the phonon angular frequency ω_q and its polarization ξ_i .

The overlap integral

$$\mathcal{O} = \left| \int_{BZ} u_{\mathbf{k}'}^*(\mathbf{r}) u_{\mathbf{k}}(\mathbf{r}) \exp(i\mathbf{G} \cdot \mathbf{r}) d^3r \right|^2 \quad (3.20)$$

depends on the type of transition. For intravalley transitions of electrons it is common to set \mathcal{O} to unity, which is exact only for wave functions of pure s -states or for exact plane waves [Jacoboni83]. The lowest conduction band of cubic semiconductors is a mixture of a s and p -type states and so overlap factors less than unity are obtained. Since for both intra- and intervalley transitions the overlap factors \mathcal{O} were found to be almost constant [Reggiani73] the values for \mathcal{O} can be included in the coupling constants.

The phonon number N_q is given by the Bose-Einstein statistics

$$N_q = \frac{1}{\exp\left(\frac{\hbar\omega_q}{k_B T_L}\right) - 1}, \quad (3.21)$$

where T_L denotes the lattice temperature and k_B the Boltzmann constant.

Acoustic Intravalley Scattering at Room Temperature

Since at room temperature the acoustic phonon energy $\hbar\omega_q$ is very small compared to the thermal energy $k_B T_L$ the expression for the transition rate for acoustic intravalley scattering can be simplified by using the elastic and equipartition approximation. Within the latter approximation the Bose-Einstein statistics (3.21) is replaced by its first order Taylor expansion which gives for the phonon population N_q

$$N_q \simeq \frac{k_B T_L}{\hbar\omega_q} - \frac{1}{2}. \quad (3.22)$$

Symbol	Value	Units
ρ	2.33 ^a	g/cm ³
u_s	9.05 ^b	cm/sec
$\Xi_{\text{adp}}^{\Delta}$	9.0 ^b	eV
$\hbar\omega_{\text{op}}$	61.2 ^c	meV
$D_t K_L$	1.75 ^c	10 ⁸ eV/cm

^a [Jacoboni83], ^b [Jungemann03], ^c [Fischetti96b]

Table 3.2: Parameters for acoustic and optical intravalley phonon scattering in Si.

The phonon dispersion relation for small \mathbf{q} is approximated as $\omega(\mathbf{q}) \simeq u_s q$. Thus, (3.19) becomes

$$\{S_{\text{ac}}^{\text{abs}}\}^v(\mathbf{k}', \mathbf{k}) = \frac{\pi q \{\Xi_{\text{adp}}^v\}^2}{\Omega u_s \rho} \left(\frac{k_B T_L}{\hbar q u_s} \mp \frac{1}{2} \right) \delta[\varepsilon^v(\mathbf{k}') - \varepsilon^v(\mathbf{k}) \pm \hbar\omega_q], \quad (3.23)$$

where u_s denotes the average sound velocity and ρ is the mass density of the crystal. Ξ_{adp}^v is the acoustic deformation potential of the v -th valley, which is derived by averaging the two non-zero elements of the deformation potential tensor over the polar angle [Jacoboni83].

In the elastic approximation the phonon energy is neglected, $\hbar\omega_q = u_s q \rightarrow 0$. Therefore, emission and absorption processes are equivalent and the transition probabilities can be added. This leads to a scattering rate for acoustic intraband scattering which is a function of energy only

$$\{S_{\text{ac}}\}^v(\varepsilon) = \frac{2\pi k_B T_L \{\Xi_{\text{adp}}^v\}^2}{\hbar u_s^2 \rho} g^v(\varepsilon). \quad (3.24)$$

In (3.24), $g^v(\varepsilon)$ denotes the density of states of valley v . The values of the parameters used in (3.24) can be found in Table 3.3.1.

Acoustic Intravalley Scattering at Low Temperatures

When the lattice temperature is very low (3.22) does not hold anymore and the dependence on the acoustic phonon energy and momentum transfer have to be considered. Using a model in which the phonon dispersion has to be evaluated during simulation will demand long calculation times. Therefore it is useful to derive a

temperature-dependent but otherwise constant mean phonon energy $\langle \varepsilon_{ac} \rangle = \hbar\omega_{ac}$ and formulate the acoustic intraband scattering rate as [R.-Bolívar05] [Bufler01]

$$\{S_{ac}^{emi}\}^v(\varepsilon) = \frac{\pi \Xi_{adp}^2 \langle q \rangle}{\rho u_s} \left(N_{ac} + \frac{1}{2} \mp \frac{1}{2} \right) g^v(\varepsilon \pm \hbar\omega_{ac}) . \quad (3.25)$$

To obtain the average momentum transfer $\langle q \rangle$ a mean momentum transfer \bar{q} is calculated first by taking an average over the solid angle Ω

$$\bar{q}(\varepsilon) = \frac{1}{4\pi} \oint q d\Omega = \frac{1}{2} \int k \sqrt{1 - 2 \cos(\vartheta)} \sin(\vartheta) d\vartheta = \frac{4}{3} k . \quad (3.26)$$

This result is used to take a second average with the equilibrium distribution function, i.e., the Maxwell-Boltzmann distribution

$$\langle q \rangle = \frac{\int_0^\infty \bar{q}(\varepsilon) e^{-\varepsilon/k_B T_L} g(\varepsilon) d\varepsilon}{\int_0^\infty e^{-\varepsilon/k_B T_L} g(\varepsilon) d\varepsilon} . \quad (3.27)$$

With a parabolic band approximation $\langle q \rangle$ evaluates to

$$\langle q \rangle = \frac{\frac{4}{3} \frac{\sqrt{2m^*}}{\hbar} (k_B T)^{\frac{1}{2}}}{0.886} , \quad (3.28)$$

where m^* is the effective electron mass. Now, the average phonon energy is obtained by assuming a linear dispersion relation

$$\langle \varepsilon_{ac} \rangle = \hbar u_s \langle q \rangle . \quad (3.29)$$

Optical Intravalley Scattering

From the matrix element theorem one can derive that optical intravalley scattering occurs only in the conduction band valleys along the $\langle 111 \rangle$ directions [Harrison56]. Thus this type of scattering is important in Ge. In Si it contributes only at high electron energies.

By replacing $\Xi^2 q^2 \xi^2$ in (3.19) with a squared optical coupling constant the scattering probability can be reformulated with a squared optical coupling constant $\{D_t K^v\}^2$ [Jacoboni83]. The optical phonon energies $\hbar\omega_{op}$ and the phonon number $N_q = N_{op}$ can be assumed to be constant since the dispersion curve is nearly flat for

phonons involved in optical intraband transitions. If the overlap factor \mathcal{O} is lumped in the coupling constant the resulting transition rate can be written as

$$\{S_{\text{op}}^{\text{abs}}\}^v(\mathbf{k}', \mathbf{k}) = \frac{\pi}{\rho\Omega\omega_{\text{op}}} \left(N_{\text{op}} + \frac{1}{2} \mp \frac{1}{2} \right) \{D_t K^v\}^2 \delta[\varepsilon^v(\mathbf{k}') - \varepsilon^v(\mathbf{k}) \mp \hbar\omega_{\text{op}}] . \quad (3.30)$$

With the above formulation the scattering rate for optical phonons is a function of the final energy $\varepsilon \pm \hbar\omega_{\text{op}}$

$$\{S_{\text{op}}^{\text{abs}}\}^v(\varepsilon) = \frac{\pi \{D_t K^v\}^2}{\rho\omega_{\text{op}}} \left(N_{\text{op}} + \frac{1}{2} \mp \frac{1}{2} \right) g^v(\varepsilon \pm \hbar\omega_{\text{op}}) . \quad (3.31)$$

The values used for optical intravalley scattering are given in Table 3.3.1.

Intervalley Phonon Scattering

Both acoustic and optical phonons can cause electron transitions between states in different conduction band valleys [Harrison56, Conwell67]. The scattering rate for intervalley scattering out of a valley v for a phonon mode η reads

$$\{S_{\eta}^{\text{abs}}\}^v(\varepsilon) = \sum_{v' \neq v} \frac{\pi \{D_t K_{\eta}^{v'v}\}^2 Z^{v'}}{\rho\omega_{\eta}} \left(N_{\eta} + \frac{1}{2} \mp \frac{1}{2} \right) g^{v'}(\varepsilon^{v'} \pm \hbar\omega_{\eta} - \Delta\varepsilon^{v'v}) . \quad (3.32)$$

The possible final valleys v' are determined by two selection rules for the phonon mode η : g -type phonons induce transitions between opposite valleys on the same axis in \mathbf{k} space, and f -type phonons induce transitions among orthogonal axes. The coupling constants $\{D_t K_{\eta}^{v'v}\}$ depend on the phonon branch η and the initial and final valley in a particular transition. $Z^{v'}$ denotes the number of possible final equivalent valleys in a transition, N_{η} is the phonon number, and $\Delta\varepsilon^{v'v}$ is the energy difference between the minima of the final and initial valley.

The numerical values for the bulk phonon scattering rates are summarized in Table 3.3.

Figure 3.1 depicts the low field electron mobility over temperature. This result is obtained by Monte Carlo simulation including only phonon scattering and agrees very well with simulation data from [Canali75]. Because of the influence of impurity scattering the mobility obtained from experimental data is lower in the low temperature regime.

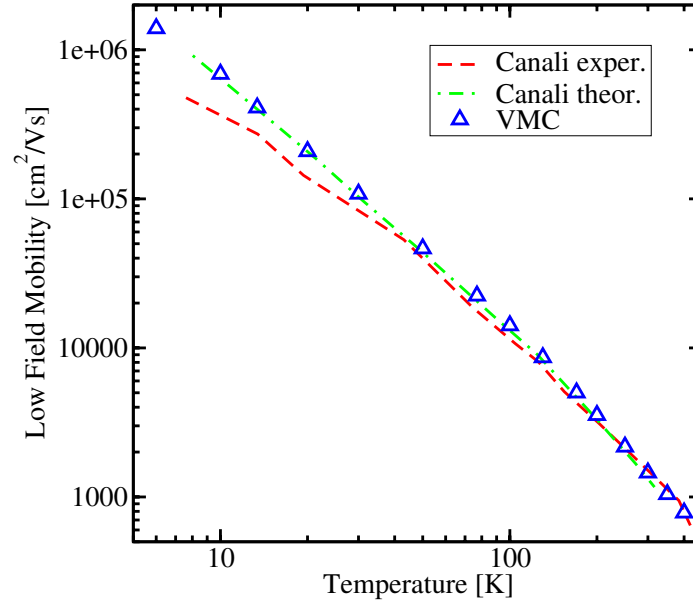


Figure 3.1: Low field electron mobility in Si versus lattice temperature as a result of Monte Carlo simulation (VMC) compared to experimental and theoretical data [Canali75].

Phonon Mode η	$D_t K$ [MeV/cm]	$\hbar\omega$ [meV]	Selection Rule r
Transversal acoustic	50	12.06	g
Longitudinal acoustic	80	18.53	g
Longitudinal optical	1100	62.04	g
Transversal acoustic	30	18.86	f
Longitudinal acoustic	200	47.39	f
Transversal optical	200	59.03	f

Table 3.3: Phonon modes, coupling constants, phonon energies, and selection rule for Si as used in the analytical intervalley phonon scattering model. Values are taken from [Jacoboni83].

Full-Band Phonon Scattering

As explained in the introduction of Section 3.3, the many-valley approach for analytical band models is adapted for the full-band framework. The differences in the formulation of the scattering rates lie then in the analytical versus the numerical calculation of the density of states and the implementation of interband transitions. The transition rate of full-band acoustic intravalley scattering is derived by applying

Phonon Mode η	$D_t K$ [MeV/cm]	$\hbar\omega$ [meV]	Selection Rule r
Transversal acoustic	47.2	12.1	g
Longitudinal acoustic	75.5	18.5	g
Longitudinal optical	1042	62.0	g
Transversal acoustic	34.8	19.0	f
Longitudinal acoustic	232	47.4	f
Transversal optical	232	58.6	f
Holes acoustic	991	63.3	a

Table 3.4: Phonon modes, coupling constants, phonon energies, and phonon branch of inelastic phonon scattering for Si [Dhar06] as used in FBMC simulation.

Phonon Mode η	$D_t K$ [MeV/cm]	$\hbar\omega$ [meV]	Selection Rule r
Transversal acoustic	47.9	5.6	g
Longitudinal acoustic	77.2	8.6	g
Longitudinal optical	928	37.0	g
Transversal acoustic	283	9.9	f
Longitudinal acoustic	1940	28.0	f
Transversal optical	1690	32.5	f
Holes acoustic	3500	37.0	a

Table 3.5: Phonon modes, coupling constants, phonon energies, and phonon branch of inelastic phonon scattering for Ge [Jungemann03] as used in FBMC simulation.

the elastic approximation to (3.23)

$$\{S_{ac}\}^{n'n}(\mathbf{k}'|\mathbf{k}) = \frac{2\pi}{\hbar} \frac{k_B T_L \{\Xi_{adp}\}^2}{\Omega \rho u_s^2} \delta(\varepsilon_{n'}^v(\mathbf{k}') - \varepsilon_n^v(\mathbf{k})) \delta_{v_{n'}(\mathbf{k}'), v_n(\mathbf{k})}. \quad (3.33)$$

The deformation potentials Ξ are assumed to be 8.5 eV for electrons and 5.12 eV [Dhar06] for holes in Si [Dhar06] and 8.79 eV for electrons and 7.40 eV for holes in Ge [Jungemann03]. The Kronecker delta term on the right hand side defines that transitions are allowed only within a valley v , but between different bands n' and n . The probability to scatter to another band n is determined by the contribution of the density of states in this band at the final energy.

For the simulation of SiGe alloys the parameter values for Si and Ge are linearly interpolated according to the material composition. Since only the Δ -valleys are considered in the implemented full-band scattering formalism, simulation of SiGe compounds is only valid as long as the Δ -valleys are dominantly populated.

The coupling constants, phonon energies, and phonon modes η , and the selection rule r for inelastic full-band phonon scattering in Si are shown in Table 3.4. The coupling constants are taken from [Jacoboni83] and [Jungemann03] and are fine-tuned to match the measured data for biaxial strained Si [Dhar06]. Table 3.5 shows the respective values for Ge, which are used to calculate the interpolated parameter values of SiGe alloys.

The phonon branches determine a set of selection rules labeled $r(\eta, v(\mathbf{k}'), v(\mathbf{k}))$. In the full-band formulation these selection rules act on the density of states whereas the coupling constant is kept constant for all combination of valleys and bands. This leads to the expression

$$\begin{aligned} \{S_{\eta}^{\text{abs}}\}^{n,n'}(\mathbf{k}'|\mathbf{k}) &= \\ &= \frac{\pi \{D_t K_{\eta}\}^2}{V \rho \omega_{\eta}} \left(N_{\eta} + \frac{1}{2} \mp \frac{1}{2} \right) \delta(\varepsilon_{n'}(\mathbf{k}') \pm \hbar \omega_{\eta} - \varepsilon_n(\mathbf{k})) r(\eta, v(\mathbf{k}'), v(\mathbf{k})) \end{aligned} \quad (3.34)$$

for the transition rate due to intervalley phonon scattering. For holes there is no restriction in the selection of the final state by a selection rule and there is only one inelastic optical phonon mode.

Figure 3.2 shows the electron velocity for relaxed Si as a function of the electric field in [100] direction. It can be observed that the data from VMC agrees well with measurements.

Figure 3.3 depicts the hole velocity as a function of the electric field and Figure 3.4 the energy as a function of the electric field in [100] direction for relaxed Ge. These results are compared to values from literature [Fischetti96a][Yamada95][Ghosh06] and show good agreement.

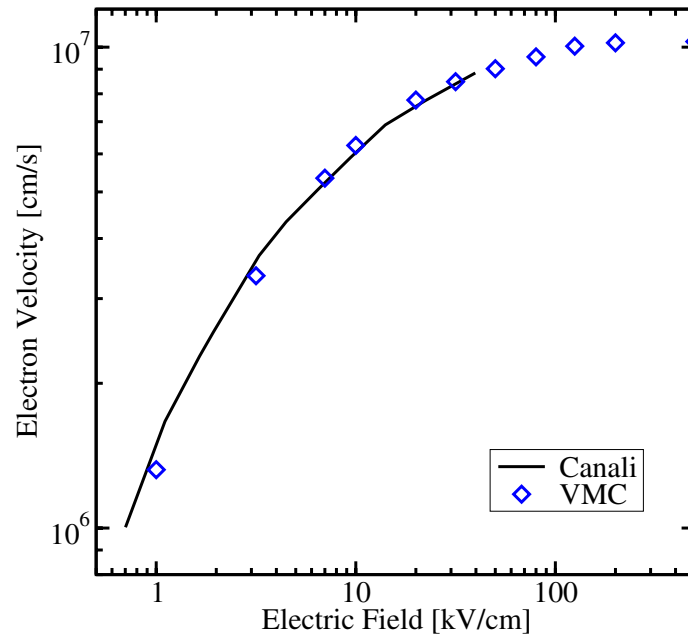


Figure 3.2: Electron velocity versus field in [100] direction for relaxed Si. Monte Carlo results (VMC) are compared to measurement [Canali75].

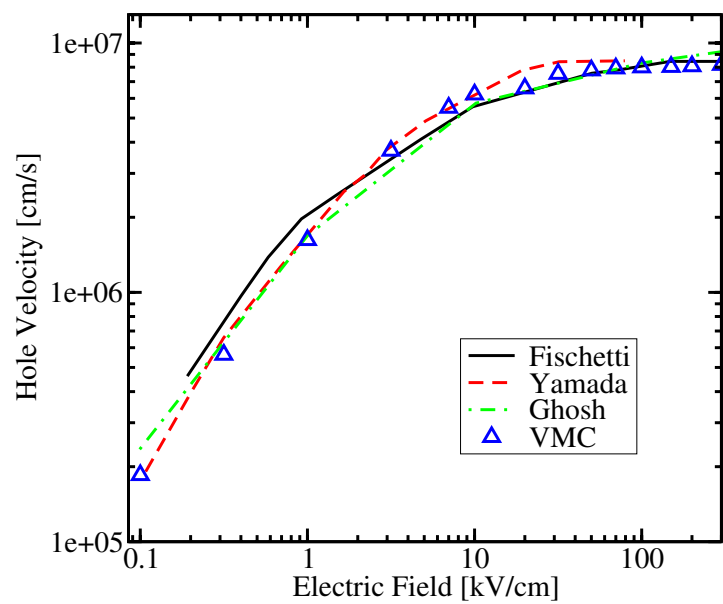


Figure 3.3: Hole velocity versus field in [100] direction for relaxed Ge. Monte Carlo results (VMC) are compared to results from literature [Fischetti96a][Yamada95][Ghosh06].

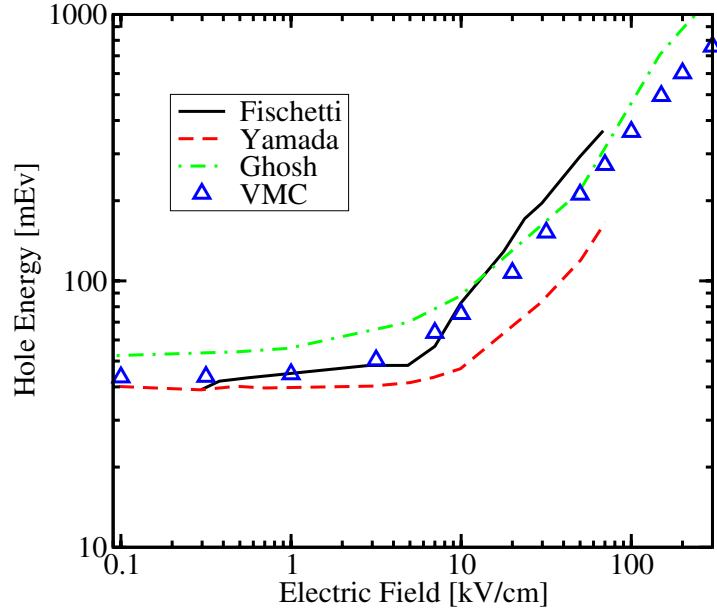


Figure 3.4: Hole energy versus field in [100] direction for relaxed Ge. Monte Carlo results (VMC) are compared to results from literature [Fischetti96a][Yamada95][Ghosh06].

3.3.2 Ionized Impurity Scattering

In this work the well known model of Brooks and Herring [Brooks51] is used in an extended form, where multi-potential scattering and dispersive screening is included. The Fourier transformed potential V_{BH} of a screened, ionized impurity is given by

$$V_{\text{BH}}(\mathbf{q}) = \frac{Ze}{4\pi\epsilon_0\epsilon_s} \frac{1}{q^2 + \beta_s^2}. \quad (3.35)$$

Here, Ze is the charge of the impurity center and β_s is the inverse Thomas-Fermi screening length

$$\beta_s^2 = \frac{e^2 n_I}{\epsilon_0 \epsilon_s k_B T_L} \frac{\mathcal{F}_{-1/2}(\eta)}{\mathcal{F}_{1/2}(\eta)}, \quad (3.36)$$

where n_I is the concentration of the impurity centers and \mathcal{F}_i denotes the Fermi integral of the i -th order with the reduced Fermi energy η as argument

$$\eta = \frac{\epsilon_F - \epsilon_C}{k_B T_L}. \quad (3.37)$$

Application of the Golden Rule (3.13) and the scattering potential (3.35) gives the transition rate

$$\{S_{\text{BH}}\}^{n'n}(\mathbf{k}'|\mathbf{k}) = \frac{2\pi}{\hbar} \left(\frac{Ze}{4\pi\epsilon_0\epsilon_s} \right)^2 \frac{1}{(q^2 + \beta_s^2)^2} \delta(\varepsilon_{n'}^v(\mathbf{k}') - \varepsilon_n^v(\mathbf{k})). \quad (3.38)$$

The ionized impurity scattering rate from the above potential can be formulated [Kosina98]

$$S_{\text{BH}} = C(k) \frac{1}{2\beta_s^2} \frac{b}{1+b}. \quad (3.39)$$

Here, $b = 4k^2/\beta_s^2$ and the prefactor $C(k)$ is set

$$C(k) = \frac{n_I Z^2 e^4}{2\pi \hbar^2 \epsilon_0^2 \epsilon_s^2 v_g(k)}, \quad (3.40)$$

where v_g denotes the magnitude of the group velocity. In the approximation based on non-parabolic analytic bands, the scattering rate for a valley v evaluates to

$$S_{\text{BH}}^{\text{NP}}(\varepsilon) = \frac{n_I Z^2 e^4}{2\sqrt{2}\pi(\epsilon_0\epsilon_s)^2 \varepsilon_{\beta,v}^2 \sqrt{m_v^*}} \sqrt{\gamma(\varepsilon)} \frac{1 + 2\alpha^v \varepsilon}{1 + \frac{4\gamma(\varepsilon)}{\varepsilon_{\beta,v}}}, \quad (3.41)$$

with

$$\varepsilon_{\beta,v} = \frac{\hbar^2 \beta_s^2}{2m_v^*}. \quad (3.42)$$

Multi-Potential Scattering and Dispersive Screening

The Brooks-Herring model significantly overestimates the mobility for higher impurity concentrations. To extend the validity of the model, multi-potential scattering and dispersive screening via Lindhard's dielectric function is included. Multi potential scattering to the first order considers only the Coulomb interaction of the carrier with pairs of impurities. The Fourier transform of the applied potential takes the form:

$$V_0(\mathbf{q}) = \frac{Ze}{4\pi\epsilon_0\epsilon_s|\mathbf{q}|^2} (1 + \exp(-i\mathbf{q}\mathbf{R})), \quad (3.43)$$

where \mathbf{R} is the distance between the centers.

V_t is the total potential which forms because of the response of the electrons to the applied potential V_0 . The total potential is related to the applied potential via the dielectric function $\epsilon(\mathbf{q}, \omega)$

$$V_t(\mathbf{q}) = \frac{V_0(\mathbf{q})}{\epsilon(\mathbf{q}, 0)}. \quad (3.44)$$

The frequency ω equals zero because the applied potential is time independent. When considering only low order screening effects, Lindhard's dielectric function is appropriate [Ferry91]:

$$\epsilon(\mathbf{q}, 0) = 1 + \frac{\beta_s^2}{q^2} G(\xi, \eta), \quad (3.45)$$

Here, $G(\xi, \eta)$ denotes the screening function for which an integral representation exists [Ferry91]

$$G(\xi, \eta) = \frac{1}{\mathcal{F}_{-1/2}(\eta)} \frac{1}{\xi\sqrt{\pi}} \int_0^\infty \frac{x}{1 + \exp(x^2 - \eta)} \ln \left| \frac{x + \xi}{x - \xi} \right| dx, \quad (3.46)$$

with

$$\xi^2 = \frac{\hbar^2 q^2}{8m^*k_B T_L}. \quad (3.47)$$

The integral (3.46) cannot be evaluated analytically, but there are attempts in literature to approximate it with a sufficiently accurate rational expression [Kosina98]. After combining equations (3.43)(3.44) and (3.45) and averaging the term $|1 + \exp(-i\mathbf{q}\mathbf{R})|^2$ over the solid angle $|V_t|^2$ is found as

$$|V_t(q)|^2 = \left(\frac{Ze}{4\pi\epsilon_0\epsilon_s} \right)^2 \frac{1}{(q^2 + \beta_s^2 G(\xi, \eta))^2} \left(1 + \frac{\sin(qR)}{qR} \right). \quad (3.48)$$

Equivalent Scattering Cross Section

The long range of the Coulomb force causes a large scattering cross section of a single ion. This makes Coulomb scattering occur very frequently and consume a

high amount of computation time during a Monte Carlo simulation. The momentum transfer per scattering event is rather small. This leads to a very anisotropic scattering behavior with a high percentage of small-angle scattering events.

The number of scattering events can be significantly reduced by the introduction of an isotropic equivalent scattering cross section $\tilde{\sigma}$, which has the same momentum relaxation time as the original cross section σ . These cross sections are related by [Kosina97]

$$\tilde{\sigma}(k, \cos(\theta)) = \frac{1}{2} \int_{-1}^1 (1 - \cos \theta) \sigma(k, \cos \theta) d \cos \theta, \quad (3.49)$$

where θ is the angle between \mathbf{k} and \mathbf{k}' . The equivalent total scattering rate \tilde{S}_{BH} is

$$\tilde{S}_{\text{BH}} = 2\pi n_{\text{I}} v_{\text{g}}(k) \int_{-1}^1 (1 - \cos \theta) \sigma(k, \cos \theta) d \cos \theta. \quad (3.50)$$

Using the potential (3.35) in Fermi's golden rule and integrating over the final states

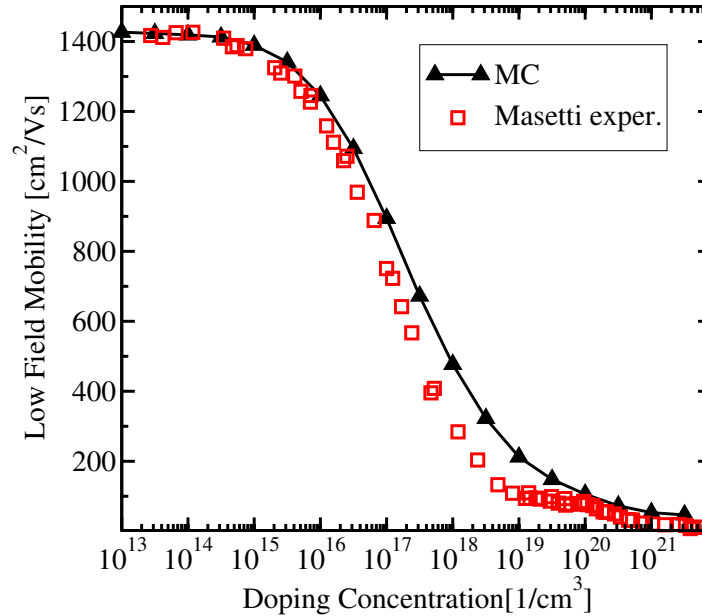


Figure 3.5: Electron low field mobility versus doping concentration for Si. Experimental data [Masetti83] are compared to Monte Carlo results. An ionized impurity model which includes a two-ion potential and dispersive screening is used for the Monte Carlo simulation.

the equivalent total scattering rate \tilde{S}_{BH} is found to be [Kosina97]

$$\tilde{S}_{\text{BH}} = C(k) \frac{1}{4k^2} \left(\ln(1+b) - \frac{b}{1+b} \right). \quad (3.51)$$

Figure 3.5 shows the low field electron mobility versus the doping concentration in Si. The Monte Carlo result is achieved by using a modified Brooks-Herring scattering model, which includes a two-ion potential and dispersive screening. The result shows fairly good agreement with experimental data [Masetti83]. Further improvements can be achieved by taking the second Born correction and plasmon scattering into account [Kosina98].

3.3.3 Impact Ionization

Impact ionization is modeled using a modified threshold expression [Cartier93]

$$S^{\text{II}} = \begin{cases} P_1 \left(\frac{\varepsilon}{1\text{eV}} - \frac{\varepsilon_{\text{th}}^1}{1\text{eV}} \right)^3 & : \varepsilon_{\text{th}}^1 < \varepsilon < \varepsilon_{\text{th}}^1 + \varepsilon_{\text{OS}} \\ P_2 \left(\frac{\varepsilon}{1\text{eV}} - \frac{\varepsilon_{\text{th}}^2}{1\text{eV}} \right)^2 & : \varepsilon_{\text{th}}^1 + \varepsilon_{\text{OS}} < \varepsilon \end{cases} \quad (3.52)$$

where S^{II} is the impact ionization scattering rate, $\varepsilon_{\text{th}}^1$ and $\varepsilon_{\text{th}}^2$ are threshold energies, and P_1 and P_2 are prefactors which determine the softness of the threshold. The value of the offset energy ε_{OS} is chosen to render the scattering function continuous.

The parameters are tuned to reproduce measured electron velocity field characteristics [Canali75] and impact ionization coefficients [Slotboom87][Overstraeten70] [Maes90] for relaxed Si: $\varepsilon_{\text{th}}^1 = \varepsilon_{\text{g}}$, $\varepsilon_{\text{th}}^2 = \varepsilon_{\text{g}} + 444 \text{ meV}$, $P_1 = 4.5 \cdot 10^{11} \text{ 1/s}$, $P_2 = 3.4 \cdot 10^{12} \text{ 1/s}$, and $\varepsilon_{\text{OS}} = 622 \text{ meV}$. For strained Si the threshold values are adjusted in accordance with the bandgap change. After an impact ionization scattering event is evaluated the overall final energy $\varepsilon - \varepsilon_{\text{g}}$ is randomly distributed between the hole and the primary and secondary electrons.

Fig 3.6 depicts the impact ionization coefficient of electrons in Si as a function of the inverse electric field. The simulation result agrees very well with various measured values from literature.

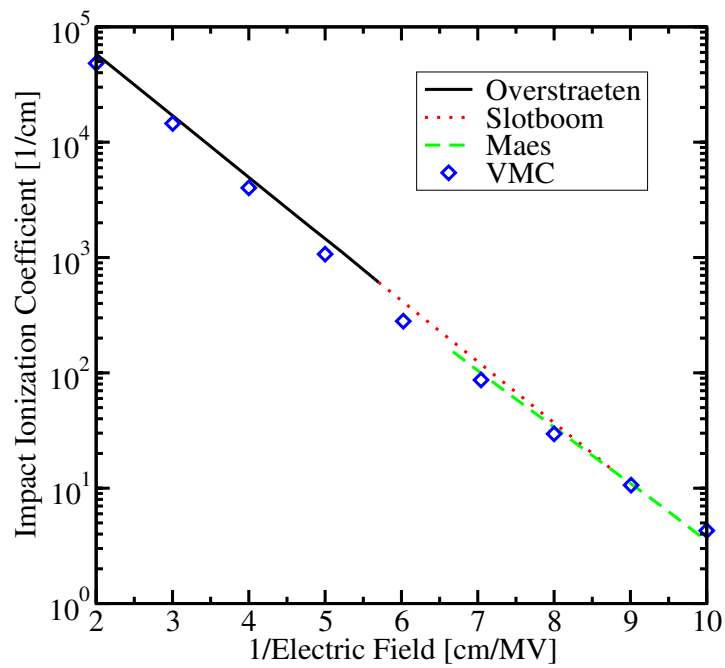


Figure 3.6: Impact ionization coefficient versus the inverse electric field. Monte Carlo result (VMC) is compared to measurements [Overstraeten70] [Slotboom87][Maes90].

Chapter 4

Monte Carlo Technique

4.1 Random Numbers: Direct and Indirect Method

Monte Carlo Methods require a large amount of uniformly distributed random numbers. In computer simulations usually a sufficient long sequence of pseudo random numbers is used, which makes the results reproducible and debugging of program code generally easier. The probability density $p(r)$ of a uniformly distributed random number r is

$$p(r) = \begin{cases} 1, & 0 < r < 1 \\ 0, & \text{otherwise} \end{cases} \quad (4.1)$$

The uniformly distributed pseudo random numbers are used to obtain random numbers x according to a given distribution function $F(x)$. The distribution function reads [Papoulis84]

$$F(x) = \int_{-\infty}^x p(x') dx' . \quad (4.2)$$

The distribution function satisfies

$$F(-\infty) = 0, \quad 0 \leq F(x) \leq 1, \quad \text{and} \quad F(\infty) = 1. \quad (4.3)$$

If the distribution function is simple enough so that its inverse F^{-1} can be found the direct method [Kalos86] [Jacoboni83] can be used to obtain a random number x from a uniformly distributed random number r by

$$x = F^{-1}(r) . \quad (4.4)$$

If the probability distribution is discrete – with P_j being the probability of the j th event – the integer number i can be calculated with a discrete formulation of the direct method

$$i : \sum_{j=1}^{i-1} P_j < r \leq \sum_{j=1}^i P_j, \quad (4.5)$$

With this procedure the i –th event of N possible events is chosen according to the discrete probabilities of the events. For those cases where the inverse distribution cannot be obtained the rejection method can be used.

This method consists of two steps. It involves the probability density $\tilde{p}(x)$ which is chosen so that it reproduces the original probability density $p(x)$ as close as possible but with the constraint that a closed form of the inverse distribution function can be found. In a first step a random number x_1 is generated with a probability density $\tilde{p}(x)$ with the condition

$$M\tilde{p}(x) \geq p(x), \quad (4.6)$$

where M is a positive constant. The closed form of the inverse distribution function allows to generate x_1 using the direct method from an uniformly distributed random number r_1 . In a second step it is determined if the random number x_1 is accepted by the condition

$$p(x_1) > r_2 M \tilde{p}(x_1). \quad (4.7)$$

Here, r_2 is another uniformly distributed random number. If (4.7) does not hold, x_1 is rejected and the whole procedure is repeated with two new random numbers r_1 and r_2 .

4.2 Piecewise Constant Gamma Scheme

During a Monte Carlo simulation the scattering rate depends in a complex way on the carrier state. Therefore, calculating the time t_{scat} of the next scattering event demands for high computing time. To speed up the calculation of t_{scat} the scattering rate can be rendered to a constant upper bound value, Γ , by introducing an artificial scattering process, the so called self-scattering [Jacoboni83] process. In the following a scheme using piecewise constant Γ -values is illustrated, which is particularly suitable for FBMC.

For the sake of a simplified notation the variables of a particle state are written as

$$\xi = (n, \mathbf{r}^T, \mathbf{k}^T)^T. \quad (4.8)$$

With (3.3) and (3.4) $\dot{\xi}$ is formulated as

$$\dot{\xi} = \left(n, \mathbf{v}_n^T(\mathbf{r}, \mathbf{k}), \mathbf{F}_n^T(\mathbf{r}, \mathbf{k}) \frac{1}{\hbar} \right)^T . \quad (4.9)$$

Furthermore, the integral over the phase space volume and the summation over the band index is shortened as

$$\int d\xi = \sum_n \int_{\Omega} \int_{\text{BZ}} d^3k d^3r . \quad (4.10)$$

With the above formulations and the definitions [Jungemann03]

$$\dot{\xi}^T \nabla_{\xi} = \mathbf{F}_n^T(\mathbf{r}, \mathbf{k}) \frac{1}{\hbar} \nabla_{\mathbf{k}} + \mathbf{v}_n^T(\mathbf{r}, \mathbf{k}) \nabla_{\mathbf{r}} , \quad (4.11)$$

$$S(\xi, \xi') = \frac{\Omega}{(2\pi)^3} S_{n,n'}(\mathbf{k}, \mathbf{k}')(\mathbf{r}) \delta(\mathbf{r} - \mathbf{r}') , \quad (4.12)$$

the BTE (3.11) for the probability density can be written as

$$\left\{ \frac{\partial}{\partial t} + \dot{\xi}^T \nabla_{\xi} + S(\xi) \right\} p(\xi, t) = \int S(\xi, \xi') p(\xi', t) d\xi' . \quad (4.13)$$

The probability density in the phase-space is related to the distribution function by

$$p(\xi) = p(\mathbf{r}, \mathbf{k}, t) = \frac{2}{N(2\pi)^3} f_n(\mathbf{r}, \mathbf{k}, t) . \quad (4.14)$$

Here, N denotes the total number of carriers in the carrier gas. With the introduction of the conditional probability density $p(\xi', t' | \xi, t)$, which gives the probability that a carrier in the state ξ at the time t is found in the state ξ' at time t' , the formal integration of the BTE gives for the probability density

$$p(\xi, t | \xi_0, t_0) = p_0(\xi, t | \xi_0, t_0) + \int_{t_0}^t \int \int p_0(\xi, t | \xi_1', t_1) S(\xi_1' | \xi_1) p(\xi_1, t_1 | \xi_0, t_0) d\xi_1' d\xi_1 dt_1 . \quad (4.15)$$

In (4.15) $p_0(\xi, t | \xi_0, t_0)$ is the conditional probability density that a particle with the initial state ξ_0 at the time t_0 is found in the state ξ at time t without being scattered

$$p_0(\xi, t | \xi_0, t_0) = \delta(\xi - \xi_{\text{Mot}}(t | \xi_0, t_0)) \exp \left(- \int_{t_0}^t S(\xi_{\text{Mot}}(\tau | \xi_0, t_0)) d\tau \right) . \quad (4.16)$$

Here, $\xi_{\text{Mot}}(t|\xi_0, t_0)$ is the solution of the equations of motion (3.3) and (3.4) for a carrier tracked from time t_0 to time t with the initial position ξ_0 in phase-space. The evaluation of (4.16) is simplified by adding a self-scattering process S_{Self} to the scattering integral, which has the transition rate [Jacoboni83]

$$S_{\text{Self}}(\xi', \xi) = (\Gamma - S(\xi))\delta(\xi' - \xi) , \quad (4.17)$$

This self-scattering does not change the carrier state and therefore leaves the solution of the BTE unchanged, but renders the total scattering rate to a constant Γ .

$$S_{\text{tot}} = \int S_{\text{Self}}(\xi'|\xi)d\xi' + S(\xi) = \Gamma . \quad (4.18)$$

Γ must be larger than the scattering rate for all possible states ξ . The probability that a scattering event occurs at time τ in an interval $d\tau$ after being propagated since time t_0 without scattering is

$$dp_{\text{scat}} = \tau \left(\int p_0(\xi, \tau|\xi_0, t_0)d\xi \right) d\tau \quad (4.19)$$

With the direct method the time t_{scat} is obtained by integration of (4.19), where r is a uniformly distributed random number

$$\int_0^r dp_{\text{scat}} = \int_{t_0}^{t_{\text{scat}}} \int \tau p_0(\xi, \tau|\xi_0, t_0)d\xi d\tau = 1 - \exp(-\tau(t_{\text{scat}} - t_0)) . \quad (4.20)$$

Solving (4.20) for t_{scat} yields

$$t_{\text{scat}} = t_0 - \frac{1}{\tau} \ln(1 - r) . \quad (4.21)$$

Evaluation of (4.21) allows a much more efficient calculation of the time of flight compared to solving the integral (4.16). As a tradeoff it introduces new artificial scattering events. Since Γ must be larger than the physical scattering rate $S(\xi)$ for all possible states ξ , and $S(\xi)$ usually varies over several orders of magnitude, a constant Γ leads to a dominating self scattering rate for some regions. To overcome this drawback the phase-space is partitioned into small regions Ω_i and for each region a local Γ_i is determined

$$\Gamma_i = \max_{\xi \in \Omega_i} [S(\xi)] . \quad (4.22)$$

Within FBMC it is convenient to choose the region Ω_i to be the volume of a mesh element of the phase space mesh. The duration of a collisionless flight is then [Jungemann03]

$$\Gamma_j(t_{\text{scat}} - t_j) = -\ln(1 - r) - \sum_{k=1}^j \Gamma_{k-1}(t_k - t_{k-1}) \quad \text{for } t_j \leq t_{\text{scat}} < t_{j+1} \quad (4.23)$$

where t_j is the time at which a particle passes from mesh element Ω_{j-1} to Ω_j . The sum on the right hand side of (4.23) is evaluated during the collisionless flight until t_{scat} is smaller than the time the carrier needs to reach the border of the next mesh element. The random number r remains unchanged during this procedure. After the element where the collisionless flight ends is determined, the new state

$$\xi = \xi_{\text{mot}}(t_{\text{scat}} | \xi_0, t_0) \quad (4.24)$$

is obtained by evaluating the equations of motion (3.3) and (3.4). Next one of the scattering processes (including self scattering) is selected by using the direct method

$$\sum_{l=1}^{i-1} S_l(\xi) < \Gamma_j r \leq \sum_{l=1}^i S_l(\xi) \quad (4.25)$$

where r is another uniformly distributed random number. If self scattering is selected the carrier state remains unchanged but particle statistics are updated and evaluation of equation (4.23) is started again with a new random number. If a physical scattering process is selected a position within the \mathbf{k} -space has to be determined for the scattered particle.

4.3 Self-Scattering Scheme for Ionized Impurity Scattering

Instead of evaluating the ionized impurity scattering rate with the complicated potential (3.48), a more efficient self-scattering scheme can be implemented in a Monte Carlo simulator. Within this scheme the Brooks-Herring rate multiplied by a factor M is evaluated. Using (3.35) and (3.48) M is chosen so that the following relation is fulfilled for any q in the interval $[0, 2k]$

$$M |V_{\text{BH}}(q)|^2 \geq |V_{\text{t}}(q)|^2 . \quad (4.26)$$

A scattering rate of Brooks-Herring type is obtained which is always larger than the scattering rate resulting from the potential (3.48)

$$M|S_{\text{BH}}(q)|^2 \geq |S_{\text{t}}(q)|^2 . \quad (4.27)$$

Here, S_{t} is the scattering rate, which is evaluated with the potential (3.48). Therefore a well defined probability P exists that a Coulomb scattering event is accepted [Kosina97]

$$P = \frac{\int_0^{2k} |V_{\text{t}}(q)|^2 q^3 dq}{M \int_0^{2k} |V_{\text{BH}}(q)|^2 q^3 dq} . \quad (4.28)$$

Instead of solving these integrals numerically a solution by means of Monte Carlo integration can be found the following way. First a random number $q_{\text{r}} \in [0, 2k]$ with the probability density $|V_{\text{BH}}(q)|^2 q^3$ is chosen. Then a second random number p_{r} is chosen, which is evenly distributed between $[0, M|V_{\text{BH}}(q_{\text{r}})|^2]$. If $p_{\text{r}} < |V_{\text{t}}(q_{\text{r}})|^2$, the scattering event is accepted, otherwise it is rejected and a self-scattering event is performed.

4.4 Selecting a k -vector after Scattering

In this section, the basic layout of a rejection algorithm to select the final state of a carrier after a scattering event is shown.

For scattering models with constant matrix elements the scattering rates are proportional to the DOS at the carrier's final energy ε_{f} (see Section 3.3). Selection of a state after scattering then relies mainly on the calculation of the contribution to the DOS of the mesh elements including the particle's final energy. This is achieved by using tetrahedral mesh elements and linear interpolation of the energy within the mesh elements. The contribution g_i to the DOS of the i -th tetrahedron is proportional to the intersection of the equi-energy surface $A_i(\varepsilon_{\text{f}})$ [Lehmann72][Jungemann03]

$$g_i = \frac{1}{(2\pi)^3 \hbar} \frac{A_i(\varepsilon_{\text{f}})}{|\mathbf{v}(\mathbf{k})|} . \quad (4.29)$$

The group velocity $\mathbf{v}(\mathbf{k})$ defined by equation (3.5) is constant within a tetrahedron if we consider a linear interpolation of the energy. The group velocity can be precalculated and stored in a table. The total DOS for a band n is given by

$$g_n(\varepsilon_f) = \frac{1}{(2\pi)^3} \int_{BZ} \delta(\varepsilon_f - \varepsilon_n(\mathbf{k})) d^3k = \frac{1}{(2\pi)^3 \hbar} \int_{A(\varepsilon_f)} \frac{1}{|\mathbf{v}(\mathbf{k})|} d^2k = \sum_i g_i. \quad (4.30)$$

It should be noted, that with linear energy interpolation an equi-energy surface within the Brillouin zone is continuous.

The most time consuming task while computing a scattering event is the selection of a final tetrahedron containing the final energy ε_f . Several tables are calculated once at start time of the simulation to speed up this selection process.

- **Table of Sorted Tetrahedrons:** the tetrahedral mesh elements representing the considered part of the first Brillouin zone are sorted with respect to their lowest energy values. Additionally, the numbering of the vertices of each tetrahedron is sorted with respect to increasing energy values.
- **Table of Upper Bounds for DOS:** the range from the lowest to the highest occurring energy within a band is divided into small energy intervals $\Delta\varepsilon_i$. For each energy interval the highest DOS within all tetrahedrons is stored to build a table of upper bounds $\overline{DOS}(\varepsilon)$.
- **Upper Bound for Energy Differences:** for each energy interval $\Delta\varepsilon_i$ the largest energy difference within the tetrahedrons which intersect a specific energy interval $\Delta\varepsilon_i$ is stored to build a list of upper bounds $\Delta\varepsilon_{\max}(\varepsilon)$.

After a scattering process is selected the final energy ε_f of the scattered particle is known and so the search for a final tetrahedron can be constricted to the tetrahedrons containing ε_f . Actually only tetrahedrons with a minimum energy in the range between ε_{\min} and ε_{\max} from the table of sorted tetrahedrons are considered in this search.

$$\begin{aligned} \varepsilon_{\min} &= (\varepsilon_f - \Delta\varepsilon_{\max}(\varepsilon_f)) \\ \varepsilon_{\max} &= \varepsilon_f \end{aligned} \quad (4.31)$$

The corresponding table indices N_{\min} and N_{\max} are calculated by a binary search. Then a tetrahedron T_i is chosen randomly from this interval. There is a small number of tetrahedrons in the considered interval which do not contain ε_f . These are sorted out within a first rejection step.

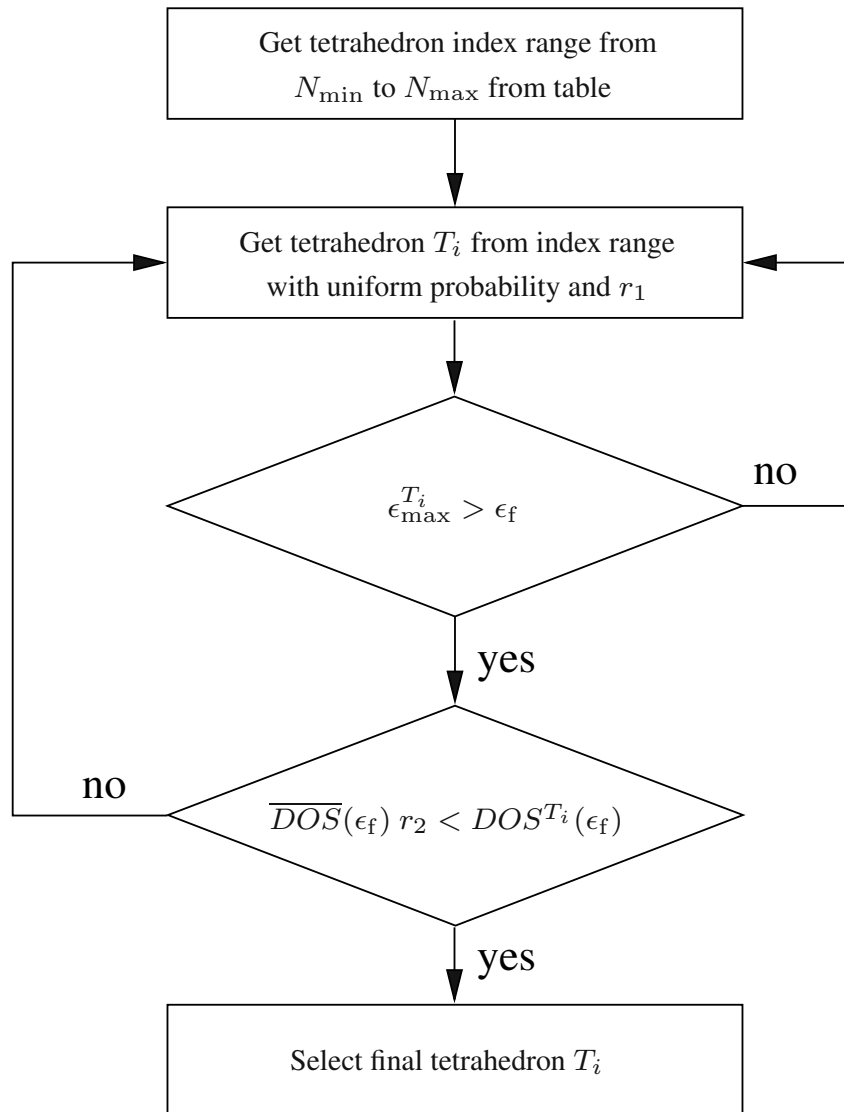


Figure 4.1: Rejection technique for the selection of the final state in \mathbf{k} -space. r_1 and r_2 are uniformly distributed random numbers between zero and one.

During a second rejection step the DOS within the tetrahedron has to be evaluated using equation (4.29). Figure 4.1 shows a flow-chart of the selection procedure with its two step rejection technique. Since the whole procedure is repeated until the second rejection step is passed, $g_i(\epsilon_f)$ has to be evaluated frequently during the simulation.

Finding the Final Wave Vector within the Chosen Tetrahedron

After selecting the final tetrahedron T_i , a final wave vector \mathbf{k}_f has to be chosen within this tetrahedron. Since equi-energy areas are planes and the group velocity is constant within a tetrahedron, this problem is reduced to the determination of a uniformly distributed random point on the equi-energy plane defined by ε_f .

The equi-energy plane has the shape of either a triangle or a quadrangle as depicted in Figure 4.9 and Figure 4.10, respectively. In the case of a quadrangle, it is split into two triangles and one triangle is randomly chosen according to the surface ratio. The final \mathbf{k} -vector is then determined with

$$\mathbf{k}_f = \mathbf{t}_1 + \lambda_1(\mathbf{t}_2 - \mathbf{t}_1) + \lambda_2(\mathbf{t}_3 - \mathbf{t}_1), \quad (4.32)$$

where \mathbf{t}_1 , \mathbf{t}_2 , and \mathbf{t}_3 are the \mathbf{k} -vectors to the vertices of the triangle. The random numbers λ_1 and λ_2 are derived as [Jungemann03]

$$\begin{aligned} \lambda_1 &= 1 - \sqrt{1 - r_1} \\ \lambda_2 &= r_2(1 - \lambda_1). \end{aligned} \quad (4.33)$$

Here, r_1 and r_2 uniformly distributed random numbers.

4.5 Meshing of the Brillouin Zone

Within this work we mesh the first octant of the first Brillouin zone to represent the band structure of relaxed and biaxially strained Si (see Section 2.6). Because an octant is a larger volume than the irreducible wedge, this approach obviously increases memory consumption. However, it simplifies the manipulations needed when particles reach a boundary [Karlwatz07].

The energy bands are calculated for the irreducible wedge using the empirical pseudopotential method [Ungersboeck07a][Rieger93] and then transformed by coordinate permutation to completely fill the first octant. Two approaches of mesh generation employing structured and unstructured tetrahedral meshes are explored for several simulation setups.

The structured mesh is based on an octree approach. The domain to be meshed is divided into cubes and afterwards the cubes are divided into six tetrahedrons. To mesh the $\{111\}$ surface of the Brillouin zone either one or five tetrahedrons have to be cut away from the six tetrahedrons forming one cube. The result is a structured tetrahedral mesh, whose surface is conform with the Brillouin zone boundary.

Figure 4.2(a) shows the k_x - k_y plane of the first octant of the Brillouin zone with the contour plot of the energy of the first conduction band. The main drawback of

the octree approach is the difficulty to implement a sufficiently flexible refinement strategy to accommodate different mesh densities. In [Fischer99] an octree algorithm is proposed which can deal with different mesh densities, but the refinement zone is limited to a cubical region and is therefore not very flexible.

A more flexible way of generating unstructured meshes is to use a mesh generator which can handle arbitrary point clouds with different point densities. In this particular work DELINK [Fleischmann99] was used to generate an initial, very coarse, unstructured mesh. For different energy bands this initial mesh was refined by the so-called *tetrahedral bisection* method. The basic idea of this method is to insert a new vertex on a particular edge, the *refinement edge*, of a tetrahedron, and to cut the tetrahedron into two pieces.

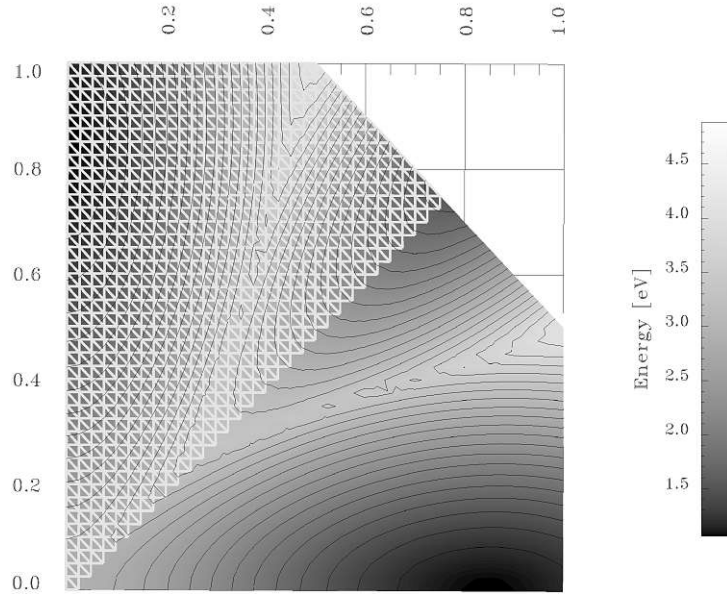
In literature one can find different improvements and specifications for this algorithm (see, for example [Arnold00]). One common problem is the detection of the refinement edge. In a mesh, tetrahedrons are not isolated and inserting a new vertex influences the whole refinement edge batch of the tetrahedron if the conformity of the mesh after the refinement step should be kept, which is normally the case. To guarantee good shaped elements, a recursive refinement mechanism was chosen. This approach produces very regular, almost isotropic elements.

To guarantee a conforming mesh during the refinement procedure, all tetrahedrons sharing a common refinement edge have to be divided. A tetrahedron is said to be *compatibly divisible* if its refinement edge is either the refinement edge of all other tetrahedrons sharing that edge or the edge is part of the boundary of the domain. If a tetrahedron is compatibly divisible, we divide the tetrahedron and all other tetrahedrons sharing the refinement edge simultaneously. If a tetrahedron is not compatibly divisible, we ignore it temporarily and divide a neighbor tetrahedron by the same process first. This leads to the atomic algorithm [Kossaczky94]. Figure 4.3 illustrates the recursive refinement process, where one new vertex is inserted.

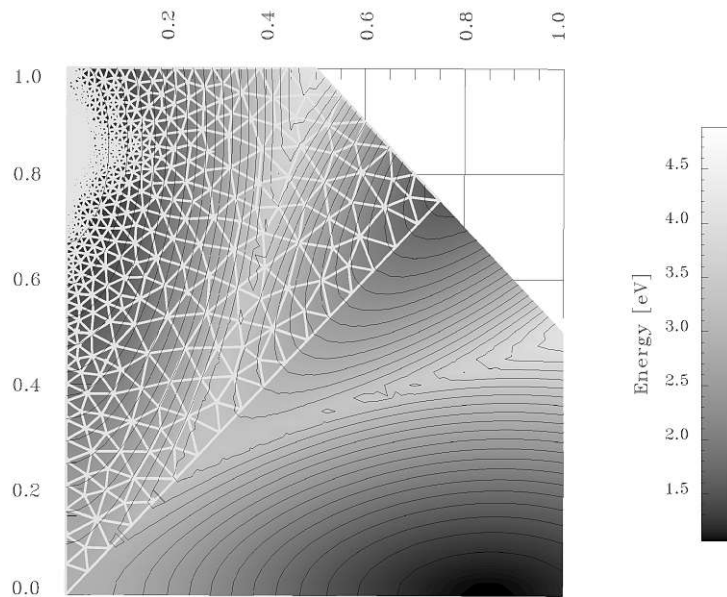
As an input to the mesher, regions of high point densities are pre-defined by the known positions of the band-minima in the Brillouin zone of Si. The dimension of this region is chosen such that the shifted band-minima of strained Si are taken into account and so the same mesh is usable with recalculated energy values for different amounts of strain. As every band has its unique position of the band-minima, the meshes are calculated for each band separately. For the valence bands only one mesh is used, which is refined around the Γ -point.

To demonstrate the benefits of mesh refinement four meshes are compared. A fine one and a coarse one of each the structured and the unstructured mesh type were generated. The number of points and tetrahedrons in the first conduction band of these meshes are shown in Table 4.5.

Figure 4.4 shows the mean electron energy as a function of the electric field for bulk Si for both structured and unstructured tetrahedral meshes. As the curves



(a) Structured Mesh



(b) Unstructured Mesh

Figure 4.2: k_x - k_y plane of the first conduction band in the first Brillouin zone with (a) structured and (b) unstructured meshes. Shown is only one octant.

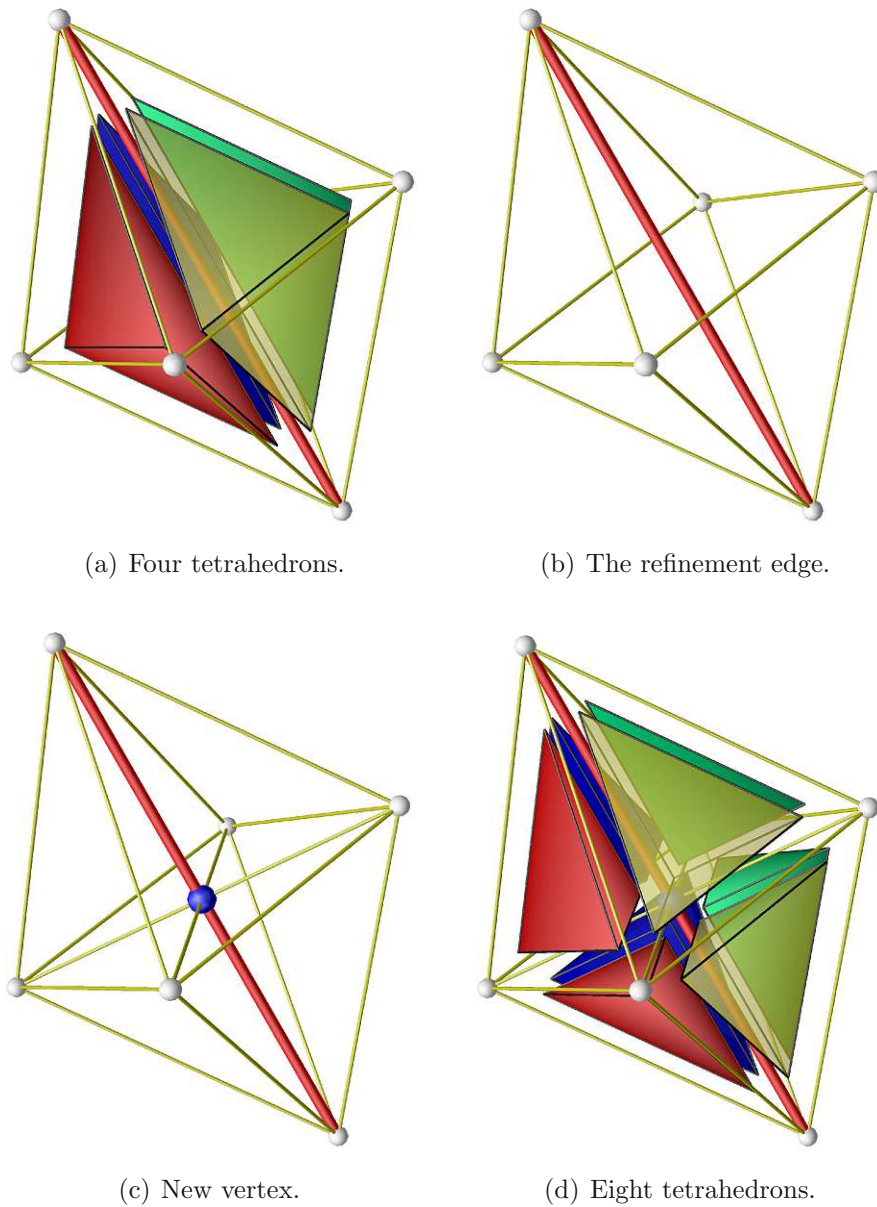


Figure 4.3: The recursive refinement procedure involving four tetrahedrons with one common refinement edge.

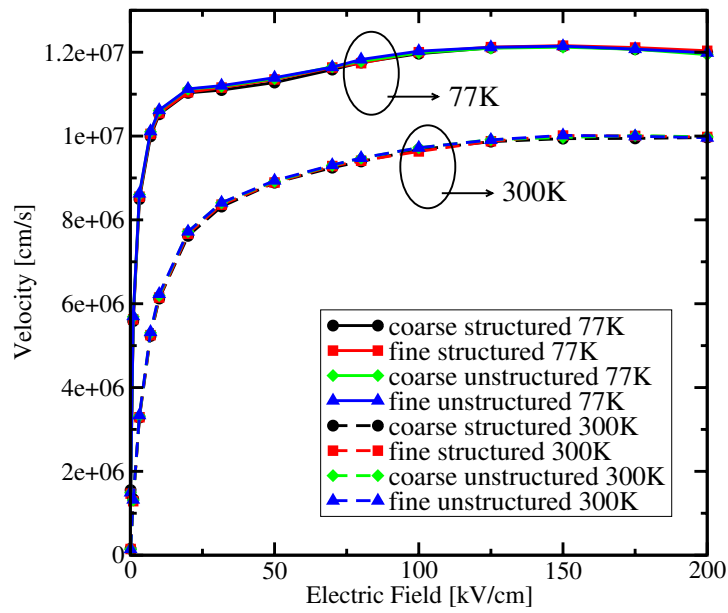


Figure 4.5: Electron velocity versus field along [100] direction for Si at 77K and 300K.

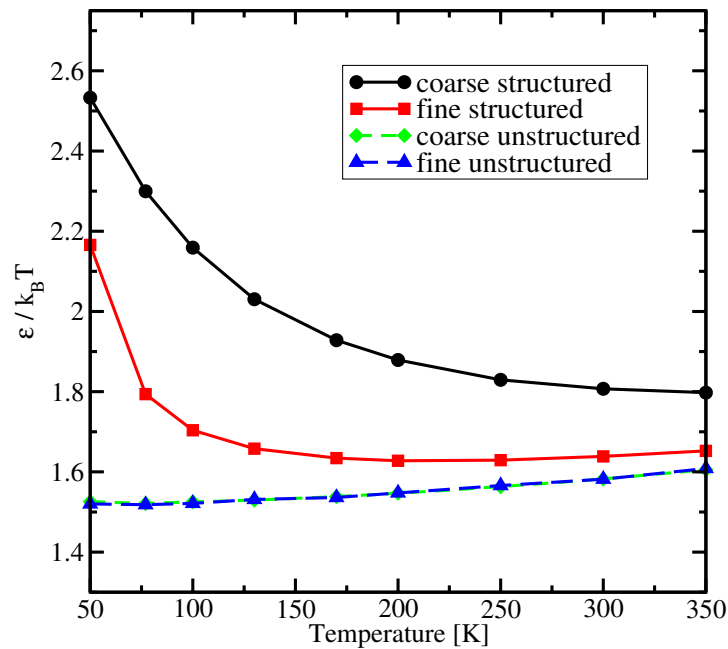


Figure 4.6: Normalized mean energy of electrons in Si at thermal equilibrium versus temperature.

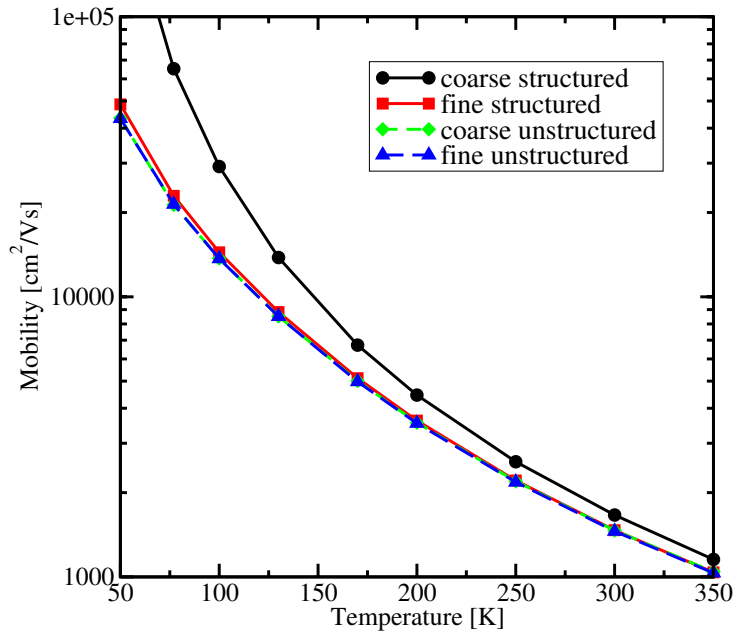


Figure 4.7: Low field mobility of electrons in Si versus temperature.

One can clearly observe that the CPU time consumption is high for the structured meshes. This is mainly due the higher build-up times. With the much higher amount of mesh elements for the fine structured mesh, it takes a long time to compute the precalculated tables shown in the last section. The computation time using the unstructured fine mesh is approximately in the same range as for the coarse structured mesh, but one has to keep in mind, that the structured mesh fails completely for the average kinetic energy at temperatures less than room temperature, where the coarse unstructured mesh still gives reasonable results (see Figure 4.6).

In conclusion, the tetrahedral meshes offer a very good potential for refinement techniques. Simulation results in the high field regime show similar accuracy for properly refined meshes as for structured octree-based meshes with more than ten

group	granularity	data structure points	tetrahedrons
structured	fine	278 166	1 536 134
	coarse	37 286	192 618
unstructured	fine	39 330	180 294
	coarse	20 346	88 938

Table 4.1: Parameter values of the meshes used for the first conduction band.

group	granularity	build-up time	200 kV/cm	0.1 kV/cm
structured	fine	12'19"	18'55"	14'49"
	coarse	2'26"	4'51"	3'12"
unstructured	fine	1'45"	4'57"	3'54"
	coarse	1'26"	4'11"	3'01"

Table 4.2: CPU time consumption for electron velocity simulations for a set of four different test meshes.

times the amount of tetrahedral elements. Simulations of electron mobility and mean electron energy in the low field regime show much better accuracy for refined meshes than octree-based meshes, particularly for simulations at low lattice temperatures.

4.6 Calculating the DOS

As shown in the last section the contribution of the tetrahedrons at a certain energy to the DOS has to be evaluated very frequently during a FBMC simulation. Therefore it is important to implement a CPU time efficient calculation algorithm.

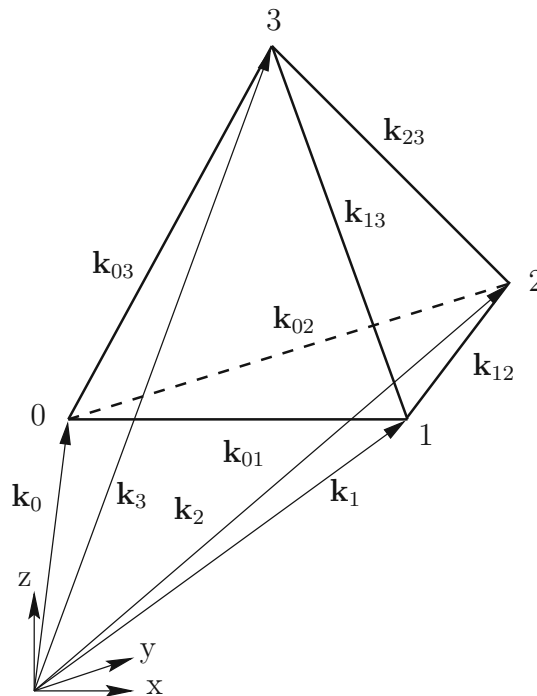


Figure 4.8: Tetrahedron with its defining location vectors

According to (4.30) the crucial step for the calculation of the DOS is to obtain the areas A_i of the intersecting equi-energy planes of all contributing tetrahedrons i .

In a first step the table of sorted tetrahedrons as defined in the last section is used to efficiently find tetrahedrons which intersect the considered energy surface. In the following both a conventional way to obtain this area and a more efficient approach based on the use of pre-calculated coefficients are presented. For the conventional calculation of the equi-energy plane the intersection points of the plane with the tetrahedron's edges are determined first.

With the vectors \mathbf{k}_0 to \mathbf{k}_3 of the tetrahedron's corners as depicted in Figure 4.8 the edges are derived as

$$\begin{aligned} \mathbf{k}_{01} &= \mathbf{k}_1 - \mathbf{k}_0, & \mathbf{k}_{02} &= \mathbf{k}_2 - \mathbf{k}_0, & \mathbf{k}_{03} &= \mathbf{k}_3 - \mathbf{k}_0, \\ \mathbf{k}_{12} &= \mathbf{k}_2 - \mathbf{k}_1, & \mathbf{k}_{13} &= \mathbf{k}_3 - \mathbf{k}_1, & \mathbf{k}_{23} &= \mathbf{k}_3 - \mathbf{k}_2. \end{aligned} \quad (4.34)$$

The edge equation in parameter form is then

$$\mathbf{s}_{ij} = \mathbf{k}_i \cdot (1 - t_{ij}) + \mathbf{k}_j t_{ij}, \quad t_{ij} \in [0, 1]. \quad (4.35)$$

The energy is interpolated linearly

$$\varepsilon_{ij} = \varepsilon_i \cdot (1 - t_{ij}) + \varepsilon_j t_{ij}. \quad (4.36)$$

For a given energy ε the parameter t_{ij} evaluates to

$$t_{ij} = \frac{\varepsilon - \varepsilon_i}{\varepsilon_j - \varepsilon_i}. \quad (4.37)$$

The \mathbf{s}_{ij} are the sought intersection points of the equi-energy plane with the edge vectors. With (3.5) and (4.37) equation (4.35) evaluates to

$$\mathbf{s}_{ij}(\varepsilon) = \mathbf{k}_i + \frac{\varepsilon - \varepsilon_i}{\hbar \mathbf{v}^T \cdot (\mathbf{k}_j - \mathbf{k}_i)} (\mathbf{k}_j - \mathbf{k}_i), \quad i, j = 0, 1, 2, 3, \quad i \neq j. \quad (4.38)$$

Expression (4.38) is symmetric, $\mathbf{s}_{ij} = \mathbf{s}_{ji}$. The intersection plane has either the shape of a triangle or a rectangle. If the intersection area consists of three intersection points forming a triangle A^T , its area is calculated by

$$A^T = \frac{1}{2} |(\mathbf{s}_{ij} - \mathbf{s}_{il}) \times (\mathbf{s}_{ik} - \mathbf{s}_{il})|. \quad (4.39)$$

In the case that the intersection is a quadrangle, it is split into two triangles the areas of which can be calculated as in (4.39).

Calculation of the area coefficients

To save computation time the calculation of intersection planes can be optimized by introducing area coefficients [Jungemann03], which are calculated in a pre-processing step and stored for each tetrahedron. The tetrahedron's vertices \mathbf{k}_0 , \mathbf{k}_1 , \mathbf{k}_2 , and \mathbf{k}_3 carry the energies ε_0 , ε_1 , ε_2 , and ε_3 . The energy ε changes linearly along the edges and is proportional to the parameter t (4.37). Therefore for the case of a triangular shaped slice as shown in Figure 4.9 we obtain for the area A^T

$$A^T = c_1 t^2 = c_2 (\varepsilon - \varepsilon_0)^2. \quad (4.40)$$

For energies ε in the range between ε_0 and ε_1 the intersection is given by the triangle $\{\mathbf{s}_{01}, \mathbf{s}_{02}, \mathbf{s}_{03}\}$ with the area

$$\begin{aligned} A^T(\varepsilon) &= \frac{1}{2} \left| \left(\mathbf{s}_{02}(\varepsilon) - \mathbf{s}_{01}(\varepsilon) \right) \times \left(\mathbf{s}_{03}(\varepsilon) - \mathbf{s}_{01}(\varepsilon) \right) \right| \\ &= \alpha_1 (\varepsilon - \varepsilon_0)^2, \end{aligned} \quad (4.41)$$

where α_1 is the first area coefficient. In the case of energies between ε_2 and ε_3 the intersection is also a triangle specified by $\{\mathbf{s}_{30}, \mathbf{s}_{31}, \mathbf{s}_{32}\}$. Similar to the first case we can obtain the intersection area with another area coefficient α_3 .

$$\begin{aligned} A(\varepsilon) &= \frac{1}{2} \left| \left(\mathbf{s}_{32}(\varepsilon) - \mathbf{s}_{30}(\varepsilon) \right) \times \left(\mathbf{s}_{31}(\varepsilon) - \mathbf{s}_{30}(\varepsilon) \right) \right| \\ &= \alpha_3 (\varepsilon - \varepsilon_3)^2. \end{aligned} \quad (4.42)$$

For energies between ε_1 and ε_2 the intersection has the shape of a quadrangle as depicted in 4.10. Its area $A^Q(\varepsilon)$ is obtained by subtracting the area of the inner

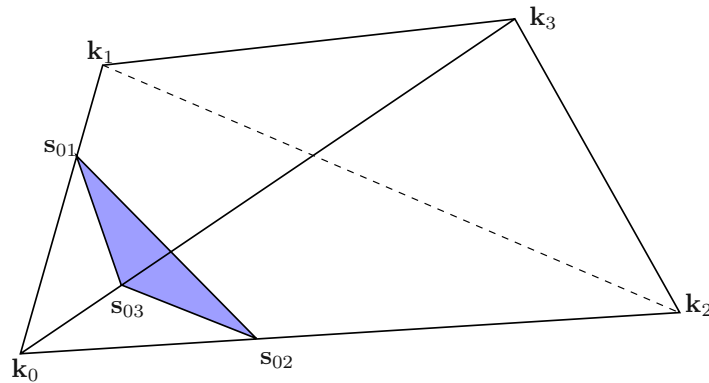


Figure 4.9: Triangular shaped equi-energy slice of a tetrahedron

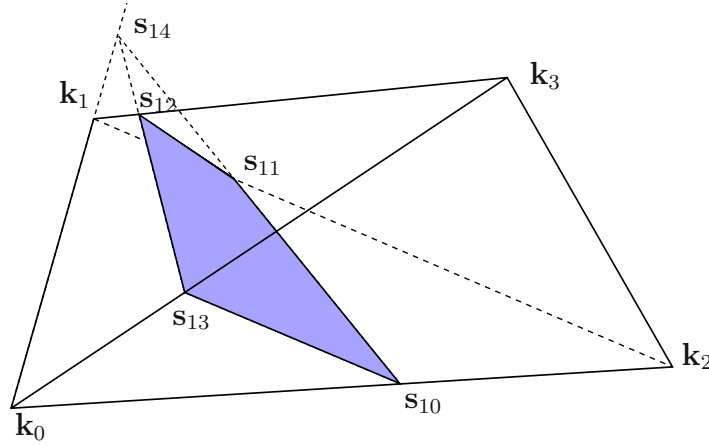


Figure 4.10: Quadrangular shaped equi-energy slice of a tetrahedron

triangle $\{\mathbf{s}_{11}, \mathbf{s}_{12}, \mathbf{s}_{14}\}$ from the area of the surrounding triangle $\{\mathbf{s}_{10}, \mathbf{s}_{13}, \mathbf{s}_{14}\}$. The inner triangle is parameterized by the introduction of another area coefficient α_2

$$\begin{aligned} A^Q(\varepsilon) &= \alpha_1(\varepsilon - \varepsilon_0)^2 - \frac{1}{2} \left| (\mathbf{s}_{11}(\varepsilon) - \mathbf{s}_{14}(\varepsilon)) \times (\mathbf{s}_{13}(\varepsilon) - \mathbf{s}_{14}(\varepsilon)) \right| \\ &= \alpha_1(\varepsilon - \varepsilon_0)^2 - \alpha_2(\varepsilon - \varepsilon_1)^2. \end{aligned} \quad (4.43)$$

The area coefficients α_1 , α_2 and α_3 derive as

$$\alpha_1 = \frac{A(\varepsilon_u)(\varepsilon_v - \varepsilon_1)^2 - A(\varepsilon_v)(\varepsilon_u - \varepsilon_1)^2}{(\varepsilon_u - \varepsilon_0)^2(\varepsilon_v - \varepsilon_1)^2 - (\varepsilon_v - \varepsilon_0)^2(\varepsilon_u - \varepsilon_1)^2}, \quad (4.44)$$

$$\alpha_2 = \frac{A(\varepsilon_u)(\varepsilon_v - \varepsilon_0)^2 - A(\varepsilon_v)(\varepsilon_u - \varepsilon_0)^2}{(\varepsilon_v - \varepsilon_0)^2(\varepsilon_u - \varepsilon_0)^2 - (\varepsilon_u - \varepsilon_0)^2(\varepsilon_v - \varepsilon_0)^2}, \quad (4.45)$$

and

$$\alpha_3 = \frac{A(\varepsilon_w)}{(\varepsilon_w - \varepsilon_3)}. \quad (4.46)$$

Here, $\varepsilon_u = (\varepsilon_2 + 2\varepsilon_1)/3$, $\varepsilon_v = (2\varepsilon_2 + \varepsilon_1)/3$, and $\varepsilon_w = (\varepsilon_3 + \varepsilon_2)/2$.

For the special case $\varepsilon_0 = \varepsilon_1$, an area calculation with equation (4.44) fails because both triangle areas become infinite. In this case another parameterization with the parameters δ and ϵ can be used, which is derived in the following. First the quadrangle shaped intersection area is split into two triangles with areas A_1^T and A_2^T

$$A_1^T = \frac{1}{2} |(\mathbf{s}_{11} - \mathbf{s}_{10}) \times (\mathbf{s}_{13} - \mathbf{s}_{10})|, \quad A_2^T = \frac{1}{2} |(\mathbf{s}_{11} - \mathbf{s}_{12}) \times (\mathbf{s}_{13} - \mathbf{s}_{12})|. \quad (4.47)$$

The terms on the right hand sides of (4.47) are given by

$$\mathbf{s}_{11} - \mathbf{s}_{10} = \frac{(\mathbf{k}_2 - \mathbf{k}_1)(\varepsilon - \varepsilon_0)}{\varepsilon_2 - \varepsilon_0} + \mathbf{k}_1 - \frac{(\mathbf{k}_2 - \mathbf{k}_0)(\varepsilon - \varepsilon_0)}{\varepsilon_2 - \varepsilon_0} - \mathbf{k}_0 = \quad (4.48)$$

$$= (\mathbf{k}_0 - \mathbf{k}_1) \frac{\varepsilon - \varepsilon_0}{\varepsilon_2 - \varepsilon_0} - (\mathbf{k}_0 - \mathbf{k}_1) \frac{\varepsilon - \varepsilon_0}{\varepsilon_2 - \varepsilon_0} = \mathbf{k}_a (\varepsilon - \varepsilon_0) - \mathbf{k}_a (\varepsilon_2 - \varepsilon_0) ,$$

$$\mathbf{s}_{13} - \mathbf{s}_{10} = \frac{(\mathbf{k}_3 - \mathbf{k}_0)(\varepsilon - \varepsilon_0)}{\varepsilon_3 - \varepsilon_0} + \mathbf{k}_0 - \frac{(\mathbf{k}_2 - \mathbf{k}_0)(\varepsilon - \varepsilon_0)}{\varepsilon_2 - \varepsilon_0} - \mathbf{k}_0 = \quad (4.49)$$

$$= \left(\frac{\mathbf{k}_{13} - \mathbf{k}_{10}}{\varepsilon_3 - \varepsilon_0} - \frac{\mathbf{k}_2 - \mathbf{k}_0}{\varepsilon_2 - \varepsilon_0} \right) (\varepsilon - \varepsilon_0) = \mathbf{k}_b (\varepsilon - \varepsilon_0) ,$$

$$\mathbf{s}_{11} - \mathbf{s}_{12} = \frac{(\mathbf{k}_2 - \mathbf{k}_1)(\varepsilon - \varepsilon_0)}{\varepsilon_2 - \varepsilon_0} + \mathbf{k}_1 - \frac{(\mathbf{k}_3 - \mathbf{k}_1)(\varepsilon - \varepsilon_0)}{\varepsilon_3 - \varepsilon_0} - \mathbf{k}_1 = \quad (4.50)$$

$$= \left(\frac{\mathbf{k}_2 - \mathbf{k}_1}{\varepsilon_2 - \varepsilon_0} - \frac{\mathbf{k}_3 - \mathbf{k}_1}{\varepsilon_3 - \varepsilon_0} \right) (\varepsilon - \varepsilon_0) = \mathbf{k}_c (\varepsilon - \varepsilon_0) ,$$

and

$$\mathbf{s}_3 - \mathbf{s}_2 = \frac{(\mathbf{k}_3 - \mathbf{k}_0)(\varepsilon - \varepsilon_0)}{\varepsilon_3 - \varepsilon_0} + \mathbf{k}_0 - \frac{(\mathbf{k}_3 - \mathbf{k}_1)(\varepsilon - \varepsilon_0)}{\varepsilon_3 - \varepsilon_0} - \mathbf{k}_1 = \quad (4.51)$$

$$= (\mathbf{k}_1 - \mathbf{k}_0) \frac{\varepsilon - \varepsilon_0}{\varepsilon_3 - \varepsilon_0} - (\mathbf{k}_1 - \mathbf{k}_0) \frac{\varepsilon_3 - \varepsilon_0}{\varepsilon_3 - \varepsilon_0} = \mathbf{k}_d (\varepsilon - \varepsilon_0) - \mathbf{k}_d (\varepsilon_3 - \varepsilon_0) .$$

Now, the area $A^Q = A_0^T + A_1^T$ of the quadrangle can be written in a parameterized formulation

$$A_Q = \frac{1}{2} \alpha_4 (\varepsilon - \varepsilon_0) - \frac{1}{2} \alpha_5 (\varepsilon - \varepsilon_0)^2 , \quad (4.52)$$

where α_4 and α_5 are pre-calculated parameters for the given tetrahedron:

$$\alpha_4 = |\mathbf{k}_a \times \mathbf{k}_b| + |\mathbf{k}_c \times \mathbf{k}_d| \quad (4.53)$$

$$\alpha_5 = (\varepsilon_2 - \varepsilon_0) |\mathbf{k}_a \times \mathbf{k}_b| + (\varepsilon_3 - \varepsilon_0) |\mathbf{k}_c \times \mathbf{k}_d| . \quad (4.54)$$

Since the regular tetrahedron and the tetrahedron where ε_0 equals ε_1 are completely alternative appearances, the area coefficient α_2 is not needed in the latter case. Therefore the area calculation is in any case completely parameterized with four pre-calculated area coefficients per tetrahedron.

4.7 Precalculated Values related to the Mesh Structure

As shown in Section 4.5 it is convenient to use tetrahedral meshes for discretization of the Brillouin zone. It has also been shown that frequently used values like the area coefficients can be precalculated to improve performance during simulation. These values are stored related to the tetrahedral mesh elements, where they are either connected to the vertices, the surfaces or the volume.

The numbering of the vertices of each tetrahedron is sorted after increasing energies as explained in Section 4.4. The energies and positions of the vertices are stored in a table.

There are also several precalculated values which are connected to the tetrahedron volumes: the energy gradient, which is used to calculate the group velocity, the area-coefficients α_1 to α_5 (see Section 4.6), and the upper bounds for the scattering rates for different types of scattering mechanisms.

For each of the four surfaces of a tetrahedron the type of the surface and a pointer to the neighbor tetrahedron are stored. Figure 4.11 shows the definition of the surface types. This value is used for efficient detection of the surface that would be crossed when a carrier has reached a border of the meshed part of the Brillouin zone. If the surface of the tetrahedron is inside of the meshed domain then the value of the surface type is defined as zero.

The pointer to the neighbors fulfills a special purpose if a tetrahedron's surface is part of the boundary of the meshed domain. In this case the pointer is set to the tetrahedron to which the carrier's position is mapped back when leaving the domain. This mapping procedure requires tetrahedrons with a surface mesh structure where the initial surface elements are congruent with the final elements. Because the mesh is built by the permutation of irreducible wedges as explained in section Section 2.6.5, this feature is guaranteed for the surfaces one to six. For surface seven the initial mesh must provide an additional symmetry [Jungemann03] as shown in Figure 4.12.

4.8 Selfconsistent Monte Carlo Scheme

The Boltzmann equation can be solved either with a given electric field or with a selfconsistent field using an iteration scheme as shown in Figure 4.13. After each time step Δt the carrier concentration is evaluated and the Poisson equation is solved

$$\nabla_{\mathbf{r}}^T [\epsilon(\mathbf{r}) \nabla_{\mathbf{r}} \psi(\mathbf{r}, t)] = -\rho(\mathbf{r}, t) \quad (4.55)$$

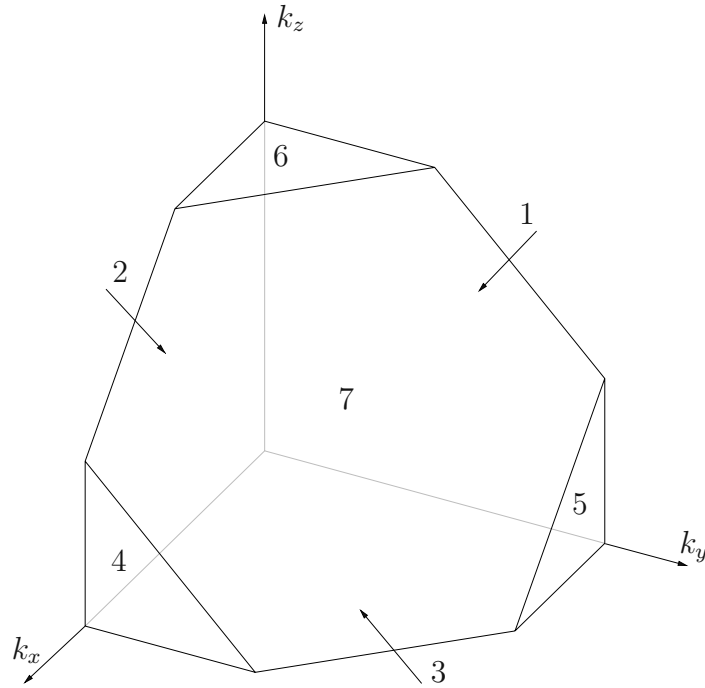


Figure 4.11: Surface types for one octant of the Brillouin zone in \mathbf{k} -space [Wagner04].

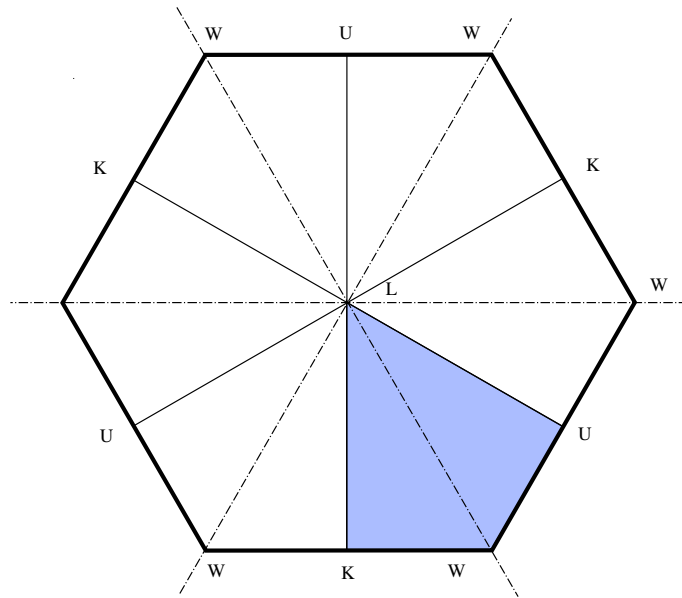


Figure 4.12: Symmetry properties of the surface 7. Solid lines are boundaries of irreducible wedges, with one wedge indicated in blue. Dashed-dotted lines indicate the additional symmetry needed for the mapping procedure.

for the electrostatic potential ψ which in turn gives a new field for the next iteration step. In (4.55) ϵ denotes the dielectric constant and ρ is the space charge density

$$\rho(\mathbf{r}, t) = e(p(\mathbf{r}, t) - n(\mathbf{r}, t) + N_D^+ - N_A^-). \quad (4.56)$$

Here, n denotes the electron concentration, p is the hole concentration, N_D^+ and N_A^- are the concentrations of the ionized donors and acceptors, respectively.

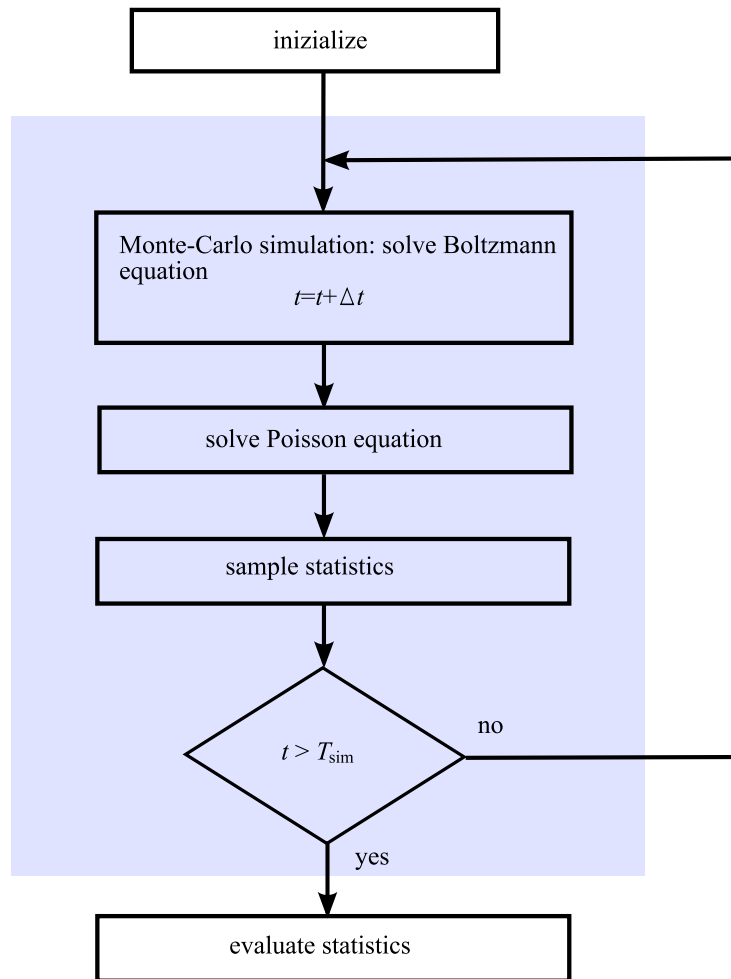


Figure 4.13: Flowchart of a selfconsistent Monte Carlo device simulation for a given total simulation time T_{sim} .

Chapter 5

Results

In this chapter the origin of the electron mobility gain in strained Si is explored by the analysis of the band structure obtained by EPM calculations. The same approach is used to explore the mobility gain for holes in strained Ge. Further, results from FBMC simulations are discussed for electrons in strained Si and for holes in strained Ge.

5.1 The Conduction Band Structure of Strained Si

5.1.1 Valley splitting

Usage of strained Si for performance enhancement of CMOS devices started with Si layers epitaxially grown on relaxed SiGe substrates [Welser92] [Welser94]. The thin Si layer takes the larger lattice constant of the SiGe substrate and therefore gets biaxially tensile strained. The usual configuration is a (001) oriented substrate, where the Δ_6 -valleys of the Si layer split into four equivalent valleys in the (001) plane which are shifted up in energy, and two equivalent valleys perpendicular to this plane which are shifted down in energy. The valley splitting suppresses intervalley scattering and therefore increases the mobility. The valley splitting also leads to a higher electron population in the lower valleys. Since the lower valleys exhibit lower effective masses, this redistribution mainly contributes to the mobility gain. With increasing strain the lower valleys are fully populated and the intervalley scattering to higher valleys is completely suppressed. From this point on the low field mobility does not benefit from further increasing the strain and mobility saturates. Uniaxial strain along [110] or [120] also induces valley splitting, but not as strong as biaxial

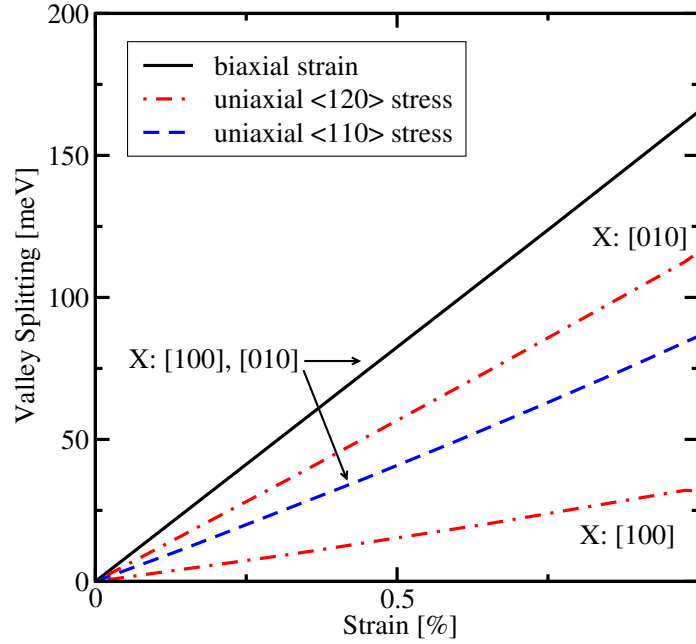


Figure 5.1: Energies of the [100] and the [010] valleys relative to the [001] valley for biaxial tensile strain and uniaxial [110] and [120] tensile strain. The abscissa shows the biaxial strain or the strain component in the stressed direction.

strain does. Figure 5.1 shows a comparison of the strain induced valley splitting as a result of EPM calculation for biaxial strain and uniaxial stress along [110] and [120] directions. It can be observed that biaxial tension is more effective in splitting the conduction band valleys than uniaxial tension.

5.1.2 Effective mass change

Experiments [Irie04][Uchida04] have shown that in the presence of shear strain the electron mobility enhancement in strained Si cannot solely be attributed to the energy splitting of the valleys. A recent study has shown that a stress along the [110] direction leads to a change of the effective masses [Uchida05][Ungersboeck07c]. The in-plane effective mass is rendered anisotropic and can be described by a component $m_{t,\parallel}$ parallel to the stress direction and one component $m_{t,\perp}$ normal to stress direction [Ungersboeck07b].

The in-plane effective masses of the lowest valley were extracted from EPM calculations. Figure 5.2 shows that uniaxial tensile stress along [110] yields the most pronounced Δm_t . This explains the pronounced anisotropy of the mobility in the transport plane as discussed in Section 5.2. The change Δm_t is negligible for biaxial tensile strain.

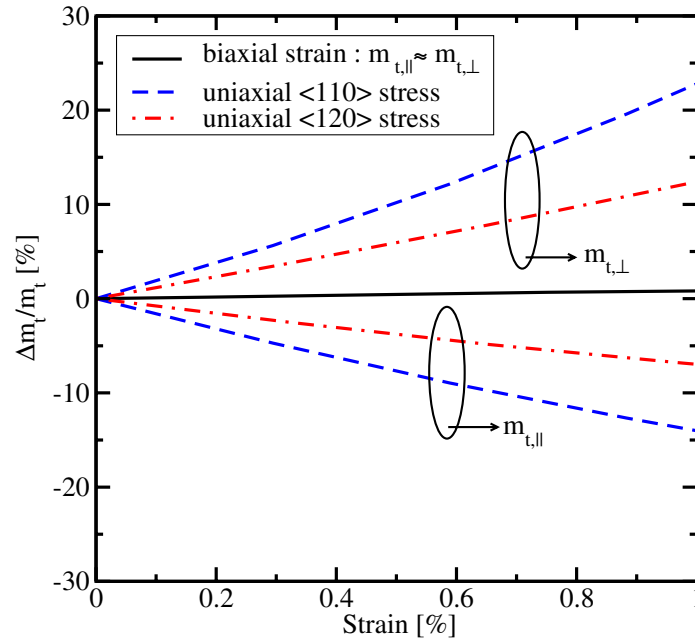


Figure 5.2: In-plane masses of the lowest valley for biaxial tensile strain and uniaxial [110] and [120] tensile strain.

This result points out another advantage of uniaxially stressed Si over biaxially strained Si. For high uniaxial stress levels in [110] direction the mobility enhancement originates mostly from the reduced conductivity mass, which is almost linearly reduced with increasing stress. Therefore no saturation for the mobility enhancement occurs within the technological relevant range of strain levels.

5.2 Low Field Electron Mobility of Strained Si

Figure 5.3 depicts the in-plane low field mobility in the strained Si layer versus the Ge mole fraction of the $\text{Si}_x\text{Ge}_{1-x}$ substrate. This result is obtained by FBMC simulation. Since the lattice constant of SiGe is larger than that of Si the resulting strain is tensile. For a mole fraction $x = 0.4$ the low field electron mobility is enhanced by a factor of 1.68 to $2410 \text{ cm}^2/\text{Vs}$. The mobility enhancement saturates for Ge mole fractions above 0.2.

Figure 5.4 depicts the in-plane electron mobility at low electric field for uniaxial tensile stress. Due to the effective mass change a strong anisotropy can be observed with the most pronounced mobility enhancement in stress direction.

A stress of 1.5GPa enhances the low field mobility by a factor of 1.63 to $2330 \text{ cm}^2/\text{Vs}$. Note that compressive stress instead of tensile stress could also be used for

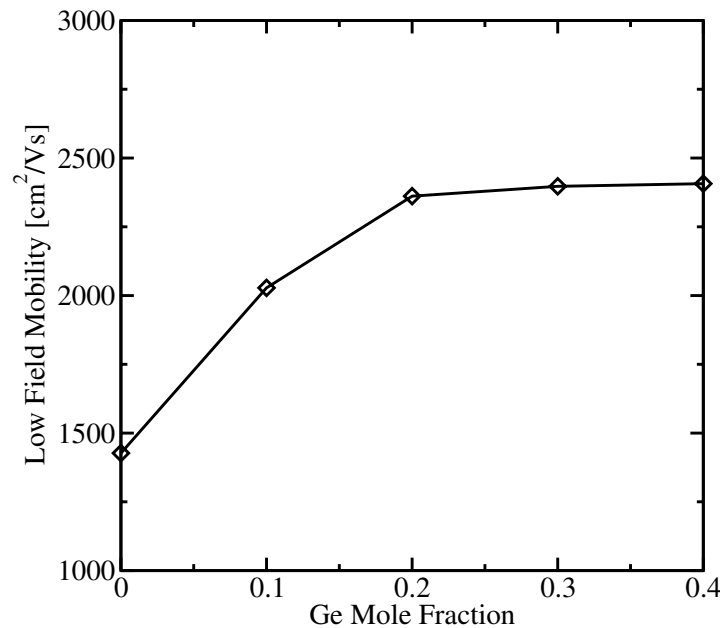


Figure 5.3: In-plane low field mobility of electrons in biaxially strained Si grown on a relaxed $\text{Si}_x\text{Ge}_{1-x}$ substrate.

electron mobility enhancement. The most pronounced enhancement is then achieved perpendicular to the applied stress in $[\bar{1}10]$ direction, otherwise the result looks similar as in Figure 5.4.

Figure 5.5 shows the electron mobility in a $(1\bar{1}0)$ plane at low electric field for uniaxial tensile stress in $[110]$ direction. In this setup a small low field mobility enhancement along the direction of stress can be achieved for low stress and a degradation for higher stress levels. In $[110]$ direction one can observe a strong mobility degradation for any stress level.

Recent achievements in strain engineering focus on combining different stress configurations to maximize the mobility gain. A promising approach is to apply tensile stress along $[110]$ and compressive stress along $[1\bar{1}0]$ to maximize shear strain and combine that with uniaxial compressive stress along $[001]$ [Ungersboeck07a]. The shear strain considerably lowers the mass in the $[110]$ direction whereas the $[001]$ uniaxial strain component introduces enhanced mobility due to the valley spitting effect. Figure 5.6 shows the mobility enhancement along $[110]$ for this stress setup for several stress level combinations.

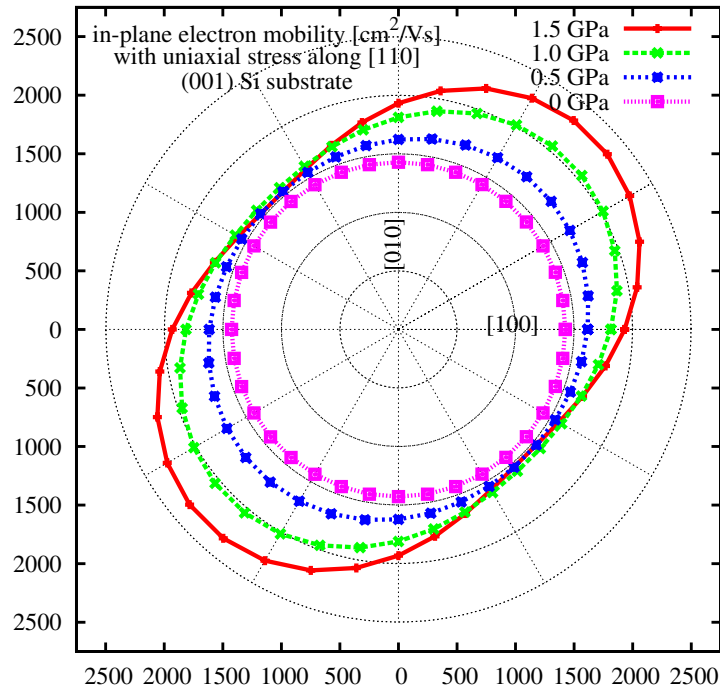


Figure 5.4: Low field electron mobility in the (001) plane in bulk Si for uniaxial [110] tensile stress.

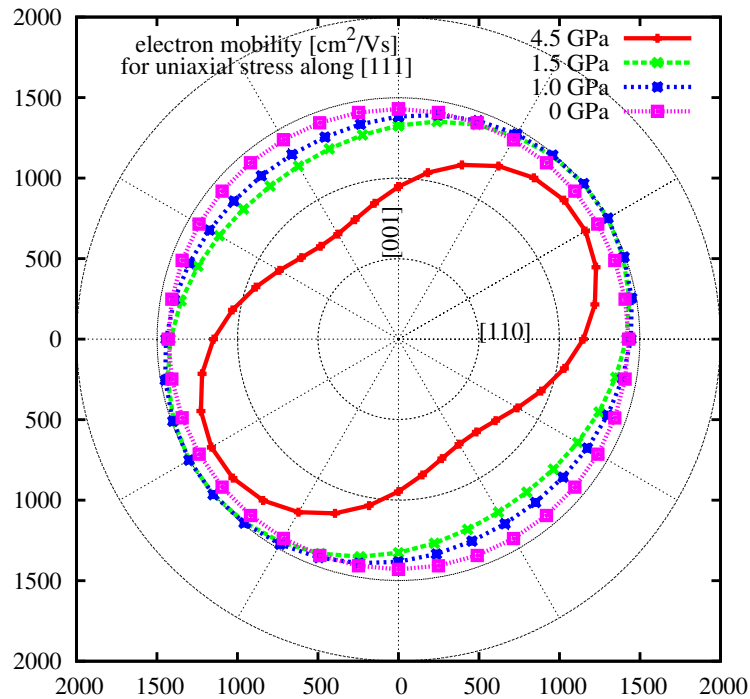


Figure 5.5: Low field electron mobility in the $(1\bar{1}0)$ plane of bulk Si for uniaxial [111] tensile stress.

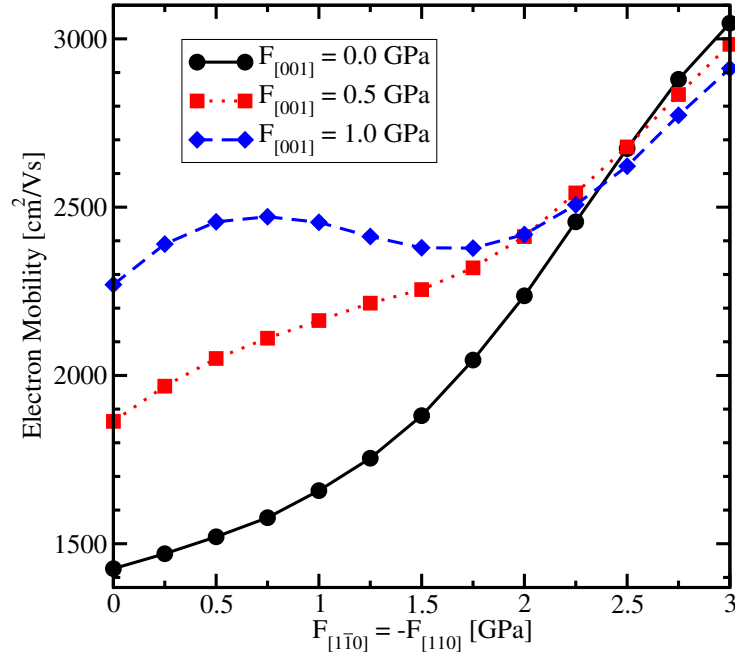


Figure 5.6: Low field electron bulk mobility of Si along $[110]$ for a combination of tensile stress $F_{[110]}$ along $[110]$, compressive stress $F_{[1\bar{1}0]}$ along $[\bar{1}\bar{1}0]$ and compressive stress $F_{[001]}$ along $[001]$.

5.3 High Field Electron Mobility of Strained Si

In the following the effect of strain on the high field mobility of Si is discussed.

Figure 5.7 depicts the electron velocity as a function of the electric field in biaxially strained Si grown on a $\text{Si}_x\text{Ge}_{1-x}$ substrate for various Ge contents. The curves show large velocity enhancement at medium fields but approach for high fields the saturation velocity of relaxed Si. A saturation of the enhancement can be observed for higher stress levels.

Figure 5.8 presents the velocity field characteristics for uniaxial tensile stress in $[110]$ direction and field in $[110]$ and the orthogonal $[\bar{1}\bar{1}0]$ direction. As applied stress is rising, the curves for field in $[110]$ direction show a steeper slope in the low field regime and exhibit a higher saturation velocity.

In contrast to the biaxial stress case the velocity enhancement exhibits no saturation for the shown stress levels, which once again can be explained by the shear strain component for stress in $[110]$ direction and the related effective mass change. Transport in the orthogonal $[\bar{1}\bar{1}0]$ direction shows a degradation of velocity.

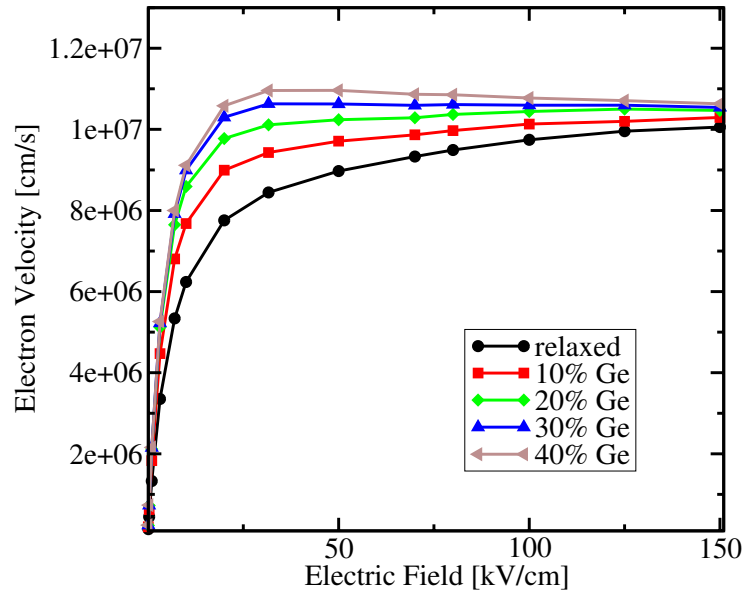


Figure 5.7: Electron velocity as a function of the electric field for field in $[100]$ direction for biaxially strained Si grown on a $\text{Si}_x\text{Ge}_{1-x}$ substrate.

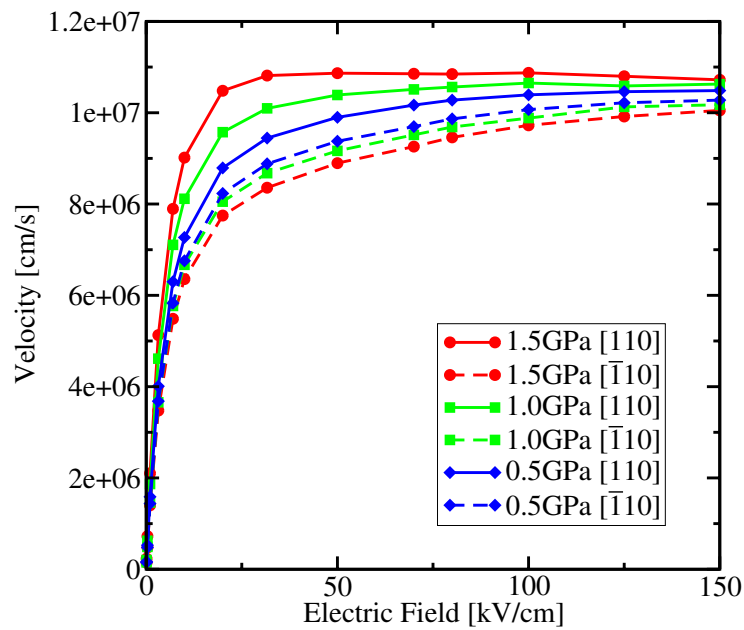


Figure 5.8: Electron velocity as a function of the electric field in $[110]$. Shown are curves for uniaxial tensile stress in $[110]$ and $[\bar{1}10]$ direction.

5.4 The Valence Band Structure of Strained Ge

The behavior of hole transport mainly depends on the features of two highly anisotropic bands: the heavy hole (HH) band and the light hole (LH) band. Even in the case of a low applied field both of these bands are important because their minima (in the hole picture) are degenerate at the Γ -point and therefore both contribute to the density of states. For hot holes also the split-off (SO) band has to be considered. Whereas the valence band structure for Si under strain is already explored by means of EPM calculation in literature [Wang06], the following sections focus on the less explored properties of the valence band structure of strained Ge.

5.4.1 Band splitting

Strain lifts the degeneracy of the HH and LH bands and also shifts the SO band. Depending on the type of strain the HH band can be above or below the LH band. Figure 5.9(a) shows the energy splitting between the SO band and the HH band and Figure 5.9(b) the heavy/light hole band energy splitting of biaxially compressively strained Ge grown on a [001] oriented $\text{Si}_{1-x}\text{Ge}_x$ substrate as a result of EPM calculation. For higher compressive strain the heavy/light hole band splitting saturates [Fischetti96a].

Figure 5.10(a) depicts the energy splitting between the SO band and the HH band and Figure 5.10(b) the heavy/light hole band splitting energies of compressively

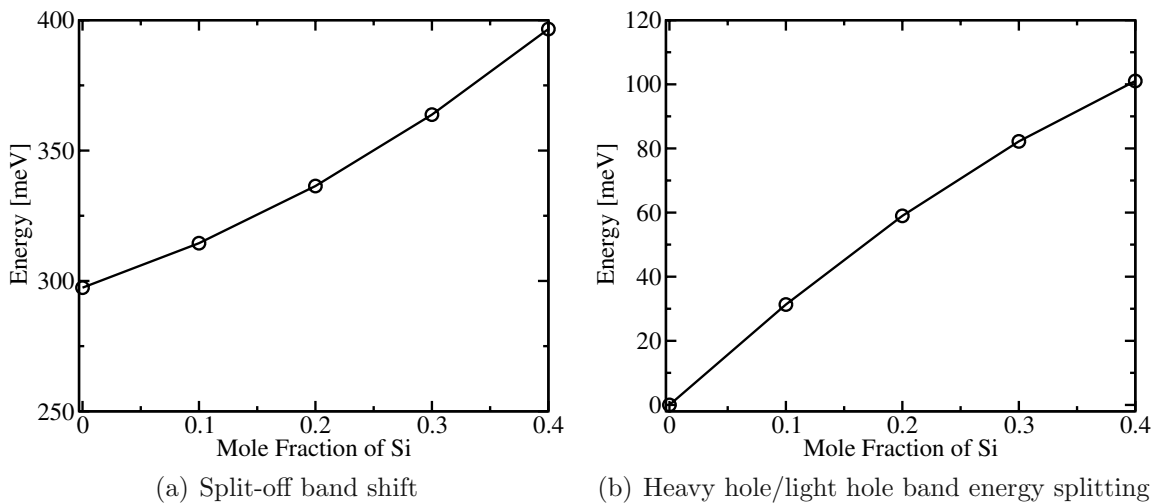


Figure 5.9: Split-off band shift relative to the valence band edge and energy splitting of heavy hole/light hole bands in strained Ge grown on a $\text{Si}_x\text{Ge}_{1-x}$ layer.

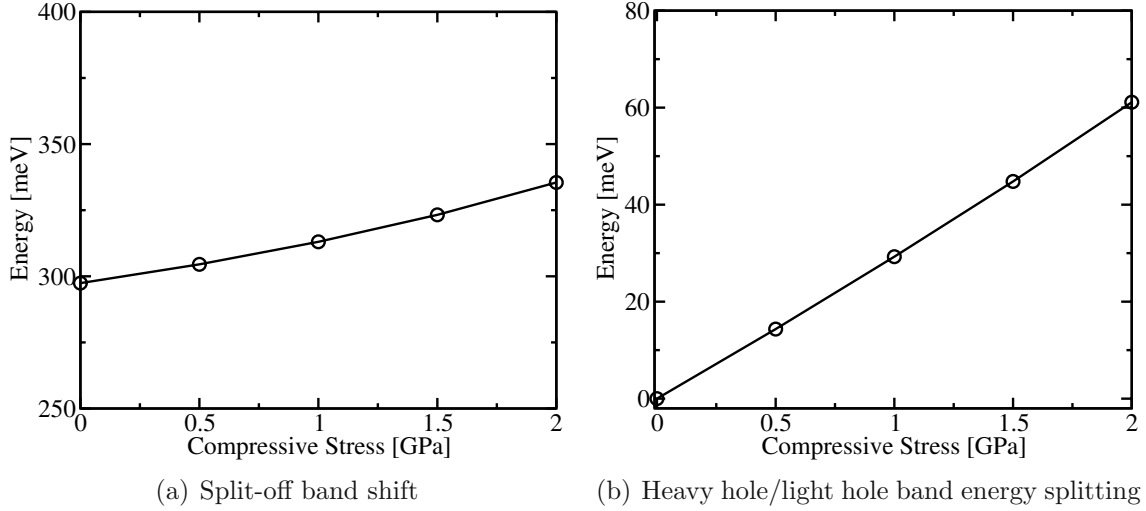


Figure 5.10: Split-off band shift relative to the valence band edge and energy splitting of heavy hole/light hole bands of compressively stressed Ge in [110] direction.

stressed Ge in [110] direction. The splitting energy rises almost linearly with compressive stress in [110] direction for the shown range of pressure. In these strain configurations the HH band is the lowest band and therefore defines the valence band edge whereas for tensile uniaxial strain the LH band is below the HH band. In any case the band splitting reduces the density of states in the low energy regime and suppresses interband scattering, which increases the mobility.

5.4.2 Effective mass change

A change in the effective mass can also contribute to the mobility gain [Wang06]. Figure 5.11 shows an equi-energy surface of the HH band at 200 meV as a result of EPM calculation. Carrier population follows the wing shaped form of the band. These wings are indicated as OW in the case of an off-plane wing and as IW for the in-plane wings with respect to the transport plane in (001). For relaxed Ge these wings are evenly populated, but they are not equivalent regarding transport, which is shown for the in-plane wings in Figure 5.12. For each wing an effective mass can be defined [Wang06]. For electric field in [110] direction the curvature of the equi-energy surface shows heavy masses in the wings IW2 and IW4, whereas for IW1 and IW3 the wings exhibit lower masses. Carriers in the off-plane wings exhibit an intermediate mass.

Under strain some of the wings move up in energy and some move down. This leads to a repopulation effect where the lowest wings get more populated and determine the mobility behavior.

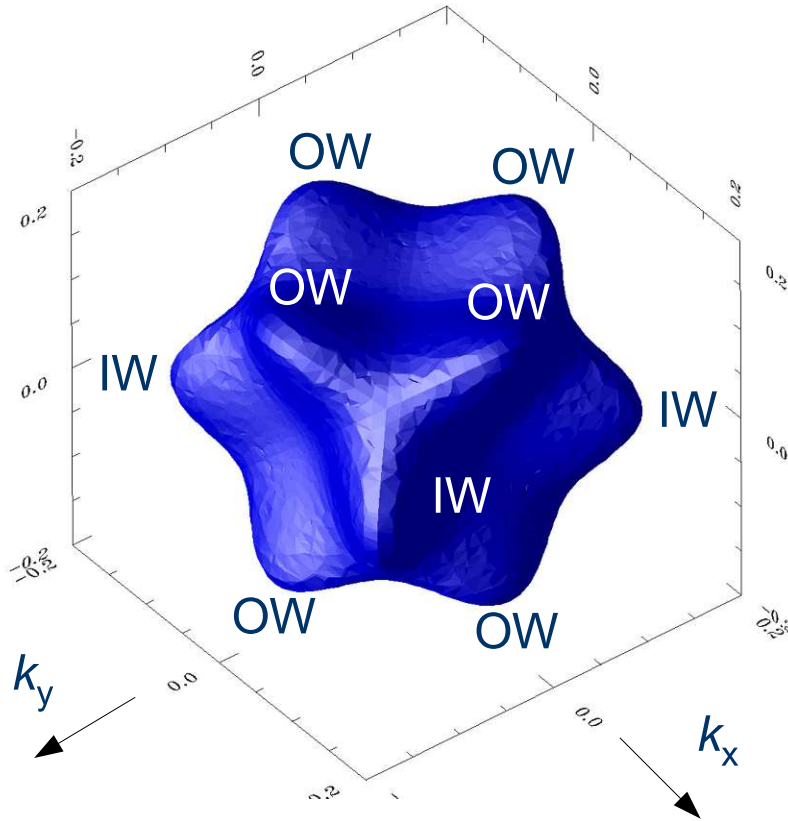
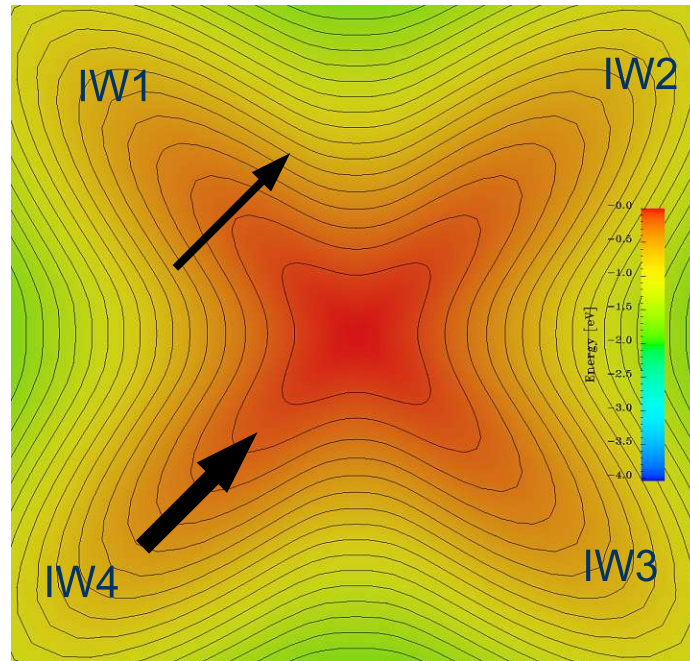


Figure 5.11: Equi-energy surface at 200 mV of the heavy hole band of relaxed Ge. OW indicates an off-plane wing and IW an in-plane wing.

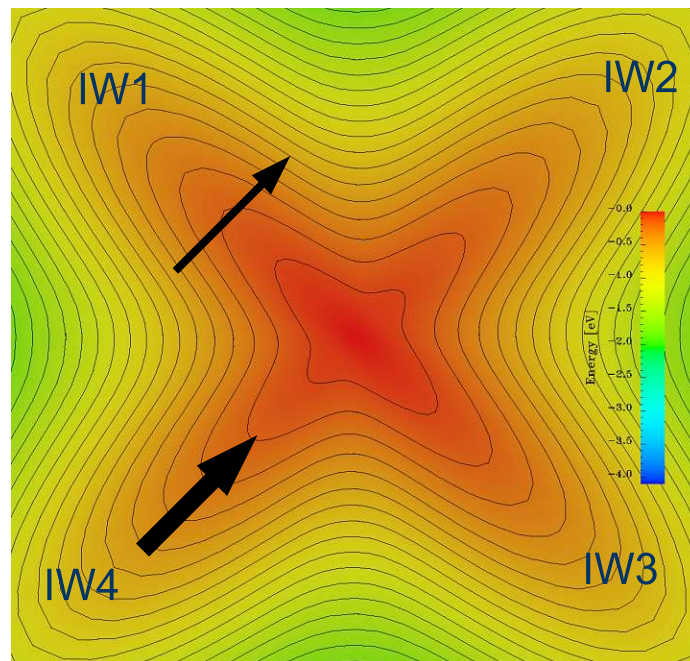
As shown in Figure 5.12(b), for uniaxial compressive stress in $[110]$ the lower mass wings IW1 and IW3 are lowered in energy and therefore higher populated, which leads to a mobility gain for transport along the $[110]$ direction.

5.5 Low Field Mobility of Holes in Strained Ge

The hole mobility of unstrained Ge, being approximately four times higher than that of Si, can be further enhanced by stress engineering. This has been shown in previous experimental and theoretical works for biaxially strained Ge epitaxially grown on a $[001]$ oriented $\text{Si}_x\text{Ge}_{1-x}$ substrate [Fischetti96a][Lee01][Leitz01][Ritenour03]. In the following hole transport properties of arbitrarily stressed/strained Ge are analyzed by means of full-band Monte Carlo simulation. Fig. 5.13 shows the in-plane low field mobility versus mole fraction of Si in the $\text{Si}_x\text{Ge}_{1-x}$ substrate. For a mole fraction $x = 0.4$ the low field hole mobility is enhanced by a factor of 3.38 to $6350 \text{ cm}^2/\text{Vs}$. This mole fraction corresponds to biaxial compressive strain of 1.7% in the Ge layer.



(a) Relaxed



(b) Compressive stress

Figure 5.12: k_x - k_y plane of the heavy hole band of Ge. The thick arrow indicates a heavy effective mass for transport in $[110]$ direction and the thin arrow a low effective mass.

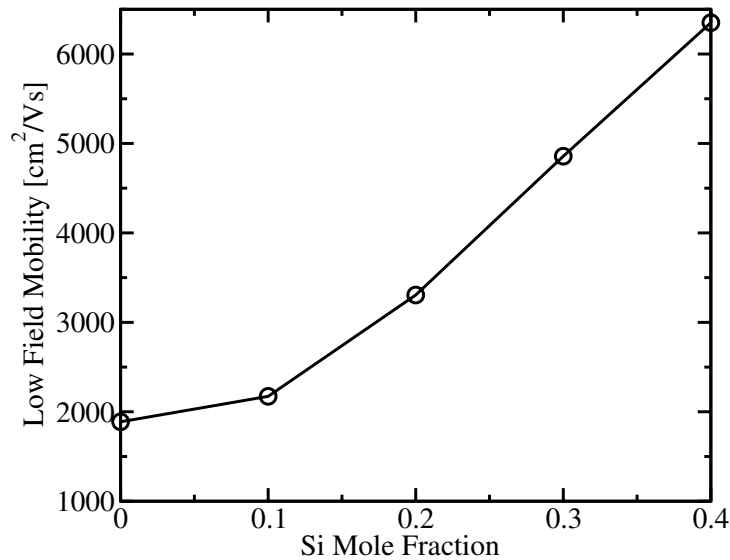


Figure 5.13: In-plane low field mobility of holes in biaxially compressed Ge grown on a $\text{Si}_x\text{Ge}_{1-x}$ substrate.

Fig. 5.14 depicts the in-plane hole mobility at low electric field for uniaxial compressive stress in $[110]$ direction. In Si technology p-MOS devices with uniaxially stressed channels in this configuration are already fabricated in large volumes [Ghani03]. A strong anisotropy with the most pronounced mobility enhancement in stress direction can be observed. Stress of 1.5GPa enhances the low field mobility by a factor of 2.55 to $4790 \text{ cm}^2/\text{Vs}$.

In Figure 5.15 the energy distribution functions for holes in relaxed and uniaxially stressed Ge are compared. Compressive stress is applied in $[110]$ direction. As a result of stress the hole distribution is shifted to higher energies, which is in accordance with the calculated mean hole energy of 43 meV for relaxed Ge and 56 meV for strained Ge. This result is caused by the alteration of the DOS under stress.

5.6 High Field Mobility of Holes in Strained Ge

In Figure 5.16 the velocity versus field characteristics for holes in biaxially strained Ge on a $\text{Si}_x\text{Ge}_{1-x}$ substrate is depicted. The field is applied in $[100]$ direction. The highest mobility gain can be observed in the low field regime while the curves converge in the high field regime to a saturation velocity of $8 \cdot 10^6 \text{ cm/s}$.

Figure 5.17 presents the velocity versus field characteristics for uniaxial compressive stress and field in $[110]$ direction. In the low field regime the curves show a superlinear increase of velocity with increasing stress, while at high fields the curves converge as observed for biaxial strain.

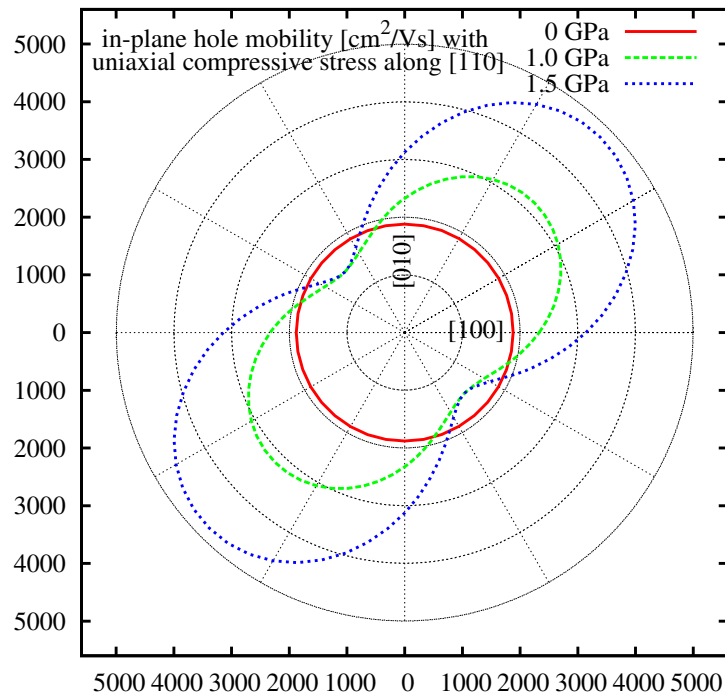


Figure 5.14: Low field hole mobility in the (001) plane of bulk Ge for uniaxial [110] compressive stress.

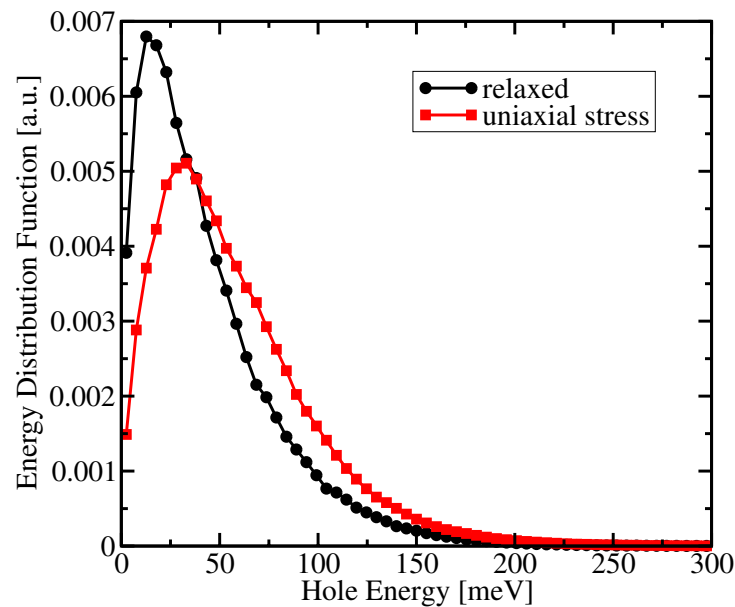


Figure 5.15: Energy distribution function for holes in equilibrium for relaxed Ge and Ge with an applied uniaxial compressive stress of 2 GPa in [110] direction.

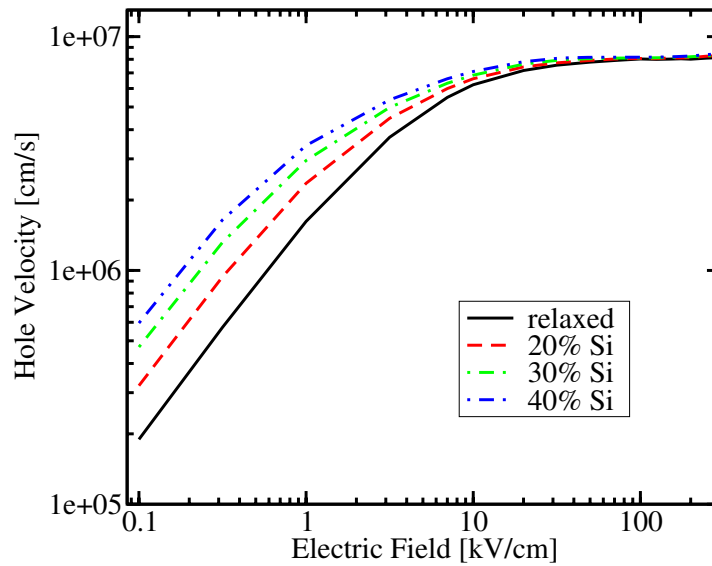


Figure 5.16: Hole velocity versus electric field in [100] for biaxially compressed Ge grown on a $\text{Si}_x\text{Ge}_{1-x}$ substrate.

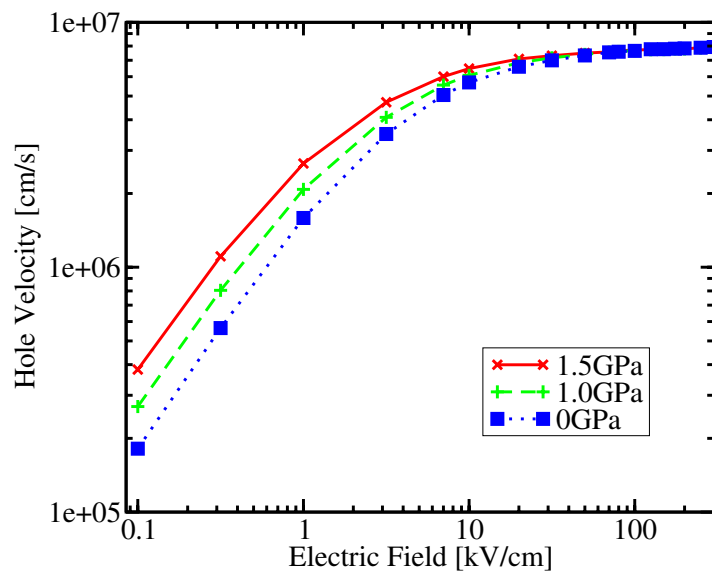


Figure 5.17: Hole velocity as a function of the electric field in compressively stressed Ge for field and stress in [110] direction.

Chapter 6

Simulation of Blocked Impurity Band Devices

6.1 Introduction

Blocked impurity band (BIB) photo detectors [Stetson86], invented by Petroff and Stapelbroek [Petroff86], are usually designed for the mid- to far-infrared range from $10 \mu\text{m}$ to $1000 \mu\text{m}$ wavelength. This wavelength range gained considerable importance in astronomy since the molecular and atomic emission lines from species like O, C or H_2O are within this range and far away objects are often hidden by interstellar dust clouds which absorb higher energy photons. On the other hand the atmosphere filters most of the infrared radiation and so exploring the infrared spectrum got an significant upturn with the realization of space based observation facilities such as the Spitzer Space Telescope where BIB detectors are applied in the form of detector arrays [Beeman07][Gehrz07].

BIB detectors deliver high quantum efficiency in a volume much smaller than in conventional photoconductors because of their much higher primary doping. Thus, BIB detectors are more resistant to the deleterious effects of radiation and offer a high signal to noise ratio. They offer also an extended wavelength response, which is caused by the formation of the impurity band and do not suffer from a transient response with memory like effects such as conventional photo detectors exhibit in the low temperature regime [Haegel03a]. Depending on the implementation BIB detectors can be set up for intensity measurement as well as photo multipliers with single phonon detection.

The schematic view of an n-type BIB detector is shown in Figure 6.1. It consists of a heavily – but not degenerately – doped layer of width d with donor concentration N_D so that the dopants form an impurity band in which carrier hopping occurs [Miller60].

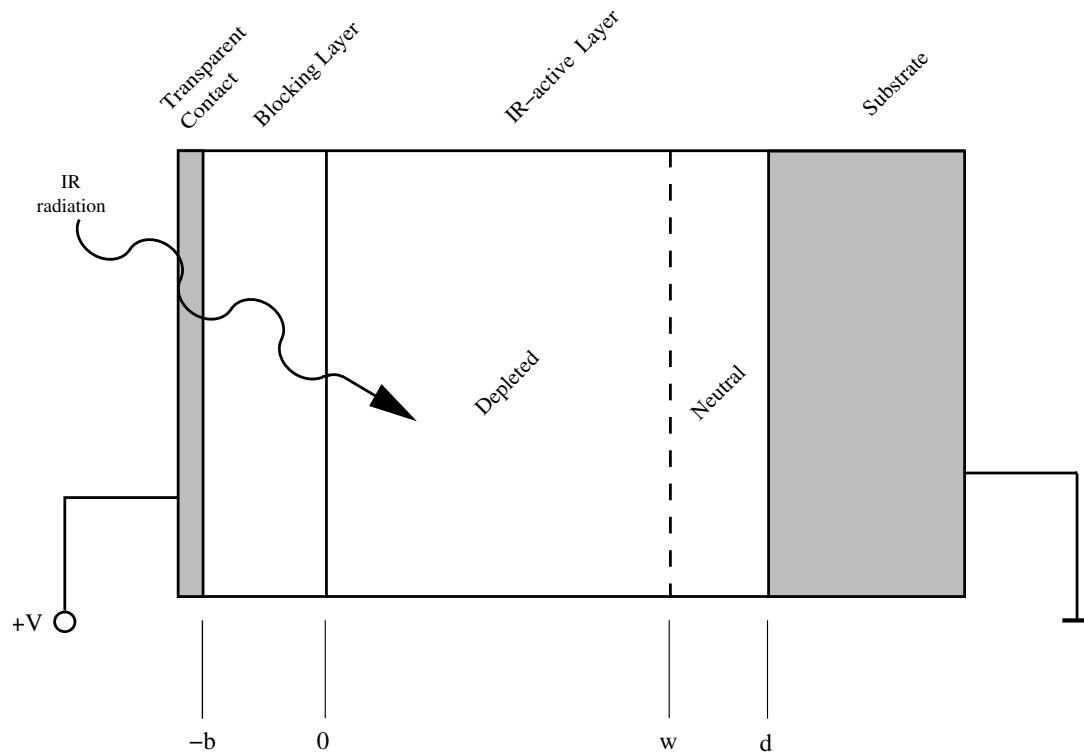


Figure 6.1: Schematic of an n-type BIB device.

This region is referred to as the infrared (IR)-active layer because an incoming photon can lift an electron from the impurity band to the conduction band. The IR-active layer is also partly compensated by a much weaker acceptor doping with concentration N_A . Next to that layer comes an area of intrinsic Si of width b where hopping conduction is strongly suppressed. It is referred to as the blocking layer.

The contacts consist of degenerately doped Si. The contact next to the blocking layer is illuminated and must be transparent in the infrared regime. Typically, a BIB detector is manufactured by starting from a degenerately doped Si substrate on which then the IR-active layer and the blocking layer are epitaxially grown.

6.2 Operation of BIB Detectors

A BIB detector is usually operated at temperatures below 10K. This is necessary to suppress dark current originating from thermally generated carriers. As a second effect the acceptors in the IR-active region take their charge from the donors and get completely ionized,

$$N_{D^+} = N_{A^-} . \quad (6.1)$$

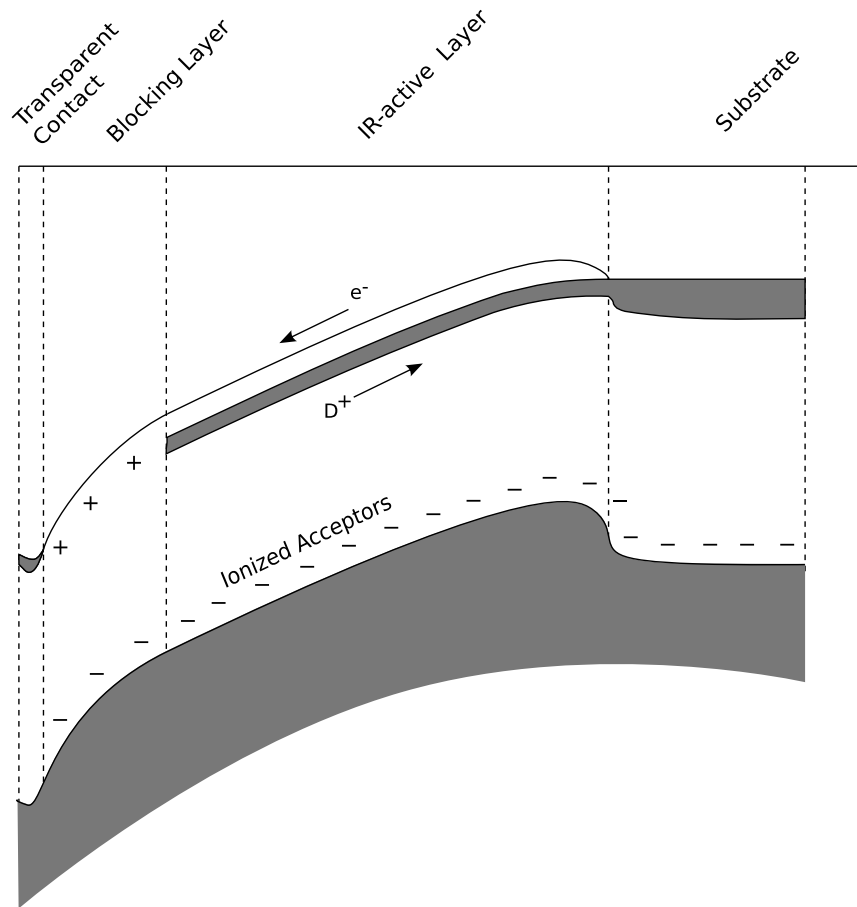


Figure 6.2: Energy band diagram of an n-type BIB device.

The negative charges N_{A-} on the fixed sites are immobile. If a reverse bias is applied, the N_{D+} charges move away from the blocking layer interface due to the impurity band hopping mechanism. Since impurity band hopping is suppressed in the blocking layer no new carriers are delivered from there and a depletion region of width w in the IR-active region is formed. In this case depletion refers to the N_{D+} charges. The remaining acceptor charges form a negative space charge region, while the electrons in the conduction band are collected at the transparent contact side after passing the blocking layer region.

Figure 6.2 depicts the energy band diagram for a BIB detector operating at reverse bias. The detection of a phonon takes place by generation of an electron hole pair. While the electron in the conduction band moves to the transparent contact, the hole can be interpreted as the charge of a D^+ donor moving to the other side by hopping conduction.

For an ideal BIB detector with no doping in the blocking layer a one dimensional Poisson equation can be formulated for the blocking and the depletion area, which

gives the depletion width as [Szmulowicz87]

$$w = \left(\frac{2\epsilon_s V}{eN_A} + b^2 \right)^{1/2} - b, \quad (6.2)$$

where V is the applied bias, and ϵ_s is the static dielectric permittivity. For Si $\epsilon_s = 11.7 \epsilon_0$, where ϵ_0 is the free space permittivity.

The electric field depends on the spatial coordinate x

$$E(x) = \left(\frac{eN_A}{\epsilon_s} \right) (w - x), \quad 0 \leq x \leq w, \quad (6.3)$$

in the depletion region and

$$E(x) = \left(\frac{eN_A}{\epsilon_s} \right) w, \quad -b \leq x \leq 0, \quad (6.4)$$

in the blocking layer. In the neutral region of the IR-active layer the field vanishes. The above formulae show that the maximum field occurs in the blocking layer. It depends on the depletion layer thickness w and on the acceptor doping concentration N_A , but is independent on the donor doping concentration N_D .

Another quantity of interest is the optical carrier generation rate $G(x)$. If the reflectivity of the transparent contact is R_1 and the reflectivity of the interface between the IR active layer and the substrate is R_2 , $G(x)$ can be written as [Szmulowicz80] [Szmulowicz86]

$$G(x) = \frac{\alpha \Phi (1 - R_1) (e^{-\alpha x} + R_2 e^{-2\alpha d} e^{\alpha x})}{1 - R_1 R_2 e^{-2\alpha d}}. \quad (6.5)$$

Here, Φ is the flux density of the incoming radiation and α is the optical absorption coefficient which depends on the photon wave length λ .

In the depletion region the continuity equation for the electrons in the conduction band is

$$e \frac{\partial n}{\partial t} = \frac{dJ_n}{dx} + \xi(x) J_n(x) + eg(x) \quad (6.6)$$

and for holes in the impurity band

$$e \frac{\partial p}{\partial t} = -\frac{dJ_p}{dx} + \xi(x) J_n(x) + eg(x). \quad (6.7)$$

Here, ξ is the impact ionization coefficient, J_n is the electron current density and J_p the hole hopping current density. The total generation rate $g(x)$ can be written as

$$g(x) = G(x) + G_0, \quad (6.8)$$

where G_0 is the thermal generation rate. It is assumed that the ionizing collisions are independent from each other so that the probability ξ of ionizing collisions per unit length can be meaningfully defined [McIntyre66]. Equations (6.6) and (6.7) are solved by multiplication by the integrating factors

$$M(x) = \exp\left(\int_0^x \xi(x')dx'\right) = M(w) = \exp\left(\int_x^w \xi(x')dx'\right). \quad (6.9)$$

As a result the total current density $J = J_p(x) + J_n(x)$ is obtained for the steady state as [Szmulowicz87]

$$J = M(0)J_p(0) + M(w)J_n(w) + e \int_0^w g(x)M(x)dx. \quad (6.10)$$

The current density $J_p(0)$ in equation (6.10) can be interpreted as positive donor charges which are injected at $x = 0$. Because of the low mobility of these hopping carriers they undergo no multiplication, hence $M(0) = 1$. On the other hand electrons injected at the right side at $x = w$ are multiplied due to the avalanche effect by $M(w)$ after traveling the distance of the depletion region. Carriers generated in the depletion region by thermal or optical generation undergo a position dependent multiplication by $M(x)$ which is taken into account by the last term on the right hand side of (6.10).

Equation (6.10) can be simplified if an ideal blocking layer is assumed, which prevents the injection of hopping carriers so that $J_p(0) = 0$. Furthermore, it can be assumed that the current density $J_n(w)$ which stems from diffusion of carriers from the heavily doped neutral part of the IR-active region is small enough to be neglected. This simplifies the equation for the total current density to

$$J = e \int_0^w g(x)M(x)dx. \quad (6.11)$$

In a macroscopic formulation the impact ionization coefficient can be written as [Sze81] [Stillman77]

$$\xi(x) = N_D \sigma_I \exp\left(-\frac{E_c}{E(x)}\right). \quad (6.12)$$

Here, N_D is the majority dopant concentration, σ_I is the cross section for impact ionization and E_c is the critical field for impact ionization. With (6.12) the integrating factor $M(x)$ can be obtained as

$$M(x) = \exp \left[N_D \sigma_I \left(w e^{-\frac{A}{w}} - (w-x) e^{-\frac{A}{w-x}} - A \int_{\frac{A}{w}}^{\infty} \frac{e^{-t}}{t} dt + A \int_{\frac{A}{w-x}}^{\infty} \frac{e^{-t}}{t} dt \right) \right] \quad (6.13)$$

with the parameter

$$A = \frac{\epsilon_s E_c}{e N_A}. \quad (6.14)$$

The two integrals in (6.13) have to be solved numerically since there is no solution in closed form.

6.3 Hopping Conduction

Semiconductors exhibit intrinsic conductivity at sufficiently high temperatures due to thermal activation of carriers from the valence band to the conduction band. A wide band gap causes a rapid decrease of this kind of conduction at lower temperatures. Therefore shallow impurities become the most important provider for free carriers as their ionization energy is much lower than the bandgap. At low temperatures the thermal activation energy is so small that the carriers are recaptured by the impurities. This is a gradual process known as *freeze-out*.

At even lower temperatures the impurities are completely frozen out and hopping conduction is the prominent transport effect. In the case of no compensation hopping conduction can occur – if an n-type semiconductor is considered – when an electron is removed from a neutral donor site and moves to a neighbor neutral donor site, creating an overcharged impurity there [Nishimura65]. The conductivity σ caused by this thermally activated process is characterized by an activation energy ε_2

$$\sigma = \sigma_2 \exp \left(-\frac{\varepsilon_2}{k_B T} \right). \quad (6.15)$$

Here, σ_2 as well as the activation energy ε_2 depend on the average distance between the impurities.

In n-type BIB devices the donor concentration is slightly compensated by a frozen acceptor doping. The acceptors are ionized with carriers from the impurity band,

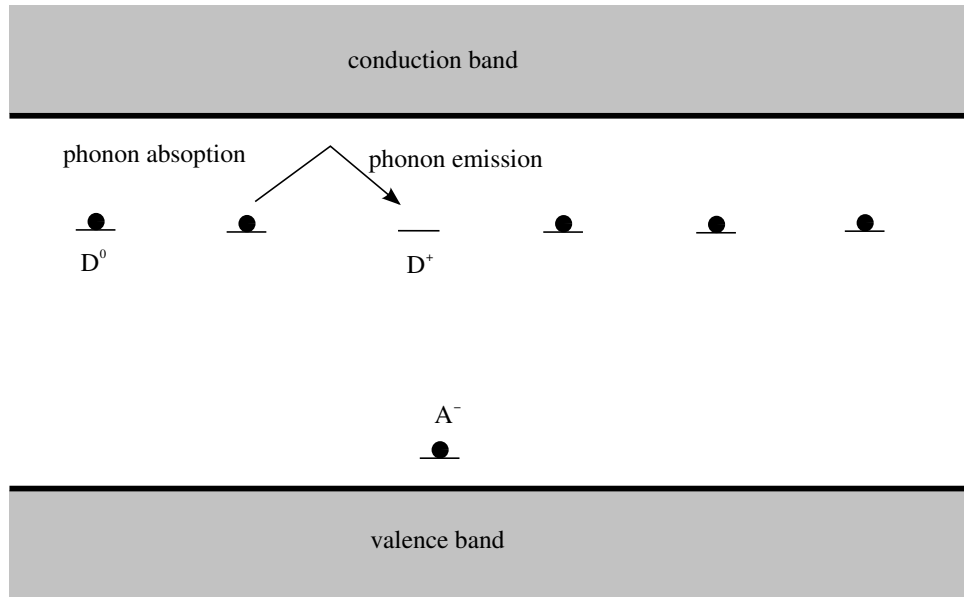


Figure 6.3: Nearest neighbor hopping illustrated in a n-type BIB device. The electron is transferred from a D^0 donor to a D^+ donor by the assistance of a phonon absorption and emission process.

leaving positively charged donor sites in the impurity band even at the lowest temperatures. Such a setup gives rise to another carrier hopping effect, where the electron of a neutral donor site is transferred to a positively charged neighbor donor site. This process is assisted by the absorption and emission of a phonon, lifting the electron to an excited intermediate state as illustrated in Figure 6.3 for a n-type device. The conductance can be described with another thermal activation energy ε_3 [Shklovskii84]

$$\sigma = \sigma_3 \exp\left(-\frac{\varepsilon_3}{k_B T}\right). \quad (6.16)$$

This nearest neighbor hopping process is the most important hopping mechanism within BIB devices, but at very low temperatures there is another hopping process, namely the so called variable-range hopping mechanism. When the thermal energy $k_B T$ becomes very low the hopping carrier may not find a suitable energy state within the possible range at neighbor impurity sites. In this situation the carrier may be transferred to a more distant site despite of the small wavefunction overlap [Shklovskii84].

6.4 Monte Carlo Simulation of BIB Detectors

A two step procedure is used to simulate the properties of BIB detectors. First the electrostatic field is calculated using a conventional TCAD device simulator. In this work MINIMOS-NT [IuE04] was used. This field is then fed to the Monte Carlo simulator where in a second step the Boltzmann equation is solved. The detector is modeled as a one-dimensional device.

The following sections show some features for Monte Carlo simulation at very low temperatures and present a concept for an alternative impact ionization model to capture a non-Markovian avalanche effect.

6.4.1 Neutral Impurity Scattering

At very low temperatures neutral impurity scattering can significantly contribute to the total scattering rate. In literature several attempts exist to describe neutral impurity scattering [Sclar56][Kwong90][Itoh97]. For the sake of simplicity the expression of Erginsoy [Erginsoy50][Bhattacharyya93] is used for the scattering probability

$$\Gamma_{ni} = \frac{20 \cdot 4\pi\epsilon_0\epsilon_s N_n \hbar^3}{m_v^* e^2} \quad (6.17)$$

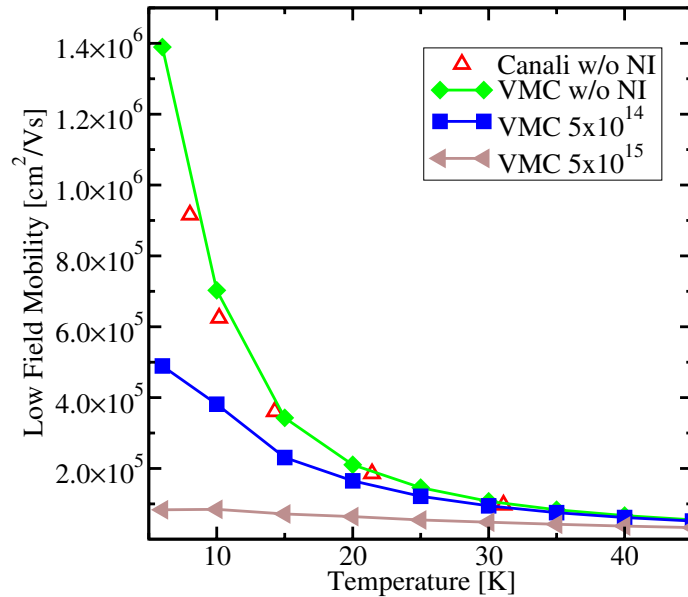


Figure 6.4: Low field electron mobility versus lattice temperature for several neutral impurity concentrations in Si as a result of Monte Carlo simulation. Simulation data without impurity scattering is taken from [Canali75].

In (6.17) N_n is the neutral impurity concentration and m_v^* is the effective mass in the valley v . Erginsoy's model is based on a parabolic band approximation and gives an energy-independent result for the scattering probability, whereas Sclar's [Sclar56] or other more sophisticated approaches lead to an energy-dependent formulation.

Figure 6.4 depicts the low field mobility of electrons in Si in the low temperature regime. Shown are MC simulation results based on phonon scattering and in addition neutral impurity scattering when indicated. It is shown that neutral impurities cause a mobility reduction at low temperatures, and therefore neutral impurity scattering has to be considered in simulation of BIB devices.

6.4.2 Non-Markovian Impact Ionization Model

An BIB detector can also operate as a single photon multiplier if the bias voltage is large enough to cause an avalanche effect to due impact ionization. In the following, an impact ionization model is described which captures the non-Markovian nature of the avalanche [Sinitsa02][Petroff87].

It is assumed that impact ionization takes place exclusively in the depletion region and that the carriers do not recombine again. The impact ionization rate $S_{\text{BIB}}^{\text{II}}$ is derived from (3.52), taking into account that the rate depends on the impurity concentration N_D^0 of the impurity band

$$S_{\text{BIB}}^{\text{II}} \propto N_D^0 \cdot S^{\text{II}}. \quad (6.18)$$

When an impact ionization event occurs the energy and position in real space of the secondary particle is saved in a table. The energy is calculated by randomly distributing the primary carrier energy between the primary and the secondary carrier. The primary carrier trajectory is followed until it ends at a contact. On its way through the depletion region several impact ionization events may occur which produce new entries in the table. After the original carrier is collected at a contact the table is reduced by the entry of the already executed carrier and the simulation continuous with the carrier defined by the next table entry. The simulation is finished when there are no more table entries to be processed. With this procedure all carriers of the avalanche are simulated under consideration of their individual trajectory.

Because of their low mobility the carriers in the impurity band experience no avalanche multiplication. As another consequence of the low mobility, the slow carriers in the impurity band cause a local breakdown of the field in the areas of avalanche generation [Petroff87]. This leads to a limitation of carrier multiplication. With Monte Carlo this effect can only be treated by applying a self-consistent simulation scheme.

6.5 Results

In the following simulations are based on the specification of the n-type device given in Table 6.1. It is assumed that the doping concentration changes abruptly at the blocking layer/active layer interface and that the blocking layer is undoped. In the following the orientation of the device is so that the blocking layer is positioned on the right side starting at 26.5 μm . The degenerately doped contacts are not included in the simulation domain. Results obtained with different specifications than in Table 6.1 are indicated as they occur.

Device Parameter	Value
Substrate Material	Si
Active Region: n^+ Doping	Sb, $N_D = 4 \cdot 10^{17} \text{ cm}^{-3}$
Active Region: p^- Doping	B, $N_A = 2 \cdot 10^{12} \text{ cm}^{-3}$
Blocking Layer Thickness	$b = 3.5 \mu\text{m}$
Active Layer Thickness	$d = 26.5 \mu\text{m}$
Bias Voltage	$V = 1.0 \text{ V}$
Lattice Temperature	$T = 7 \text{ K}$

Table 6.1: Specification of the n-type BIB device.

6.5.1 Electrostatic Field

The electrostatic field within the BIB device is obtained from a conventional TCAD-device simulation using MINIMOS-NT. Figure 6.5 shows the electrostatic field in an n-type BIB device at several bias voltages V . The results show very good agreement with simulation results from literature [Haegel03b][Huffman92]. Figure 6.6 depicts the electrostatic field in an n-type BIB device for several acceptor concentrations in the IR-active region. Both results agree well with the analytical solutions (6.3) and (6.4).

These figures also illustrate some basic rules for the design of BIB devices. It is shown how the depletion area is determined by the bias V and the compensation doping. To achieve good quantum efficiency it is necessary to have a large depletion area, because this is the part of the IR-active layer where the field is non-zero and so the optical generated electrons are able to proceed to the contact.

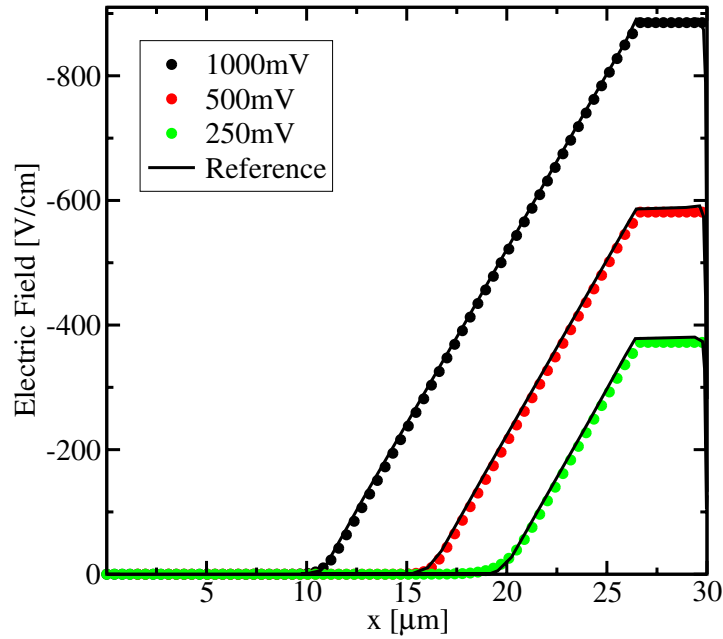


Figure 6.5: Electrostatic field in an n-type BIB device at several bias voltages. The results show very good agreement with simulation results from literature [Haegel03b][Huffman92].

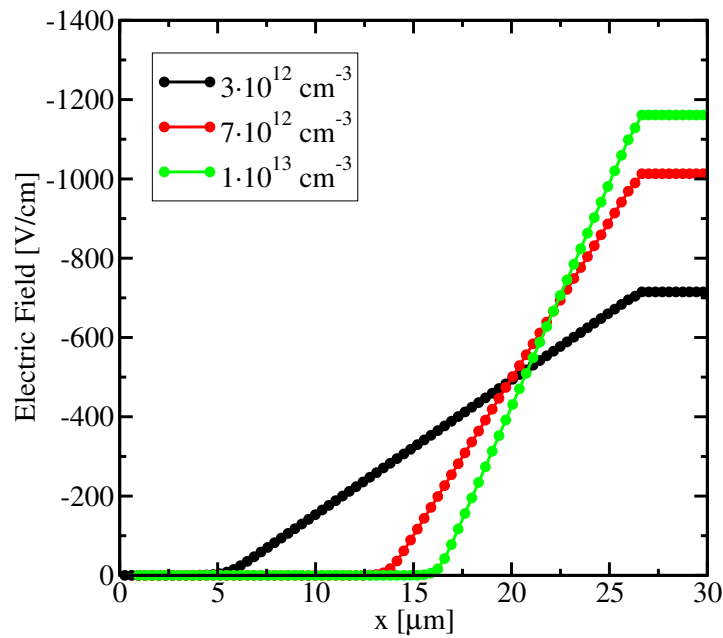


Figure 6.6: Electrostatic field in an n-type BIB device for several acceptor concentrations in the active region.

On the other hand, to avoid a breakdown condition, the depletion region must not grow into the contact. As a consequence the compensating acceptor doping must be well controlled at a quite low level.

It should also be noted that the field distribution does not depend on the majority doping, which forms the impurity band. In principle, a higher donor concentration leads to higher quantum efficiency, but also introduces band broadening, which in turn leads to unwanted thermal dark current.

6.5.2 BIB Device as a Single Photon Counter

For the following simulations the field distribution is obtained by a conventional TCAD simulator and then passed to the Monte Carlo simulator, here VMC. Then a non-selfconsistent Monte Carlo simulation is performed.

When a photon is detected, it lifts an electron from the impurity band to the conduction band, which – if the field is sufficiently large – causes an avalanche multiplication. Two positions for the photon detection at $x_1 = 10 \mu\text{m}$ and $x_2 = 14 \mu\text{m}$ are evaluated as depicted in Figure 6.7. Each injection position is simulated 1000 times. In this setup the bias voltage $V = 2.5 \text{ V}$ and the acceptor doping concentration in the IR-active region is $N_A = 5 \cdot 10^{12} \text{ cm}^{-3}$. All other device specifications are in accordance with Table 6.1.

Figure 6.9 depicts the energy distribution of electrons collected at the contact for an assumed optical generation of the original electron at position x_1 . The mean energy is 46.4 meV which is only slightly below the energy of electrons starting at position x_2 . This indicates that the impact ionization limits the energy gain of the carriers as they proceed through the depletion region.

Figure 6.10 and Figure 6.11 show the shape of the electron avalanche, when it reaches the contact, for electrons generated at position x_1 and x_2 respectively.

It should be noted that these results are not calibrated against measurement data and therefore only give qualitative insights about the avalanche behavior.

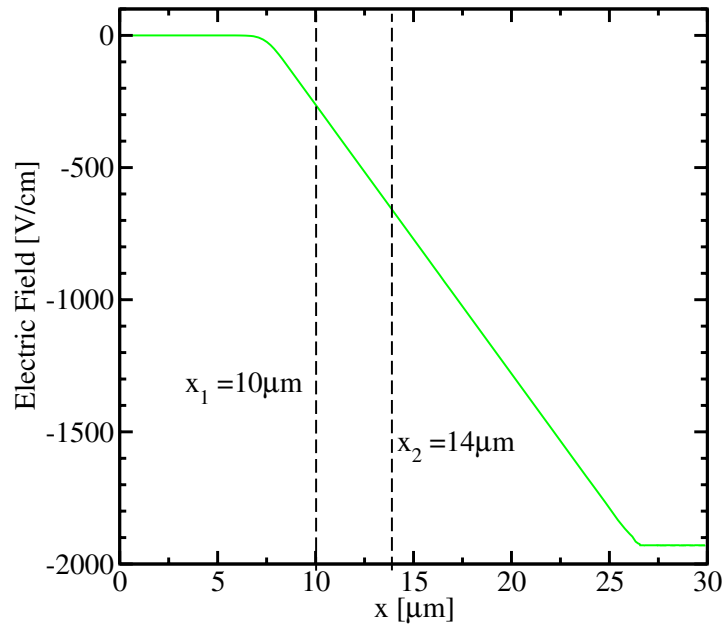


Figure 6.7: Electrostatic field in an n-type BIB device. The dotted lines indicate the detection of two photons at the positions x_1 and x_2 .

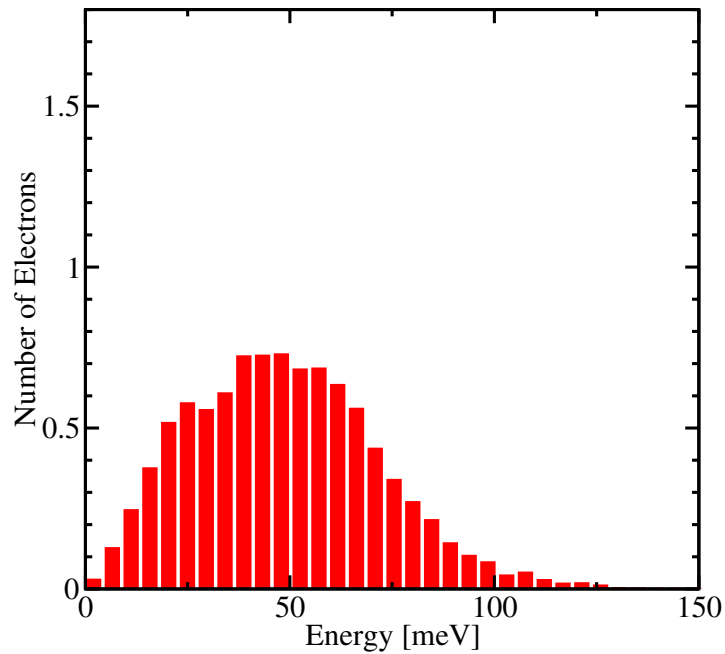


Figure 6.8: Energy distribution of electrons at the contact caused by a photon detected at $x_1 = 10 \mu\text{m}$.

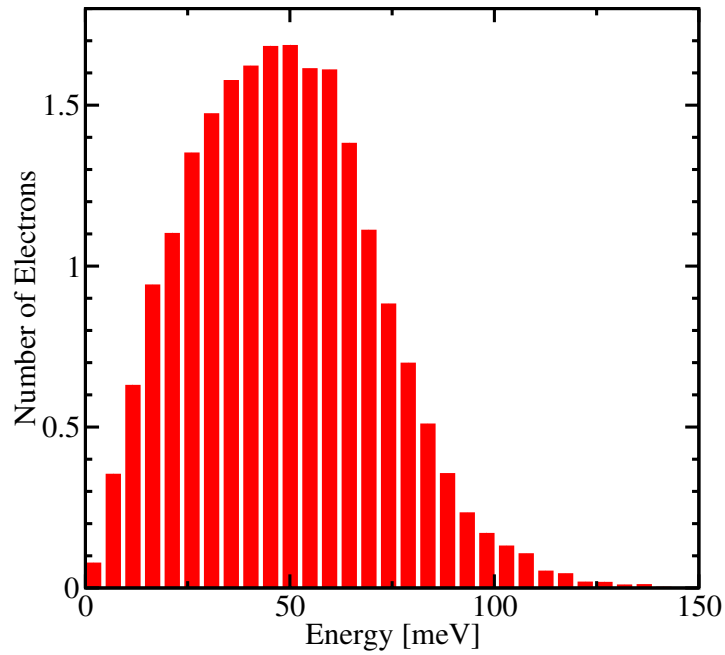


Figure 6.9: Energy distribution of electrons at the contact caused by a photon detected at $x_1 = 14 \mu\text{m}$.

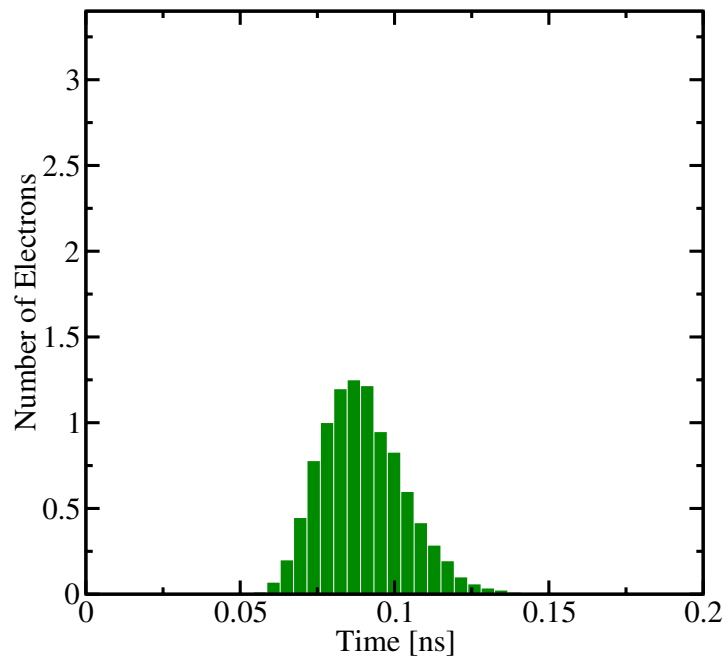


Figure 6.10: Distribution of the arrival time at the contact caused by a photon detected at $x_2 = 10 \mu\text{m}$.

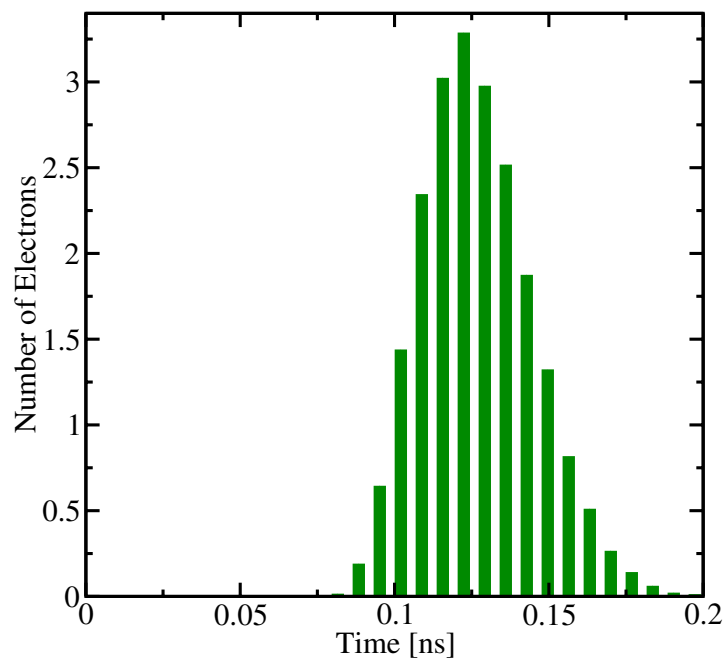


Figure 6.11: Distribution of the arrival time at the contact caused by a photon detected at $x_2 = 14 \mu\text{m}$.

Chapter 7

Summary and Conclusions

Due to the rapid progress of Si technology and the introduction of new device types and materials, it is a challenging task to develop and improve models for TCAD device simulation. In this development process it is essential to have access to reliable data from measurements, but as device fabrication gets more and more complex also experiments become more expensive and – as a major drawback – also more time consuming. As a consequence it is of increasing interest to obtain data by simulations based on more fundamental methods.

In this work it has been shown that Monte Carlo methods based on a full-band dispersion relation are a powerful tool in this respect. Full-band Monte Carlo is generally applicable to hot carrier problems, because an accurate representation of the band structure at higher energies is essential here. Beyond that, the simulator has been extended to handle transport in arbitrarily strained Si, Ge and SiGe alloys. This is an important feature, since modern high performance MOSFET devices rely heavily on strain engineering techniques to increase the performance. It has been exemplarily demonstrated that in Si the electron mobility is increased by a $\langle 110 \rangle$ strain setup and that in Ge the higher hole mobility compared to Si can be further increased by the introduction of strain.

These effects are explained by an evaluation and theoretical interpretation of band structure data from EPM calculations. It is concluded that the electronic mobility increase or decrease, depending on the setup, stems from an energy separation of the Δ valleys, which also lifts their degeneracy, and from a change in the effective masses in transport direction. For hole transport the latter effect is also valid, but there is also a contribution from the relative shift of the heavy hole, light hole and split-off bands.

It has been also demonstrated that the high computational costs of full-band Monte Carlo can be reduced by the implementation of performance optimizing features

SUMMARY AND CONCLUSIONS

like rejection algorithms or irregular mesh refinement in \mathbf{k} -space. These features in combination with the availability of successively increasing computational power indicate that full-band Monte Carlo will play a stronger role in device simulation in the future.

In this work Monte Carlo techniques are also applied to simulate blocked impurity band photo detectors. These devices operate at temperatures below 10 K. The scattering models were extended to deliver valid results in this temperature range. Some simulation results of the avalanche effect in blocked impurity band devices were presented. The avalanche effect can be used to operate the devices as single photons detectors.

Bibliography

- [Anghel03] D.V. Anghel. *Bravais Lattice Table*. 2003.
<http://folk.uio.no/dragos/Solid/>.
- [Arnold00] Douglas N. Arnold, Arup Mukherjee, and Luc Pouly. *Locally Adapted Tetrahedral Meshes Using Bisection*. SIAM J. Sci. Comput., vol. 22, no. 2, pages 431–448, 2000.
- [Ashcroft76] N. W. Ashcroft, and N. D. Mermin. “Solid state physics”. W. B. Saunders, Philadelphia, 1976.
- [Beeman07] J. W. Beeman, S. Goyal, L. A. Reichertz, and E. E. Haller. *Ion-implanted Ge:B far-infrared blocked-impurity-band detectors*. Infrared Physics & Technology, vol. 51, no. 1, pages 60–65, 2007.
- [Bernstein06] K. Bernstein, D. J. Frank, A. E. Gattiker, W. Haensch, B. L. Ji, E. J. Nowak S. R. Nassif and, D. J. Pearson, and N. J. Rohrer. *High Performance CMOS Variability in the 65-nm Regime and Beyond*. IBM J.Res.Dev., vol. 50, no. 4/5, pages 433–450, 2006.
- [Bhattacharyya93] K. Bhattacharyya, S. M. Goodnick, and J. F. Wager. *Monte Carlo simulation of electron transport in alternating-current thin-film electroluminescent devices*. J.Appl.Phys., vol. 73, no. 7, pages 3390–3395, 1993.
- [Bir74] G. L. Bir, and G. E. Pikus. “Symmetry and strain induced effects in semiconductors”. Wiley, New York, 1974.
- [Brooks51] H. Brooks. *Scattering by Ionized Impurities in Semiconductors*. Phys.Rev., vol. 83, page 879, 1951.

BIBLIOGRAPHY

- [Bufler01] F. M. Bufler, A. Schenk, and W. Fichtner. *Simplified model for inelastic acoustic phonon scattering of holes in Si and Ge*. J.Appl.Phys., vol. 90, no. 5, pages 2626–2628, 2001.
- [Canali75] C. Canali, C. Jacoboni, F. Nava, G. Ottaviani, and A. Alberigi-Quaranta. *Electron Drift Velocity in Silicon*. Phys. Rev. B, vol. 12, no. 6, pages 2265–2284, 1975.
- [Cartier93] E. Cartier, M. V. Fischetti, E. A. Eklund, and F. R. McFeely. *Impact Ionization in Silicon*. Appl. Phys. Lett., vol. 62, no. 25, pages 3339–2241, 1993.
- [Conwell67] E.M. Conwell. “High field transport in semiconductors”, volume 9 of *Solid State Physics*. Academic Press, New York, London, 1967.
- [Dhar06] S. Dhar, H. Kosina, G. Karlowatz, E. Ungersboeck, T. Grasser, and S. Selberherr. *High-field electron mobility model for strained-silicon devices*. IEEE Trans.Electron Devices, vol. 53, no. 12, pages 3054–3062, 2006.
- [Erginsoy50] Cavid Erginsoy. *Neutral Impurity Scattering in Semiconductors*. Phys.Rev., vol. 79, no. 6, pages 1013–1014, 1950.
- [Ferry91] D.K. Ferry. “Semiconductors”. Macmillan, New York, 1991.
- [Fischer99] Björn Fischer. *A Full-Band Monte Carlo Charge Transport Model for Nanoscale Silicon Devices Including Strain*. PhD thesis, University Hannover, Germany, 1999.
- [Fischetti96a] M. V. Fischetti, and S. E. Laux. *Band structure, deformation potentials, and carrier mobility in strained Si, Ge, and SiGe alloys*. J.Appl.Phys., vol. 80, no. 4, pages 2234–2252, 1996.
- [Fischetti96b] M.V. Fischetti, and S.E. Laux. *Monte Carlo simulation of electron transport in Si: The first 20 years*. In G. Baccarani, and M. Rudan, editors, 26th European Solid State Device Research Conference, pages 813–820, Bologna, Italy, 1996. Editions Frontiers.
- [Fleischmann99] Peter Fleischmann. *Mesh Generation for Technology CAD in Three Dimensions*. Dissertation, Institut für Mikroelektronik, Technische Universität Wien, 1999.
<http://www.iue.tuwien.ac.at/phd/fleischmann>.

BIBLIOGRAPHY

- [Gehrz07] R. D. Gehrz, T. L. Roellig, M. W. Werner, G. G. Fazio, J. R. Houck, F. J. Low, G. H. Rieke, B. T. Soifer, D. A. Levine, and E. A. Romana. *The NASA Spitzer Space Telescope*. Review of Scientific Instruments, vol. 78, no. 1, page 011302, 2007.
- [Ghani03] T. Ghani, M. Armstrong, C. Auth, M. Bost, P. Charvat, T. Hoffmann, K. Johnson, C. Kenyon, J. Klaus, B. McIntyre, K. Mistry, J. Sandford, M. Silberstein, S. Sivakumar, P. Smith, K. Zawadzki, S. Thompson, , and M. Bohr. *A 90nm high volume manufacturing logic technology featuring novel 45nm gate length strained silicon CMOS transistors*. In Proc.Intl.Electron Devices Meeting, pages 11.6.1–3, 2003.
- [Ghosh06] B. Ghosh, X. F. Fan, and L. F. Register. *Monte Carlo study of strained Germanium nanoscale bulk pMOSFETs*. IEEE Trans.Electron Devices, vol. 53, no. 3, pages 533–537, 2006.
- [Haegel03a] N. M. Haegel. *BIB detector development for the far infrared: from Ge to GaAs*. In M. Razeghi, and G. J. Brown, editors, Quantum Sensing: Evolution and Revolution from Past to Future. Proceedings of the SPIE, volume 4999, pages 182–194, 2003.
- [Haegel03b] N. M. Haegel, S. A. Samperi, and A. M. White. *Electric field and responsivity modeling for far-infrared blocked impurity band detectors*. J.Appl.Phys., vol. 93, no. 2, pages 1305–1310, 2003.
- [Haensch06] W. Haensch, E. J. Nowak, and Dennard R. H. *Silicon CMOS Devices Beyond Scaling*. IBM J.Res.Dev., vol. 50, no. 4/5, pages 339–361, 2006.
- [Harrison56] W. A. Harrison. *Scattering of electrons by lattice vibrations in nonpolar crystals*. Phys.Rev., vol. 104, no. 5, pages 1281–1290, 1956.
- [Hinckley90] J. M. Hinckley, and J. Singh. *Influence of substrate composition and crystallographic orientation on the band structure of pseudomorphic Si-Ge alloy films*. Phys.Rev.B, vol. 42, pages 3546–3566, 1990.
- [Hooke78] R. Hooke. “De potentia restitutiva”. 1678.
- [Huffman92] J. E. Huffman, A. G. Crouse, B. L. Halleck, T. V. Downes, and T. L. Herter. *Si:Sb blocked impurity band detectors for infrared astronomy*. J.Appl.Phys., vol. 72, pages 273–275, July 1992.

BIBLIOGRAPHY

- [Intel07] Intel. *45nm technology*, 2007.
<http://www.intel.com/technology/45nm>.
- [Irie04] H. Irie, K. Kita, K. Kyuno, and A. Toriumi. *In-Plane Mobility Anisotropy and Universality Under Uni-Axial Strains in n- and p-MOS Inversion Layers on (100), (110), and (111) Si*. IEDM Techn. Dig., pages 225–228, 2004.
- [Itoh97] K. M. Itoh, T. Kinoshita, J. Muto, N. M. Haegel, W. Walukiewicz, O. D. Dubon, J. W. Beeman, and E. E. Haller. *Carrier scattering by neutral divalent impurities in semiconductors: Theory and experiment*. Phys.Rev.B, vol. 56, no. 4, pages 1906–1910, 1997.
- [IuE04] IuE. *MINIMOS-NT 2.1 User's Guide*. Institut für Mikroelektronik, Technische Universität Wien, Austria, 2004.
<http://www.iue.tuwien.ac.at/software/minimos-nt>.
- [IuE06] IuE. *Vienna Monte Carlo 2.0 User's Guide*. Institut für Mikroelektronik, Technische Universität Wien, Austria, 2006.
<http://www.iue.tuwien.ac.at/software>.
- [Jacoboni83] C. Jacoboni, and L. Reggiani. *The Monte Carlo method for the solution of charge transport in semiconductors with applications to covalent materials*. Reviews of Modern Physics, vol. 55, no. 3, pages 645–705, 1983.
- [Jungemann03] C. Jungemann, and B. Meinerzhagen. “Hierarchical Device Simulation”. Springer, Wien New York, first edition, 2003.
- [Kalos86] M. H. Kalos, and P. A. Whitlock. “Monte Carlo methods, volume I: Basics”. Wiley-Interscience Publications, John Wiley and Sons, New York, 1986.
- [Karlowitz07] G. Karlowitz, W. Wessner, and H. Kosina. *Effect of Band Structure Discretization on the Performance of Full-Band Monte Carlo Simulation*. In 5th IMACS Symposium on Mathematical Modelling - 5th MATHMOD Vienna - Mathematics and Computers in Simulation - Transactions of IMACS, volume 5, pages 4.1–4.6. Elsevier, 2007.
- [Kittel96] C. Kittel. “Introduction to solid state physics”. John Wiley & Sons, 7 edition, 1996.
- [Kosina97] H. Kosina. *Efficient Evaluation of Ionized-Impurity Scattering in Monte Carlo Transport Calculations*. Phys.stat.sol.(a), vol. 163, pages 475–489, 1997.

BIBLIOGRAPHY

- [Kosina98] H. Kosina, and G. Kaiblinger-Grujin. *Ionized-Impurity Scattering of Majority Electrons in Silicon*. Solid-State Electron., vol. 42, no. 3, pages 331–338, 1998.
- [Kosina00] H. Kosina, M. Nedjalkov, and S. Selberherr. *Theory of the Monte Carlo Method for Semiconductor Device Simulation*. IEEE Trans. Electron Devices, pages 1898–1998, 2000.
- [Kossaczky94] Igor Kossaczky. *A Recursive Approach to Local Mesh Refinement in Two or Three Dimensions*. ELSEVIER Journal of Computational and Applied Mathematics, no. 55, pages 275 – 288, 1994.
- [Kwong90] K. C. Kwong, N. Y. Du, J. Callaway, and R. A. LaViolette. *Inelastic scattering of electrons by neutral impurities in semiconductors*. Phys.Rev.B, vol. 41, no. 18, pages 12666–12671, 1990.
- [Landau81] L.D. Landau, and E.M. Lifshitz. “Course in theoretical physics, vol. 3: Quantum mechanics non-relativistic theory”. Butterworth-Heinemann, 1981.
- [Lee01] M. L. Lee, C. W. Leitz, Z. Cheng, A. J. Pitera, T. Langdo, M. T. Currie, G. Taraschi, E. A. Fitzgerald, and D. A. Antoniadis. *Strained Ge channel p-type metal-oxide-semiconductor field-effect transistors grown on Si_{1-x}Ge_x/Si virtual substrates*. Appl.Phys.Lett., vol. 79, no. 20, pages 3344–3346, 2001.
- [Lehmann72] G. Lehmann, and M. Taut. *On the Numerical Calculation of the Density of States and Related Properties*. Phys. Status Solidi B, vol. 54, pages 469–477, 1972.
- [Leitz01] C. W. Leitz, M. T. Currie, M. L. Lee, Z.-Y. Cheng, D. A. Antoniadis, and E. A. Fitzgerald. *Hole mobility enhancements in strained Si/Si_{1-y}Ge_y p-type metal-oxide-semiconductor field-effect transistors grown on relaxed Si_{1-x}Ge_x (x < y) virtual substrates*. Appl.Phys.Lett., vol. 79, no. 25, pages 4246–4248, 2001.
- [Levinshtein99] M. Levinshtein, S. Rumyantsev, and M. Shur, editors. “Handbook Series on Semiconductor Parameters”, volume 1,2. World Scientific, London, 1999.
- [Maes90] W. Maes, K. De Meyer, and R. Van Overstraeten. *Impact Ionization in Silicon: A Review and Update*. Solid-State Electron., vol. 33, no. 6, pages 705–718, 1990.
- [Masetti83] G. Masetti, M. Severi, and S. Solmi. *Modeling of Carrier Mobility Against Carrier Concentration in Arsenic-, Phosphorus- and*

BIBLIOGRAPHY

- Boron-Doped Silicon*. IEEE Trans. Electron Devices, vol. ED-30, no. 7, pages 764–769, 1983.
- [McIntyre66] R.J. McIntyre. *Multiplication noise in uniform avalanche diodes*. IEEE Trans. Electron Devices, vol. ED-13, pages 164–168, 1966.
- [Miller60] A. Miller, and E. Abrahams. *Impurity Conduction at Low Concentrations*. Phys. Rev., vol. 120, pages 745–755, 1960.
- [Nishimura65] H. Nishimura. *Impurity Conduction in the Intermediate Concentration Region*. Phys. Rev., vol. 138, no. 3A, pages A815–A821, 1965.
- [Overstraeten70] R. van Overstraeten, and H. de Man. *Temperature Dependence on the Electron Impact Ionization Coefficient in Silicon*. Solid State Electron., vol. 13, pages 583–608, 1970.
- [Papoulis84] A. Papoulis. “Probability, random variables, and stochastic processes”. Mc-Graw Hill, 1984.
- [Petroff86] M.D. Petroff, and M. G. Stapelbroek. *Blocked impurity band detectors*. U.S. Patent No. 4568960, 1986.
- [Petroff87] M. D. Petroff, M. G. Stapelbroek, and W. A. Kleinmans. *Detection of individual 0.4-28 micron wavelength photons via impurity-impact ionization in a solid-state photomultiplier*. Appl. Phys. Lett., vol. 51, pages 406–408, 1987.
- [R.-Bolívar05] S. R.-Bolívar, F. M. Gómez-Campos, and J. E. Carceller. *Simple analytical valence band structure including warping and non-parabolicity to investigate hole transport in Si and Ge*. Semicond. Sci. Technol., vol. 20, no. 1, pages 16–22, 2005.
- [Reggiani73] L. Reggiani, and C. Calandra. *Bloch states mixing in Si conduction band*. Physics Letters A, vol. 43, pages 339–340, 1973.
- [Rieger93] M.M. Rieger, and P. Vogl. *Electronic-Band Parameters in Strained $Si_{1-x}Ge_x$ Alloys on $Si_{1-y}Ge_y$ Substrates*. Phys. Rev. B, vol. 48, pages 14276–14287, 1993.
- [Ritenour03] A. Ritenour, S. Yu, M. L. Lee, N. Lu, W. Bai, A. Pitera, E. A. Fitzgerald, D. L. Kwong, and D. A. Antoniadis. *Epitaxial Strained Germanium P-MOSFETs with HfO_2 Gate Dielectric and TaN Gate Electrode*. Proc. Intl. Electron Devices Meeting, pages 433–436, 2003.

BIBLIOGRAPHY

- [Sclar56] N. Sclar. *Neutral Impurity Scattering in Semiconductors*. Phys.Rev., vol. 104, no. 6, pages 1559–1561, 1956.
- [Shklovskii84] B. I. Shklovskii, and A. L. Efros. “Electronic properties of doped semiconductors”. Springer, Berlin, 1984.
- [SIA06] Semiconductor Industry Association SIA. *International Technology Roadmap for Semiconductors - 2006 Update*, 2006. <http://www.itrs.net>.
- [Sinitisa02] S. P. Sinitisa. *Simulation of avalanche multiplication of electrons in photodetectors with blocked hopping conduction*. Semiconductors, vol. 36, no. 5, pages 588–591, 2002.
- [Skotnicki05] T. Skotnicki, J. A. Hutchby, Tsu-Jae King, H. S. P. Wong, and F. Boeuf. *The end of CMOS scaling: toward the introduction of new materials and structural changes to improve MOSFET performance*. IEEE Circuits & Devices, vol. 21, pages 16–26, 2005.
- [Slotboom87] J. W. Slotboom, G. Streutker, G. J. T. Davids, and P. B. Hartog. *Surface Impact Ionization in Silicon Devices*. Proc.Intl.Electron Devices Meeting, pages 494–497, 1987.
- [Stanley98] J. Stanley, and N. Goldsman. *New irreducible wedge for scattering rate calculations in full-zone Monte Carlo simulations*. VLSI Design, vol. 8, no. 1–4, pages 413–417, 1998.
- [Stetson86] S. B. Stetson, D. B. Reynolds, M. G. Stapelbroek, and R. L. Stermer. *Design and performance of blocked-impurity-band detector focal plane arrays*. In H. Nakamura, editor, Infrared detectors, sensors, and focal plane arrays; Proceedings of the Meeting, San Diego, CA, Aug. 21, 22, 1986 (A88-12689 02-35). Bellingham, WA, Society of Photo-Optical Instrumentation Engineers, volume 686 of *Presented at the Society of Photo-Optical Instrumentation Engineers (SPIE) Conference*, pages 48–65, 1986.
- [Stillman77] G. E. Stillman, and C. M. Wolfe. *Avalanche Photodiodes*. In R.K. Willardson, and A.C. Beer, editors, Semiconductors and Semimetals, volume 12, New York, 1977. Academic Press.
- [Sze81] S. M. Sze. “Physics of semiconductor devices”. Wiley, New York, second edition, 1981.
- [Szmulowicz80] F. Szmulowicz, and R. Baron. *The effect of light attenuation on quantum efficiency for transverse and longitudinal responsivity and detectivity*. Infrared Physics, vol. 20, pages 385–391, 1980.

BIBLIOGRAPHY

- [Szmulowicz86] F. Szmulowicz, K. T. Bloch, and F. L. Madarasz. *Effect of light attenuation on the responsivity and detectivity of transverse and longitudinal detectors*. J.Appl.Phys., vol. 60, pages 4300–4307, 1986.
- [Szmulowicz87] F. Szmulowicz, and F. L. Madarasz. *Blocked impurity band detectors: An analytical model - Figures of merit*. J.Appl.Phys., vol. 62, pages 2533–2540, 1987.
- [Uchida04] K. Uchida, R. Zednik, C.-H. Lu, H. Jagannathan, J. McVittie, P. C. McIntyre, and Y. Nishi. *Experimental study of biaxial and uniaxial strain effects on carrier mobility in bulk and ultrathin-body SOI MOSFETs*. In Proc.Intl.Electron Devices Meeting, pages 229–232, 2004.
- [Uchida05] K. Uchida, T. Krishnamohan, K.C. Saraswat, and Y.Nishi. *Physical mechanisms of electron mobility enhancement in uniaxial stressed MOSFETs and impact of uniaxial stress engineering in ballistic regime*. In Proc.Intl.Electron Devices Meeting, pages 135–138, 2005.
- [Ungersboeck07a] E. Ungersboeck. *Advanced Modeling of Strained CMOS Technology*. PhD thesis, Vienna Technical University, 2007. <http://www.iue.tuwien.ac.at/phd/ungersboeck/>.
- [Ungersboeck07b] E. Ungersboeck, S. Dhar, G. Karlowatz, H. Kosina, and S. Selberherr. *Physical Modeling of Electron Mobility Enhancement for Arbitrarily Strained Silicon*. Journal of Computational Electronics, vol. 6, no. 1-3, pages 55–58, 2007.
- [Ungersboeck07c] E. Ungersboeck, S. Dhar, G. Karlowatz, V. Sverdlov, H. Kosina, and S. Selberherr. *The Effect of General Strain on the Band Structure and Electron Mobility of Silicon*. IEEE Trans.Electron Devices, vol. 54, no. 9, pages 2183–2190, 2007.
- [Wagner04] Martin Wagner. *A base Library for Full Band Monte Carlo Simulations*. Diplomarbeit, Institut für Mikroelektronik, Technische Universität Wien, März 2004.
- [Wang06] E. X. Wang, L. Shifren, B. Obradovic, R. Kotlyar, S. Cea, M. Stettler, and M. D. Giles. *Physics of Hole Transport in Strained Silicon MOSFET Inversion Layers*. IEEE Trans.Electron Devices, vol. 53, no. 8, pages 1840–1851, 2006.
- [Welser92] J. Welser, J. L. Hoyt, and J. F. Gibbons. *NMOS and PMOS transistors fabricated in strained silicon/relaxed silicon-germanium*

BIBLIOGRAPHY

- structures*. In Proc.Intl.Electron Devices Meeting, pages 1000–1002, 1992.
- [Welser94] J. Welser, J. L. Hoyt, and J. F. Gibbons. *Electron Mobility Enhancement in Strained-Si N-Type Metal-Oxide-Semiconductor Field-Effect Transistors*. IEEE Electron Device Lett., vol. 15, no. 3, pages 100–102, 1994.
- [Yamada95] T. Yamada, and D. K. Ferry. *Monte Carlo Simulation of Hole Transport in Strained $Si_{1-x}Ge_x$* . Solid State Electronics, vol. 38, no. 4, pages 881–890, 1995.
- [Yu03] P. Yu, and M. Cardona. “Fundamentals of Semiconductors”. Springer, 2003.

Own Publications

- [Dhar05a] S. Dhar, G. Karlowatz, E. Ungersboeck, and H. Kosina. *Numerical and Analytical Modeling of the High-Field Electron Mobility in Strained Silicon*. In Proc. Simulation of Semiconductor Processes and Devices, pages 223–226, 2005.
- [Dhar05b] S. Dhar, G. Karlowatz, E. Ungersboeck, H. Kosina, and S. Selberherr. *Modeling of Velocity Field Characteristics in Strained Si*. In Proceedings of the Fourteenth International Workshop on the Physics of Semiconductor Devices, pages 1060–1063, 2005.
- [Dhar06a] S. Dhar, H. Kosina, G. Karlowatz, E. Ungersboeck, T. Grasser, and S. Selberherr. *A tensorial high-field electron mobility model for strained silicon*. SiGe Technology and Device Meeting, ISTDM 2006, pages 72–73, 2006.
- [Dhar06b] S. Dhar, H. Kosina, G. Karlowatz, S. E. Ungersboeck, T. Grasser, and S. Selberherr. *High-Field Electron Mobility Model for Strained-Silicon Devices*. IEEE Trans. Electron Devices, vol. 53, no. 12, pages 3054–3062, 2006.
- [Gröschl03] M. Gröschl, R. Thalhammer, G. Karlowatz, E. Benes, and H. Nowotny. *Viscosity Monitoring with a quartz crystal thickness shear resonator*. Proc. of the 1st Congress of the Alps Adria Acoustics Association, pages 663–672, 2003.
- [Karlowatz06a] G. Karlowatz, E. Ungersboeck, W. Wessner, and H. Kosina. *Full-Band Monte Carlo Analysis of Electron Transport in Arbitrarily Strained Silicon*. In Proc. Simulation of Semiconductor Processes and Devices, pages 63–66, Monterey, USA, 2006.

OWN PUBLICATIONS

- [Karlowatz06b] G. Karlowatz, E. Ungersboeck, W. Wessner, H. Kosina, and S. Selberherr. “Analysis of hole transport in arbitrarily strained germanium”, volume 3 of *ECS Transactions*. The Electrochemical Society, 2006.
- [Karlowatz06c] G. Karlowatz, E. Ungersboeck, W. Wessner, H. Kosina, and S. Selberherr. *Analysis of Hole Transport in Arbitrarily Strained Germanium*. In Meeting Abstracts: 210th Meeting of The Electrochemical Society, page 1449, 2006.
- [Karlowatz06d] G. Karlowatz, W. Wessner, and H. Kosina. *Effect of Band Structure Discretization on the Performance of Full-Band Monte Carlo Simulation*. Mathmod Vienna Proceedings, vol. 5, no. 1, pages 4.1–4.6, 2006.
- [Karlowatz08] G. Karlowatz, W. Wessner, and H. Kosina. *Effect of Band Structure Discretization on the Performance of Full-Band Monte Carlo Simulation*. MATHCOM, vol. 79, no. 4, pages 972–979, 2008.
- [Sverdlov07a] V. Sverdlov, G. Karlowatz, S. Dhar, H. Kosina, and S. Selberherr. *Two-band k - p model for the conduction band in silicon: Impact of strain and confinement on band structure and mobility*. International Semiconductor Device Research Symposium, 2007. ISBN: 978-1-4244-1892-3.
- [Sverdlov07b] V. Sverdlov, G. Karlowatz, H. Kosina, and S. Selberherr. *Two-band k - p model for the conduction band in silicon*. Proceedings European Simulation and Modeling Conference, pages 220 – 224, 2007. ISBN: 978-90-77381-36-6.
- [Sverdlov07c] V. Sverdlov, G. Karlowatz, E. Ungersboeck, and H. Kosina. *Influence of Uniaxial [110] Stress on the Silicon Conduction Band Structure: Stress Dependence of the Nonparabolicity Parameter*. In Simulation of Semiconductor Processes and Devices, volume 12, pages 329–332, Vienna, 2007.
- [Sverdlov08] V. Sverdlov, G. Karlowatz, S. Dhar, H. Kosina, and S. Selberherr. *Two-band k - p model for the conduction band in silicon: Impact of strain and confinement on band structure and mobility*. Solid-State Electron., vol. 52, pages 1563–1568, 2008.
- [Thalhammer03] R. Thalhammer, S. Braun, B. Devcic-Kuhar, G. Karlowatz, M. Gröschl, F. Trampler, E. Benes, H. Nowotny, and M. Košťál. *Viscosity Monitoring with a Quartz Crystal Resonator*. Journal of Electrical Engineering, vol. 54, no. 5-6, pages 140–143, 2003.

OWN PUBLICATIONS

- [Ungersboeck06] E. Ungersboeck, S. Dhar, G. Karlowatz, H. Kosina, and S. Selberherr. *Physical Modeling of Electron Mobility Enhancement for Arbitrarily Strained Silicon*. In 11th International Workshop on Computational Electronics Book of Abstracts, pages 141–142, 2006.
- [Ungersboeck07a] E. Ungersboeck, S. Dhar, G. Karlowatz, H. Kosina, and S. Selberherr. *Physical Modeling of Electron Mobility Enhancement for Arbitrarily Strained Silicon*. *Journal of Computational Electronics*, vol. 6, no. 1-3, pages 55–58, 2007.
- [Ungersboeck07b] E. Ungersboeck, S. Dhar, G. Karlowatz, V. Sverdlov, H. Kosina, and S. Selberherr. *The Effect of General Strain on the Band Structure and Electron Mobility of Silicon*. *IEEE Trans. Electron Devices*, vol. 54, no. 9, pages 2183–2190, 2007.

	Author	Co-Author	Total
Journals & Contributions to books	2	3	5
Conferences	3	10	13
Total	5	13	18

Table 1: Publication statistics.



Curriculum Vitae

October 25th, 1972

Born in Mödling, Austria.

1992

High school graduation (*Matura*)
at the Höhere Technische Bundeslehranstalt und Versuchsanstalt Mödling.

1992

Enrolled in Technical Physics at the Vienna University of Technology, Austria.

2002

Working with refugees within the compulsory civilian service.

2003

Received degree of *Diplom-Ingenieur* in Technical Physics from the Vienna University of Technology.

2003 – 2007

Entered the position of project assistant and doctoral program at the Institute for Microelectronics, Vienna University of Technology, under the supervision of Prof. Hans Kosina.